Development of a Three-Dimensional Anthropometric Model for Simulating Hand Work

by

Rosemarie Figueroa-Jacinto

A dissertation submitted in partial fulfillment
of the requirements for the degree of
Doctor of Philosophy
(Industrial and Operations Engineering)
in The University of Michigan
2017

Doctoral Committee:

Professor Thomas J. Armstrong, Chair
Assistant Professor Clive D'Souza
Associate Professor Melissa Gross
Professor Albert J. Shih

Rosemarie Figueroa

rosemfig@umich.edu

ORCID iD: 0000-0002-3843-1258

DEDICATION

To my father, mother, and grandmother Julia M. Diaz

ACKNOWLEDGMENTS

iii

To Mike Nazareth, Andria Rose and Shira Washington- thank you for giving me the tools needed so that I could always give back to others and for standing by me since before I started applying to graduate schools. Also, thanks to my Latin community and Capoeira family for all the good memories and for helping me build and sustain an appropriate work/life balance throughout my graduate program. To my friends - Brandon, Vernnaliz, Lianette, Christie, Deema, Matt, Alex, Gerardo, Esteban, Ona, Francisco, Alejandro, and Lena- thank you for making this ride a fun one and for cherish great moments with me. Ben, thank you for your endless support and help during these years. I am also grateful of Chavo, who kept me company during my college and grad school years - much love to you. I am grateful of my best friend Mayté for her long-distance support, care packages and continuous encouragement. Cheers to many more years of friendship and travel!

Last but not least, many thanks to all my family, especially to my parents Ivan and Rosa, and abuela Mary for their endless love and encouragement. ¡Si se pudo!

TABLE OF CONTENT

LIST OF TABLES

LIST OF FIGURES

LIST OF APPENDICES

ABSTRACT

This dissertation provides new data for 1) predicting hand strength capabilities under different conditions, as well as 2) developing a skeleton-driven 3-D anthropometric model of the hand. This model can be used to understand the effect of hand posture and shape to force exertions while grasping objects, interacting with surfaces and/or supporting the person's body.

To complement existing hand exertions data in literature, a study of 12 participants was performed to investigate the effect of hand posture and surface orientation on hand force while pressing a flat surface. This study showed that participants were able to exert more force in a direction away from the body at elbow height than at shoulder height. Overall, the greatest proportion of the force, 72-75% of total force, was exerted over the base of the palm followed by 11-13% with the thumb when participants pushed the plate forward (45° and 90°) and downward (0°). Joint moment and finger force distribution data from this study can be incorporated in computerized 3D-models of the hand to compare strength capabilities between postures.

A skeleton-driven hand model was developed leveraging existing source data and technologies, including available medical images of the hand, current hand models, and

statistical bone shape models developed for other parts of the body. This was achieved in three steps. First, 3D meshes were developed for skin surface and bone segments based on CT scans of a single hand in five different postures. This hand was used to develop a quantitative method to establish coordinate systems for the 3D surface geometries, which are applicable to any hand after segmentation. The flat hand posture from this study was selected as the template hand and used in the following studies. Second, the 3D bone geometries and their respective coordinate systems were used to adapt four methods for determining phalange Centers of Rotation (CoR). These four methods were 1) Sphere Fitting, 2) Ellipsoid Fitting, 3) 3D-Reuleaux, and 4) Iterative Closest Point Algorithm (ICP). Sphere- and Ellipsoid-fitted CoRs were considered fixed, with fixed rotational axes based on simple links representing each segment. Reuleaux- and ICP-based CoRs were considered instantaneous, with variable link lengths identified by the rotation and the gliding action (translation) at the joints. The latter considers the anatomical structure of the bones when determining the location of the instant centers. Results from this study show that there is a significant difference between fixed and instantaneous CoRs, and that instantaneous CoRs provide a more accurate and robust kinematic model, particularly at high joint angles. Third, these CoR calculation methods were leveraged to develop landmark-free statistical models from clinical CT scans of 43 hands. The 3D-bone surface geometries of the template hand from the prior study were used to create homologous surfaces to represent (fit) each hand and to rotate each hand to that common posture. Kinematics developed from the ICP method were used to rotate finger segments

of fitted hands to 1) obtain hand skin measurements in a common posture, 2) predict whole hand skeleton shape/size, and 3) evaluate final shape predictions in the original postures. Principal component analysis and regression (PCAR) were then used to 1) describe variations in hand bone geometries with respect to hand length, hand breadth, hand thickness and sex, and 2) develop statistical models for shape/size prediction of individual finger bone geometries, as well as a whole hand skeleton model with hand skin surface reference points for scaling. The shape predictions of the hand bones, with reference points located around the skin surface, can be used as a baseline for any hand surface model to establish kinematics based on internal bone segments.

This dissertation aims to push forward the state of the art by increasing the understanding on the variables needed to realistically model a hand by 1) by providing new data for predicting hand strength capabilities and 2) developing a skeleton-driven 3-D model of the hand.

CHAPTER 1 Introduction

1.1 Overview

Models of the human hand can be used to predict postures and forces required to grasp, hold, and use objects. These models are needed for ergonomic and biomechanical analyses so that requirements for manual tasks are safely within worker capabilities. This dissertation provides new data for predicting hand strength capabilities when pressing a flat surface and develops a skeleton-driven 3-D anthropometric model of the hand that can be used to enhance current ergonomic analyses by predicting hand posture and estimating hand shape.

1.2 Aims

The general aim of this work is to develop a 3-D model that can be used to predict hand postures and movements, as well as bone shapes and sizes. To achieve this aim, the following objectives were established:

1. Determine the relationship between surface orientation, posture, and force when pressing a flat surface with the hand.

2. Developed models that describe bone surfaces and their axes based on medical images for use in simulation models.

3. Develop procedures to adapt methods to determine centers of rotation to finger joints using internal measurements obtained through CT-Scans.

4. Develop a 3-D statistical model of the hand by predicting bones shape/size and scaling the skin surface based on reference points to represent any population.

1.3 Background and Significance

We use our hands to gather information in our environment as tactile feedback, to support our body, and to apply controlled forces to grasp, hold, and manipulate objects (MacKenzie & Iberall 1994; Napier, 1993). With our hands, we perform tasks ranging from gentle and precise manipulations (e.g. using surgical tool or writing) to forceful exertions (e.g. lifting, using tools or playing sports). Thus, chronic and acute hand injuries often impair human performance during work and daily routine, and are a common cause of disability.

Injuries of the hand, fingers, and wrist are a frequent cause of Emergency Room visits (Ootes et al., 2012; Feehan et al., 2006; Larsen et al., 2004). In the US, they accounted for 10% of all visits in 2013, according to Centers for Disease Control and Prevention (CDC, 2008). Households are cited as the most common setting for an upper extremity injury (Ootes et al., 2012). In the workplace, hand injuries remain the second most common type (with back injuries as most common) and one sixth of all disabling work injuries involve the fingers (Eaton, 2007). According to the U.S. Bureau of Labor Statistics, in 2015 employers reported 268,440 hand injuries that led to lost-workdays with an incidence rate of 13%. An average direct cost per compensation claim for upper extremity disorders is around $11,411 (Silverstein et al., 2006). Moreover, there are

numerous examples, aside from direct hand injuries, where loss of grip caused property damage, injuries in other parts of the body, and/or fatalities (Hamelund, 2012; Young et al., 2010; Hass and Meyers, 1995).

Human modeling has been of great value in the medical field for performing anatomical studies, diagnosis, and surgical planning, training and navigation (Figueroa et al., 2014; Jan et al., 1997). Hand modeling has been widely used for characterizing hand shape, posture and movements through biomechanical (Marras & Radwin, 2005) and ergonomic assessments (Seo et al., 2007; Miyata et al., 2007; Frederick and Armstrong 1995; Buchholz & Armstrong, 1992). However, hand models (Armstrong, Choi et al, 2008; Sancho-bru, 2000) have not yet reached the level of accuracy of whole body models, due to the immense complexity of the hand's shape and structure (Bullock, Borras & Dollar, 2012). Hand models that predict force, posture, and shape data are needed to ensure that tools, garments, products, and work-tasks are designed properly for the intended users (Armstrong et al., 2009; Armstrong, Choi and Ahuja, 2008; Grieshaber, 2007; Sorock et al., 2002; Nag, 1998).

Without any assumptions, there is an infinite number of possible configurations for fingers, wrist and arm segments. However, biomechanical analyses help reduce the number of potential posture predictions by orders of magnitude through imposing anatomical constraints (Marras & Radwin, 2005) and minimizing interference from obstructions (Armstrong et al., 2009). Also, by characterizing population preferences based on their biomechanical behavior the number of possible posture predictions can be further reduced (Figure 1.1).
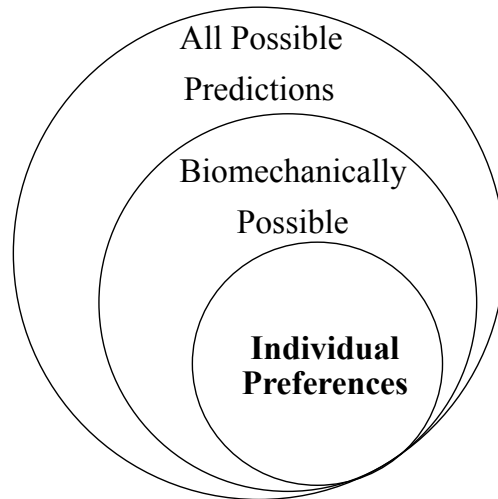
Figure 1.1 Biomechanical analyses help reduce the number of solutions based on population/individual preferences.

Thus, hand posture can be predicted based on characterizing behaviors per population based on force exertions produced by the hand, and by understanding the internal structure of the hand (Figure 1.2). The force (F_R) exerted against a surface or object is related to the joint loads specific to a certain posture. These joint loads (M) are relative to their location based on the link lengths (l) and the angles between the segments (θ), and can be deconstructed based on the tendon excursions (F_{ex} and F_{flex}) and their relative distance to the center of each joint. Studying these internal forces allows us to describe the motions of individual body parts, as well as the nature and the causes of injuries. Additionally, the external environment (e.g. obstruction, object properties, task requirements) plays a major role when determining potential hand placements and angles between the segments (θ).

$$\vec{F}_R = f(\begin{bmatrix} \theta_1 \\ \theta_2 \\ \theta_n \end{bmatrix} \begin{bmatrix} \vec{l_1} \\ \vec{l_2} \\ \vec{l_n} \end{bmatrix} \begin{bmatrix} \vec{M_1} \\ \vec{M_2} \\ \vec{M_n} \end{bmatrix})$$

$$\begin{bmatrix} \theta_1 \\ \theta_2 \\ \theta_n \end{bmatrix} = f(\begin{bmatrix} \vec{l_1} \\ \vec{l_2} \\ \vec{l_n} \end{bmatrix} \begin{bmatrix} object/surface \\ orientation, \\ shape, size, etc. \end{bmatrix})$$
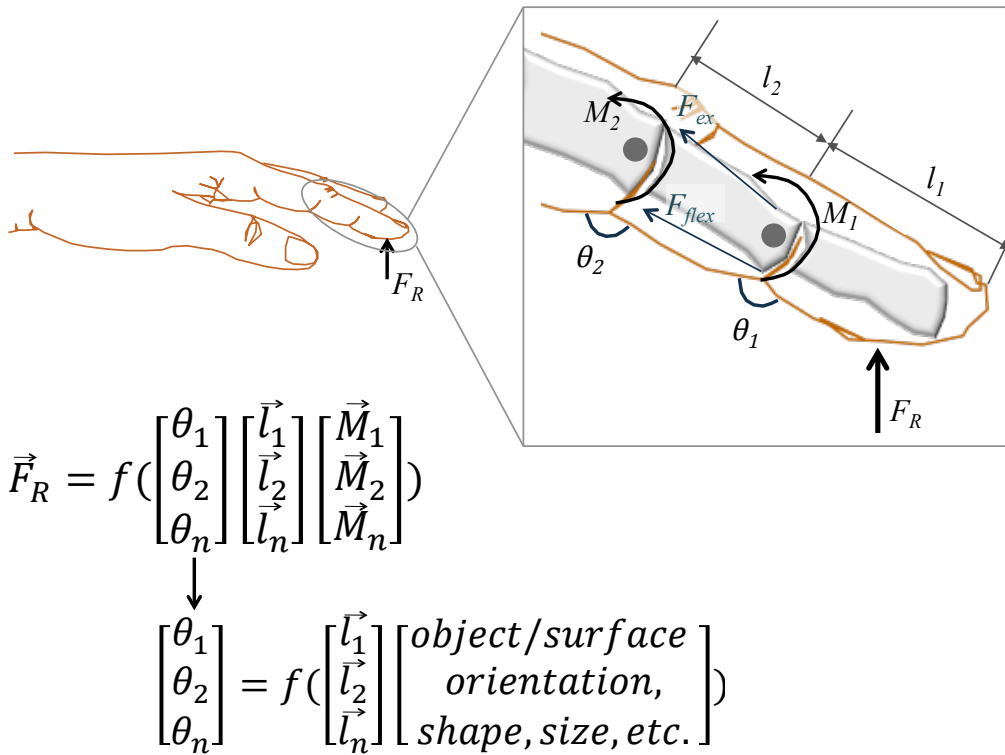
Figure 1.2 Hand force exertions and placement can be modeled by understanding the internal structure and the relationship between the internal and external surfaces

This builds into the broader set of research related to hand placement, which aims to understand and model hand force, posture, and shape based on different types of external forces, internal factors, object and task requirements, and subject anthropometrics (Figure 1.3).
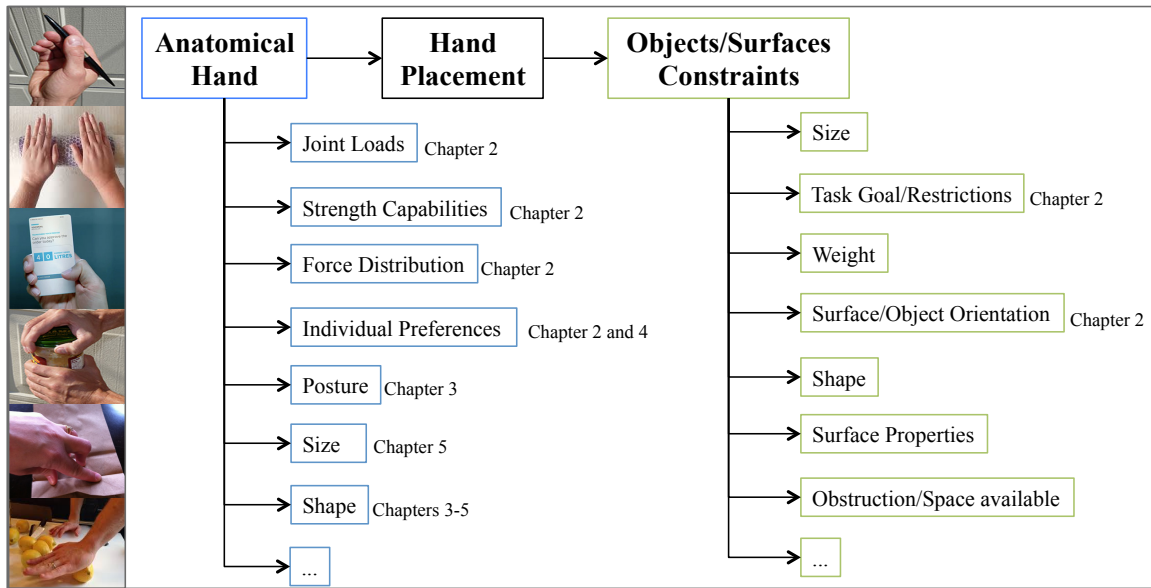
Figure 1.3 Information needed to accurately depict hand placement on an object or surface.

Over the years, several studies have evaluated hand strength based on forces exerted between the fingers and thumb or palm while holding an object (Szychlinska et al., 2017; Zhou et al., 2011; Kargov et al., 2009; Rosenbaum et al., 2009, Seo et al., 2007; Salimi et al. 2003; Blackwell et al., 1999; Fransson and Winkel, 1991; Mathiowetz et al., 1985; Chaffin et al., 1983). However, in many cases, the finger forces are exerted in the same direction against an external surface, not against another part of the hand. Studies need to be developed to analyze strength capacities when finger forces are oriented in the same direction and in other conditions.

To evaluate hand prehensile capabilities, Buchholz and Armstrong (1992) proposed a kinematic model based on collision detection between ellipsoids, assuming simplified motions between hand segments. Other studies (Vignais & Marin, 2010; Rogers et al., 2008; Miyata et al., 2006; Rehg, 1994; Lee, 1995; Kuch, 1995; Sturman, 1994) have used motion capture methods for collecting hand posture data to derive the link structure and surface deformation. However, hand self-occlusion, large skin

6

deformation, complex calibration/setup, and lack of hand breadth/thickness information are limitations in using motion-capture for reconstructing hand motion. Rogers, et al. collected hands from different subjects in several postures (Rogers, et al. 2008) to reconstruct a scalable 3D-hand model. However, marker positions were limited to the palmar surface of the hand, resulting in rough 3D shapes without hand thickness information.

Endo, et al. proposed a method for deforming a skin template and fit landmarks to marker positions from motion capture (Endo et al., 2014). Miyata, et al. reproduced a hand surface shape by statistically adjusting the shape using plaster molds of the hand in various postures (Miyata et al., 2013). CT Scans were used to fabricate these molds and their 3D shapes. Albrecht, et al. developed a computer based model animated using muscle contraction values (Albrecht et al., 2003). Yet, these three methods still relied on motion capture to develop the link structure and kinematics, simplifying the joints as an intersection of the links rather than anatomical joints formed by the movement of one bone relative to another. This difference in the geometry leads to different reaction forces. Therefore, an anatomically based segment coordinate system should be created to better model the movement of one bone with respect to another. Underlying skeleton-critical dimensions can be used to estimate anatomical joint centers of rotation to predict hand postures. Detailed skeleton geometry, as well as good estimates of the joint structures and surface deformation, can be obtained using 3D measurements from medical images (McInerney & Terzopoulos, 1996).

Other investigators have used medical scans to create skeleton-based biomechanical models (Figueroa, et al., 2016; Shimizu, et al., 2010; Miyata, et al., 2012, 2007, 2006; Lien, 2005; Kurihara & Miyata, 2004). However, they were either not scalable, partially scalable, and/or were based on Magnetic Resonance Imaging (MRI). CT provides better bone shape detail and is less sensitive to patient movement than MRI (McKinnis, 2010). CT imaging allows the user to obtain joint data in a relatively short period of time (McKinnis, 2010) such that several positions can be acquired with minimal discomfort. Jan, et al. proposed a skeleton-driven method by manually identifying landmarks and manually placing surface markers on bones to determine the joint rotation (Jan et al., 1997).

Prediction models for geometric shape and size parameters with subject characteristics have been developed for different parts of the body, such as the femur (Klein, et al., 2015), rib cage (Shi, et al., 2014; Reed, et al., 2009), knee joint (Chalovich & Eisenberg, 2005), and whole body (Park et al., 2015). All these methods were based on manual landmarking. In practice, manual landmarking becomes difficult and error prone (Mutsvangwa, 2015). There has been considerable progress on general landmark-free approaches by defining correspondences automatically and using statistical shape modeling analyses (Mutsvangwa, 2015; Brett & Taylor, 2000). Miyata, et al. developed a statistical shape model for predicting hand surface based on skin landmarks identified from motion-capture data (Miyata, et al., 2012). However, currently there are no statistical models for hand bone shapes and sizes. Statistical shape modeling for predicting hand bone shapes and sizes can be useful to generalize skeleton-driven joint structures for any population.

This work contributes by investigating the mechanical relationship between hand and work objects and developing a 3D-hand model that accurately depicts bone shapes and sizes with parameters based on hand length and breadth for female and male measurements. The proposed skeleton-driven model could be used to:

- Evaluate the spatial relationship between the hand and external objects
- Determine feasible hand postures and forces
- Prevent and assess hand injuries through better design of products, workplaces, and tasks

1.4 Dissertation Outline

This dissertation starts with an introduction (Chapter 1) followed by four main chapters for each research objective (Chapters 2-5) and finishes with a concluding chapter (Chapter 6).

Chapter 2 presents a laboratory study that examines the effect of surface orientation and posture on hand force while pressing a flat surface. Joint moments and force distributions from this study can be used to compare strength capabilities and can be incorporated into computer models of the hand.

Chapter 3 describes a method for generating and evaluating three-dimensional hand anatomical representations extracted from CT-Scans of one hand positioned in five different configurations.

Chapter 4 describes the development of procedures to adapt four methods to estimate centers of rotation – Sphere fitting, Ellipsoid fitting, 3-D Reuleaux and Iterative Closest Point– to finger joints using the 3D bone surfaces developed in Chapter 3.

Chapter 5 describes the development of a statistical shape model to properly estimate hand bone shapes and sizes for any given population. This model uses internal and external anthropometric dimensions based on medical images to develop and evaluate empirical factors for estimating shape and size.

Finally, Chapter 6 presents a summary of major findings and suggestions for future studies.

CHAPTER 2 An Investigation on Normal Force Distribution and Posture of a Hand Pressing on a Flat Surface

Abstract

Hand strength data are needed to understand and predict hand postures and finger loads while placing the hand on an object or surface. This study aims to analyze the effect of hand posture and surface orientation on hand force while pressing a flat surface. Twelve participants, 6 females and 6 males ages 19-25, performed three exertions (100%, 30% and 10% MVC- Maximum Voluntary Contraction) perpendicular to a plate in 4 angles (-45˚, 0˚, 45˚ and 90˚ with respect to horizontal plane) at elbow height. Exertions involved pushing in two postures: 1) whole hand and 2) constrained to only using the fingertips. Inter-digit joint angles were recorded to map hand and finger motions and estimate joint moments for each condition. Participants exerted twice the force when pushing with whole hand vs. fingertips. 72-75% of the total force was exerted over the base of the palm, while only 11-13% with the thumb for exertions at 90°, 45° or 0° plate angles. Males maximum force for pushing at 0˚, 45˚ and 90˚ plates averaged 49% higher than females for the whole hand and 62% for the fingertips (p<0.01). There was no significant sex difference (p>0.05) for the -45˚ plate. Thumb joint loads were generally higher than the other individual fingers (p<0.05) in all %MVC, and accounted for 12% of total force during whole hand exertions. On average, joint moments were 30% higher

11

during fingertip conditions vs. whole hand. Thumb and finger joint moment magnitudes when pushing the plate at 100%MVC indicated that Metacarpophalangeal (MCP) joint moments were higher ($p<0.05$) than Distal Interphalangeal joints (DIP) and Proximal Interphalangeal joints (PIP) under whole hand and fingertips conditions.

2.1. Introduction

Hand strength data are needed to understand and predict hand postures and finger loads while placing the hand on an object or surface. Most available strength data are based on forces exerted between the fingers and the thumb or palm while gripping an object (Kargov et al., 2009; Zhou et al., 2011; Rosenbaum et al., 2009, Mathiowetz et al., 1985). However, in several cases the fingers' force is exerted against an external surface instead of another part of the hand. These exertions could include only the fingertips or the whole hand. These exertions are common in everyday activities, including when a person supports their body on a table, plays sports (e.g. basketball, football, sprinting and gymnastics), and many work activities (e.g. installing interior panels in automobiles; laying hardwood floors) (Figure 2.1).

Figure 2.1 Examples of hands pressing a flat surface with the whole hand vs. just the fingertips.

12

However, prior studies have focused on pushing while grabbing a handle or while grasping objects. Force exertion during pushing tasks had been evaluated while grabbing handles in different sizes (Seo et al., 2007), on fixed or variable heights (Chaffin et al. 1983; Hoffman et al., 2007) and different angles (Das & Wang, 2004). Additionally, previous studies have shown that hand placement is related to object and task factors. For instance, Rosenbaum et al. (1990) and Zhou et al. (2011) demonstrated that grip selection depends on prior specifications of object orientation. These studies suggest that relative joint loads and force distribution are related to hand placement when grasping objects. In this study, during exertions using either just fingertips or whole hand, the forces involve muscles that produce moments and loads about inter phalangeal joints making the hand and fingers flex against the surface. Those joint positions and loads determine hand strength capabilities and hand posture (Chaffin, 2008; Hara et al., 1992; Daams, 1993; Rancourt & Hogan, 2001; Di Dominizio & Keir, 2010).

Prior studies also show that higher grip force occurs when there is a larger amount of area to distribute the force around the object, where finger and thumb forces work together against the palm region while grasping an object (Seo et al., 2007; Szychlinska et al. 2017). Seo et al. (2007) showed this by analyzing hand force distributions and resultant forces on different diameter cylinders. However, force distribution has not being analyzed while pushing a flat surface. It is hypothesized that similarly to the results from Seo et al. (2007) where grip forces are related to the amount of area to distribute the force, higher push forces occur where there is a larger amount of force is distributed during whole hand exertions.

This study aims to examine how hand force exerted against a flat surface is affected by hand posture and surface orientation. Towards this end, this study investigates 1) the effect of orientation of a flat surface on finger force distribution and upper extremity posture, 2) force distribution between the fingers, and 3) hand-joint moment while pressing the flat surface. Such hand strength data is necessary for hand posture and force predictions, which are used in several fields ranging from computer graphics to biomechanical and ergonomic assessments.

2.2. Methods

To achieve the stated aim, a laboratory study was conducted on contact force distribution while pressing a flat surface using a whole hand vs. fingertips under -45˚, 0˚, 45˚ and 90˚ orientations and at 100%, 30% and 10% Maximum Voluntary Contraction (MVC).

2.2.1. *Apparatus*

Grip strength was measured with a Jamar® grip dynamometer at 49mm span, and thumb-index finger pinch strength was measured with a B&L® pinch gauge (Mathiowetz et al., 1984; Mathiowetz et al., 1985; Hamilton et al., 1992). Hand length was measured according to Gordon et al. (1989) with a caliper over their hand on a table with the fingers together.

An aluminum plate of 230 by 230 mm was attached to a force transducer (Figure 2.2).
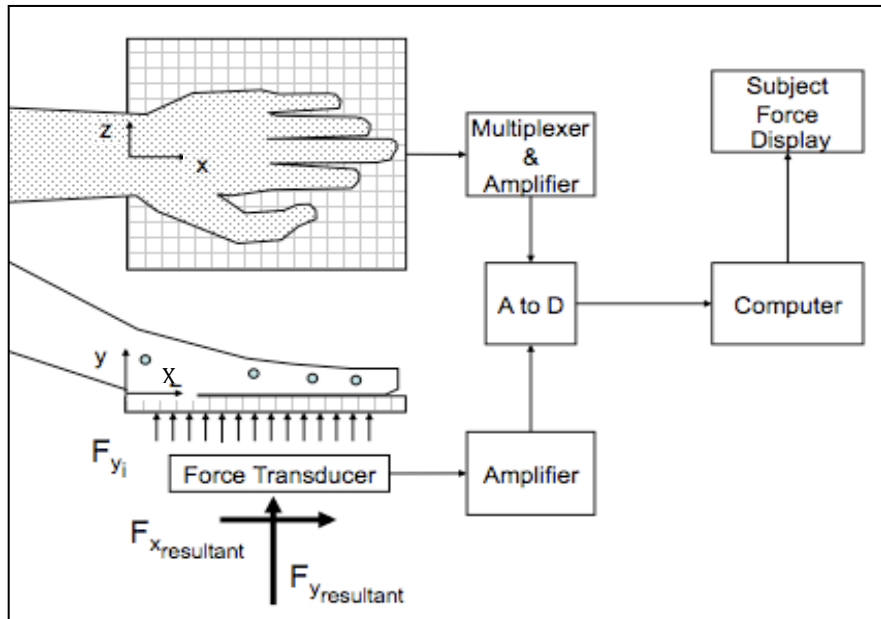
Figure 2.2 Force transducer setup when pressing with WH posture at 0˚ angle.

This force transducer was attached to a gimbal, enabling rotation about a single axis (Figure 2.3). LabVIEW (National Instruments, Inc., Austin TX) at 60Hz was used to determine total force (F) and to ensure participants exert normal forces, discarding any friction forces. Data were averaged over 3s during maximum force exertions. A video display was placed in front of the participants, to provide feedback by showing their normal force at 200ms intervals. Floor surface and soft-sole shoes had enough traction to assume leaning postures without slipping risk (Chaffin et al., 1983).
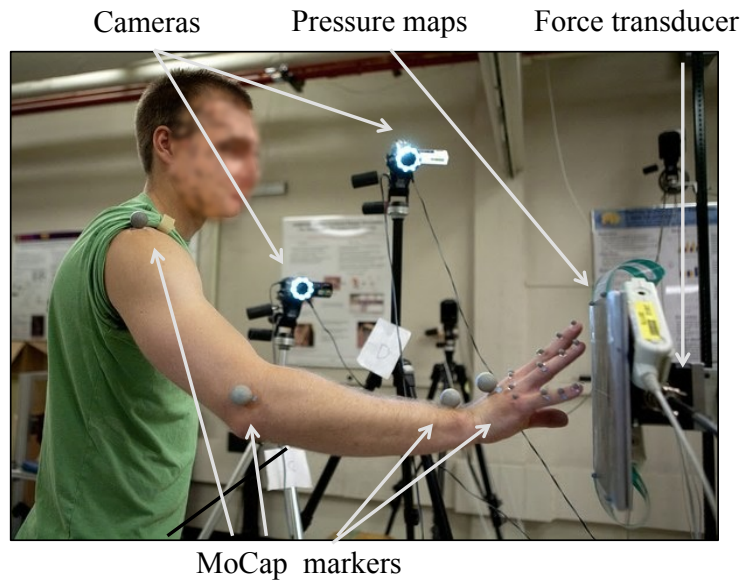
Figure 2.3 Side view of setup of markers, cameras, pressure maps and plate when pressing with FT posture at 90˚ angle.

Normal contact forces and force distribution were recorded using an I-Scan™ (Tekscan Inc., Boston, MA) at 60 Hz. Each pressure-mapping sensor has an effective sensing area of 111.8 mm by 111.8 mm, which consists of an array of sensors that have the size of 2.5 mm by 2.5 mm. Two sensors were placed side by side to cover a large area of the aluminum plate. The sensors were calibrated at pressures of 34.5kPa and 206kPa (5PSI and 30PSI) with weights and a rubber sheet in between to ensure the weight is evenly distribute on all pixels. The palm, thumb and finger forces were determined by segmenting the hand force data to selected regions, similar to the method explained by Nicholas et al. 2012. These regions were subdivided by palm, and proximal (PP), middle (MP) and distal (DP) for each digit.

MaxTRAQ tracking software (Innovision Systems, Inc.) was used to track joint coordinates on the right hand, arm and shoulder (Innovision Systems, 2012; Figueroa et al., 2014). Four small video cameras were used to record the markers as the participants

16

completed each of the tasks. These coordinates were then analyzed to obtain joint locations and moments.

2.2.2. *Participants*

Twelve right-handed participants (6 males and 6 females) volunteered to participate in the study, giving written informed consent in accordance with IRB regulations. All participants were free of known movement disorders. The hand length percentiles of the participants ranged from 21st percentile to 96th percentile for male group, and from 3rd percentile to 81st percentile for females based on the 1988 ANSUR army male and female data (Gordon et al., 1989).

2.2.3. *Experimental Design and Procedure*

Participants were instructed to perform three exertions (100%, 30% and 10%MVC) perpendicular to an aluminum plate in -45˚, 0˚, 45˚ and 90˚ pitch at elbow height (Figure 2.4).
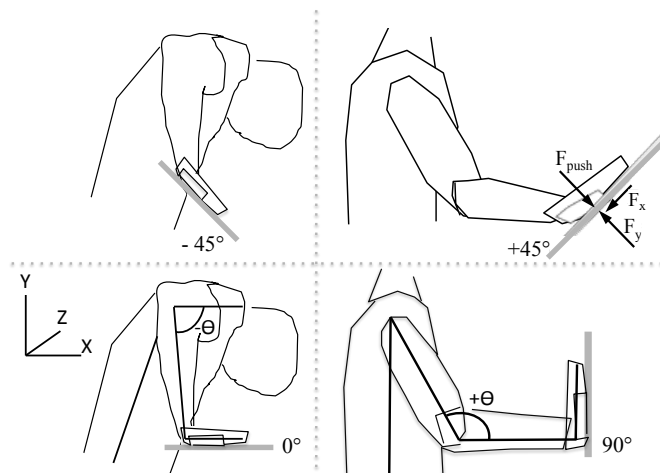
Figure 2.4 Forces were exerted perpendicular to a surface oriented -45°, 0°, +45°, 90°, and pitch with respect to horizontal. Friction force is represented as Fx and normal force as Fy. Bottom figures show elbow angle represented with a negative value (left) when facing downwards related to global Y-axis and positive (right) when facing upwards related to Y-axis.

Exertions were performed for 3 seconds using whole hand and fingertips (Figure 2.5).
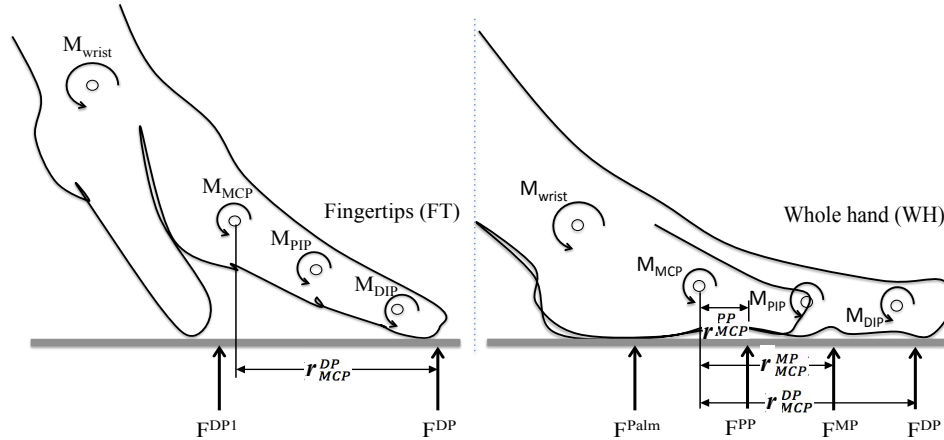
Figure 2.5 Exertions at 0° angle with fingertips (left) and whole hand (right) postures. Sample Free Body Diagram for moment at the MCP joint (M_{MCP}) produced by force (F^n) at each segment (n).

Fingertips exertions were constrained to the area of one pressure-mapping sensor. There were two replicates for each condition. Trials were blocked on plate orientation, with randomized selections between participants. Participants were allowed to become familiar with the tasks and to try different postures through practice sessions for each condition. First, participants were asked to perform maximum exertions (100%MVC). An average of the 100%MVC was used to record 30%MVC and 10%MVC conditions. The order of force exertions was randomized within the block for 30%MVC and 10%MVC. There was a minimum of two minutes of rest between exertions.

Reflective markers were attached to anatomical landmarks found by palpation. Specifically, they were placed on the lateral epicondyles, on the acromion process, on the ulna styloid process and radial styloid process, on the Metacarpophalangeal (MCP), Proximal Interphalangeal (PIP), Distal Interphalangeal (DIP) and Interphalangeal (IP) joints, and on the tip of each finger.

Vectors were defined between markers to compare postures among participants. Shoulder-Elbow, Elbow-Wrist vectors were used to compute elbow angle (Figures 2.3, 2.4). Elbow angle was defined on the anterior side of the arm (Knudson, D. 2007) and the global angle of the segment was defined as negative θ (-θ) when facing downwards related to global Y-axis and positive θ (+θ) when facing upwards related to global Y-axis (Figure 2.4). Linear distance from shoulder to tip of middle finger (Shoulder-to-D3) was used as a measure of arm straightness. The linear distance between shoulder and wrist joints (SW) was used to measure the angle (α) between the resultant force ($\boldsymbol{F_Y}$) (Figure 2.4) and shoulder-to-wrist vector ($\boldsymbol{r_{SW}}$). Where,

$$\cos \alpha = \frac{\boldsymbol{r_{SW}} \cdot \overrightarrow{\boldsymbol{F}_Y}}{|\boldsymbol{r_{SW}}| \left|\overrightarrow{\boldsymbol{F}_Y}\right|}$$

(2.1)

Moments (**M**) at each joint k (k=1, 2 3 or 4 for DIP, PIP, MCP, and Wrist, respectively) were computed as the product of the force $\vec{F}^n$ (n= DP, MP, PP and palm region) measured by the pressure-mapping sensor and the perpendicular distance r_k^n of force ($\vec{F}^n$) to joint k. Where,

$$\mathbf{M} = [\mathrm{M_{DIP}} \quad \mathrm{M_{PIP}} \quad \mathrm{M_{MCP}} \quad \mathrm{M_{Wrist}}]$$

$$\mathbf{M} = \begin{bmatrix} \mathrm{M_{DIP}^{DP}} & \mathrm{M_{PIP}^{DP}} & \mathrm{M_{MCP}^{DP}} & \mathrm{M_{Wrist}^{DP}} \\ 0 & \mathrm{M_{PIP}^{MP}} & \mathrm{M_{MCP}^{MP}} & \mathrm{M_{Wrist}^{MP}} \\ 0 & 0 & \mathrm{M_{MCP}^{PP}} & \mathrm{M_{Wrist}^{PP}} \\ 0 & 0 & 0 & \mathrm{M_{Wrist}^{Palm}} \end{bmatrix}$$

$$\mathbf{M} = \begin{bmatrix} \vec{F}^{DP}(r_{DIP}^{DP}) & \vec{F}^{DP}(r_{PIP}^{DP}) & \vec{F}^{DP}(r_{MCP}^{DP}) & \vec{F}^{DP}(r_{Wrist}^{DP}) \\ 0 & \vec{F}^{PP}(r_{PIP}^{PP}) & \vec{F}^{PP}(r_{MCP}^{PP}) & \vec{F}^{PP}(r_{Wrist}^{PP}) \\ 0 & 0 & \vec{F}^{MP}(r_{MCP}^{MP}) & \vec{F}^{MP}(r_{Wrist}^{MP}) \\ 0 & 0 & 0 & \vec{F}^{Palm}(r_{Wrist}^{Palm}) \end{bmatrix}$$

$$(2.2)$$

for whole hand condition and can be simplified to

$$\mathbf{M} = \begin{bmatrix} \vec{F}^{DP}(r_{DIP}^{DP}) & \vec{F}^{DP}(r_{PIP}^{DP}) & \vec{F}^{DP}(r_{MCP}^{DP}) & \vec{F}^{DP}(r_{Wrist}^{DP}) \\ 0 & 0 & 0 & 0 \\ 0 & 0 & 0 & 0 \\ 0 & 0 & 0 & 0 \end{bmatrix}$$

$$(2.3)$$

for fingertips condition. Figure 2.5 shows a 2D-Body Diagram for moment at the MCP joint (M_{MCP}). The independent variables in this experiment were sex, hand posture (fingertips/whole hand) and plate orientation, and the dependent variables were grip/pinch/push force, areas of hand force distribution, joint locations and joint moments.

2.2.4. *Statistical Analysis*

ANOVA was used (MINITAB®) to compare the effect of force (%MVC) on hand force distribution, finger placements and joint moments in fingertips and whole hand conditions. This analysis was also used to determine how resultant force was affected by plate orientation (-45˚, 0˚, 45˚ and 90˚) by hand posture (whole hand vs. fingertips). The mean values for each main effect and simple interaction were computed and significant factors were determined. Bonferroni adjustments were applied for multiple statistical tests. Significance was set at *p<0.05*.

2.3. Results

2.3.1. Force Exertions

Descriptive statistics of the participants are summarized in Table 2.1.

Table 2.1 Basic information about participants (mean ± SD)

Item	Male Group	Female Group
Age (years)	22.0 ± 2.6	21.5 ± 2.9
Stature (cm)	180.1± 5.5	166.4± 5.6
Hand Length (cm)	19.8 ± 1.1	16.7 ± 0.4
[a] Grip Strength (N)	483.0 ± 56.2	305.2 ± 15.2
[b] Thumb-index Finger Pinch Strength (N)	73.4 ± 5.3	45.4 ± 5.2

[a] Grip strength was measured with a Jamar® grip dynamometer with a grip span of 49mm
[b] Thumb-index Finger Pinch was measured with a B&L® pinch gauge

Males power grip and pinch strengths were significantly ($p<0.05$) greater than females (Table 2.1). Average maximum force pooled by sex for pushing at -45°, 0°, 45° and 90° degrees with the whole hand and fingertips are presented in Table 2.2.

Table 2.2 Total maximum exertions (N) per orientation for male and female groups while pushing with the whole hand (WH) and fingertips (FT) (mean ± SD)

Orientation (°)	Male Group Maximum Exertions (N)		Female Group Maximum Exertions (N)		Total Maximum Exertions (subjects pooled) (N)	
	WH	FT	WH	FT	WH	FT
-45	84.3 ± 7.0	58.4 ± 8.6	86.4 ± 21.5	51.5 ± 12.8	85.6 ± 9.0	55.3 ± 4.4
0	198.8 ± 3.3	91.1 ± 16.4	128.5 ± 29.4	62.9 ± 8.7	164.0 ± 44.5	82.0 ± 9.5
45	154.4 ± 21.1	84.8 ± 30.5	132.2 ± 11.6	56.2 ± 12.6	142.2 ± 38.7	74.4 ± 7.6
90	252.1 ± 38.7	114.1 ± 25.8	142.5 ± 42.7	76.1 ± 15.9	198.3 ± 54.8	94.9 ± 10.6

The male group was consistently exerted more force than the female group (except for the -45˚pitch conditions). Average maximum force for pushing with whole hand at 0˚, 45˚ and 90˚ plates was 49% higher than for female ($p<0.01$); average maximum for pushing with the fingertips was 62% greater for males than females ($p<0.01$). There was no significant sex difference ($p>0.05$) for pushing on the -45˚plate.

Grip strength was 6.6 times greater than pinch strength (p<0.01). Grip strength (Table 2.1) was 4.6 greater than flat hand average maximum and 7 times greater than fingertips average maximum while pushing in a downward and inward direction (-45°- Table 2.2). Grip strength was 2-3 times greater than the average maximum push with the whole hand and 4.2- 5.3 times higher than fingertips average maximum exertion while pushing downward (0°- Table 2.2) and away from the body (45° and 90°- Table 2.2). Maximum thumb-index finger pinch strength (Table 2.1) was 0.7 and 1.1 times the average maximum force exerted down and inward at -45° (Table 2.2) with the whole hand and fingertips, respectively. Thumb-index finger pinch strength was about 0.4 times the average maximum force exerted with the whole hand and about 0.7 times the exerted force with the fingertips downward at 0° or away from the body at 45° and 90° (Table 2.2)

2.3.2. *Force Distribution per Hand Segment*

Normal forces per segment for each orientations and each hand posture are shown in Table 2.3.

Table 2.3 Finger force distribution (normal force) pushing the plate with 4 orientations (-45˚, 0˚, 45˚ and 90˚) and 2 hand postures (whole hand-WH and fingertips- FT) (mean ± SD) (pooled for all participants)

% MVC	Object Orientation (°)	Hand Posture	Forces (subjects pooled) (N)					Palm Region	Total
			Thumb	Index	Middle	Ring	Little		
100	-45	WH	13.5 ± 4.0	4.8 ± 1.9	4.5 ± 1.7	3.9 ± 1.6	2.7 ± 1.2	14.1 ± 12.5	85.6 ± 9.0
		FT	18.0 ± 8.0	10.8 ± 4.3	8.9 ± 3.0	8.4 ± 3.2	7.1 ± 3.9		55.3 ± 4.4
	0	WH	19.8 ± 6.7	2.8 ± 1.6	5.7 ± 3.1	7.9 ± 4.5	7.3 ± 3.2	110.6 ± 31.2	164.0 ± 44.5
		FT	29.7 ± 12.9	14.5 ± 4.0	12.4 ± 5.8	11.5 ± 6.3	9.0 ± 5.5		82.0 ± 9.5
	45	WH	16.4 ± 5.5	2.5 ± 0.9	4.7 ± 1.8	6.3 ± 2.7	7.0 ± 2.8	102.3 ± 19.7	142.2 ± 38.7
		FT	28.3 ± 12.4	12.1 ± .02	10.4 ± 5.0	12.2 ± 7.7	10.3 ± 5.7		74.4 ± 7.6
	90	WH	20.2 ± 8.6	3.5 ± 1.5	5.9 ± 2.8	8.0 ± 3.4	9.9 ± 4.1	139.9 ± 47.8	198.3 ± 54.8
		FT	31.8 ± 14.0	14.3 ± 5.2	14.4 ± 6.8	11.5 ± 6.6	10.8 ± 5.8		94.9 ± 10.6
30	-45	WH	4.2 ± 1.6	1.5 ± 0.6	1.2 ± 0.5	1.1 ± 0.6	0.8 ± 0.3	3.8 ± 3.9	12.5 ± 1.5
		FT	5.0 ± 3.0	2.6 ± 0.9	2.7 ± 1.2	2.3 ± 0.9	2.0 ± 1.0		14.7 ± 1.2
	0	WH	5.5 ± 2.0	1.0 ± 0.3	1.7 ± 1.0	2.3 ± 1.0	2.0 ± 0.7	33.8 ± 10.7	46.3 ± 12.9
		FT	8.6 ± 3.8	4.7 ± 2.2	3.4 ± 1.3	3.3 ± 1.3	3.2 ± 2.4		23.2 ± 2.3
	45	WH	4.9 ± 2.4	0.8 ± 0.3	1.2 ± 0.7	1.9 ± 0.9	1.9 ± 0.6	29.7 ± 5.1	40.5 ± 11.4
		FT	9.1 ± 6.2	4.0 ± 1.2	3.1 ± 1.4	2.9 ± 1.5	3.0 ± 1.7		22.1 ± 2.7
	90	WH	6.9 ± 4.0	0.8 ± 0.5	2.0 ± 1.0	2.6 ± 1.4	2.5 ± 1.0	42.7 ± 16.3	57.5 ± 16.4
		FT	7.2 ± 2.9	5.2 ± 2.1	4.2 ± 2.3	3.8 ± 2.3	3.6 ± 3.4		24.1 ± 1.5
10	-45	WH	1.6 ± 0.5	0.6 ± 0.2	0.5 ± 0.2	0.5 ± 0.2	0.3 ± 0.1	1.5 ± 1.5	5.0 ± 0.6
		FT	1.7 ± 0.9	0.8 ± 0.5	0.9 ± 0.7	0.9 ± 0.4	0.8 ± 0.3		5.1 ± 0.4
	0	WH	10.2 ± 11.7	3.9 ± 5.1	3.9 ± 4.9	4.1 ± 5.1	3.7 ± 4.6	39.4 ± 48.3	65.3 ± 14.2
		FT	2.6 ± 1.3	1.7 ± 0.6	1.2 ± 0.6	1.1 ± 0.7	1.4 ± 1.1		8.1 ± 0.6
	45	WH	1.4 ± 0.9	0.2 ± 0.2	0.5 ± 0.3	0.6 ± 0.4	0.7 ± 0.4	11.1 ± 3.3	14.6 ± 4.3
		FT	3.7 ± 4.9	1.0 ± 0.6	0.8 ± 0.5	0.9 ± 0.6	0.9 ± 0.6		7.3 ± 1.2
	90	WH	2.3 ± 1.2	0.4 ± 0.3	0.7 ± 0.4	1.0 ± 0.7	1.1 ± 0.5	13.8 ± 4.7	19.2 ± 5.3
		FT	3.4 ± 2.7	2.6 ± 1.9	1.9 ± 2.1	1.7 ± 1.8	1.4 ± 2.3		11.0 ± 0.8

Thumb force was 12% of the total force when pushing with whole hand and 38% of the total force for pushing with the fingertips. The sum of finger forces (excluding thumb) corresponded to 62% of the total force for pushing with the fingertips, but only 15% of the total force for pushing with the whole hand. Seventy-three percent of the total force was exerted with the palm. When constrained to push with just the fingertips, the force exerted by the thumb increased by 37% and the sum of the force exerted by the fingers increased by 50% (Figure 2.6) for all conditions.
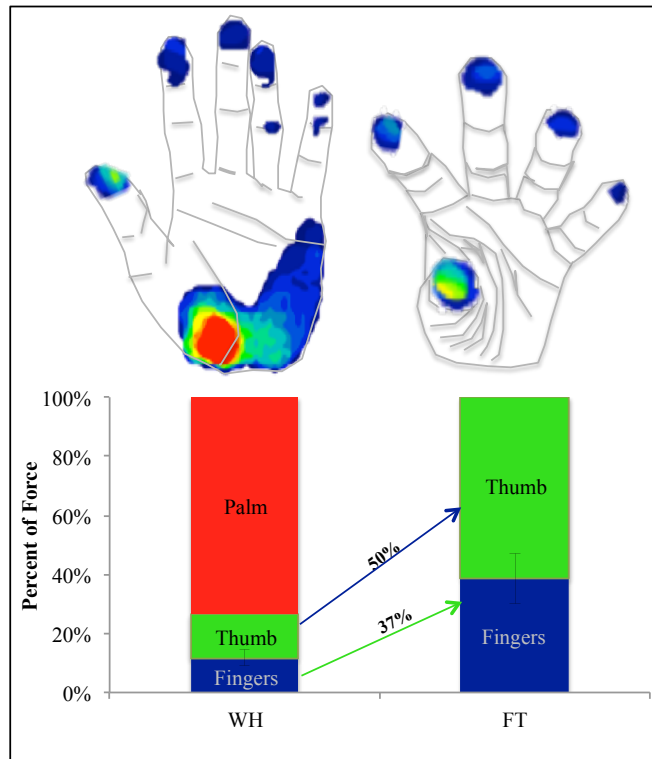
Figure 2.6 Force distribution per segment when pushing perpendicular to the flat surface at maximum force exertion (100 %MVC) in 2 hand postures, a) fingertip (FT) and b) whole hand (WH) (pooled for all participants) at 0˚ pitch. Colors range from Red for highest force value to Dark Blue for lowest values.

2.3.3. Posture Analysis

Shoulder-D3 distances while pressing a flat surface per sex under whole hand posture for

0° pitch are shown in Figure 2.7.
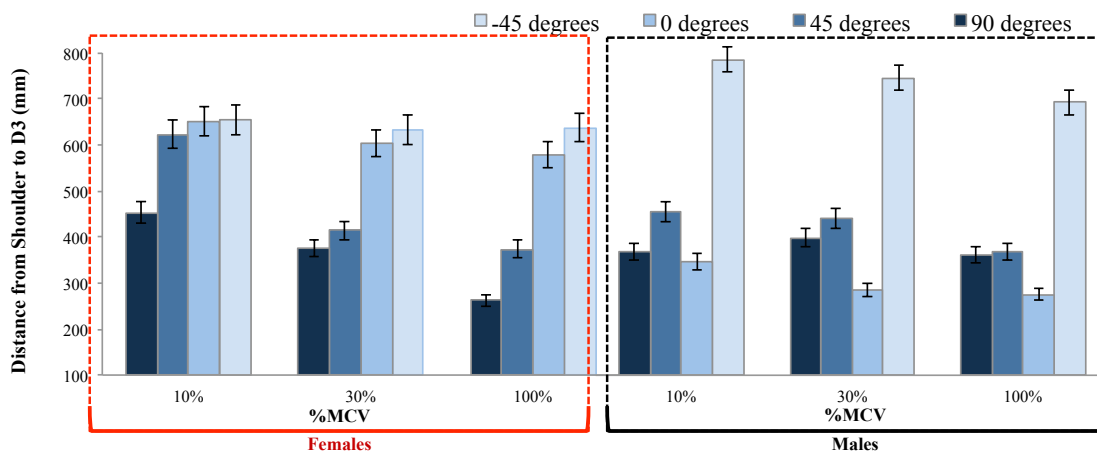
Figure 2.7 Linear distance of shoulder to tip of middle finger (Shoulder-to-D3) while pressing the plate with whole hand posture in 4 orientations (45˚, 0˚, 45˚ and 90˚) under 3 conditions (100, 30 and 10 %MVC).

24

The angle (α) between the resultant hand force (FY) and the vector corresponding to the linear distance between the shoulder and wrist joints (RSW) for 0˚and 90˚ orientations by sex, and hand posture are shown in Table 2.4.

Table 2.4 Angle (α) between resultant force (F_Y) and shoulder-to-wrist vector (R_{SW}) while pressing perpendicular to a flat surface under 0˚and 90˚orientations and 2 hand postures (whole hand-WH and fingertips- FT).

Object Orientation (°)	% MVC	Hand Posture	α (Degrees) Males	Females
0	100	WH	12.3	6.41
		FT	15.4	9.74
	30	WH	59.9	44.1
		FT	66.9	38.3
	10	WH	36.7	41.4
		FT	43.2	42.7
90	100	WH	8.04	6.52
		FT	7.88	8.31
	30	WH	48.4	37.9
		FT	51.6	43.7
	10	WH	52.7	26.0
		FT	63.8	47.8

Angle (α) between resultant force (F$_Y$) and shoulder-to-wrist vector (RSW) was different in low %MVC vs. 100 %MVC ($p < 0.05$) when pushing in both fingertips and whole hand conditions. Elbow angles for each hand posture under 0° pitch are shown in Figure 2.8.
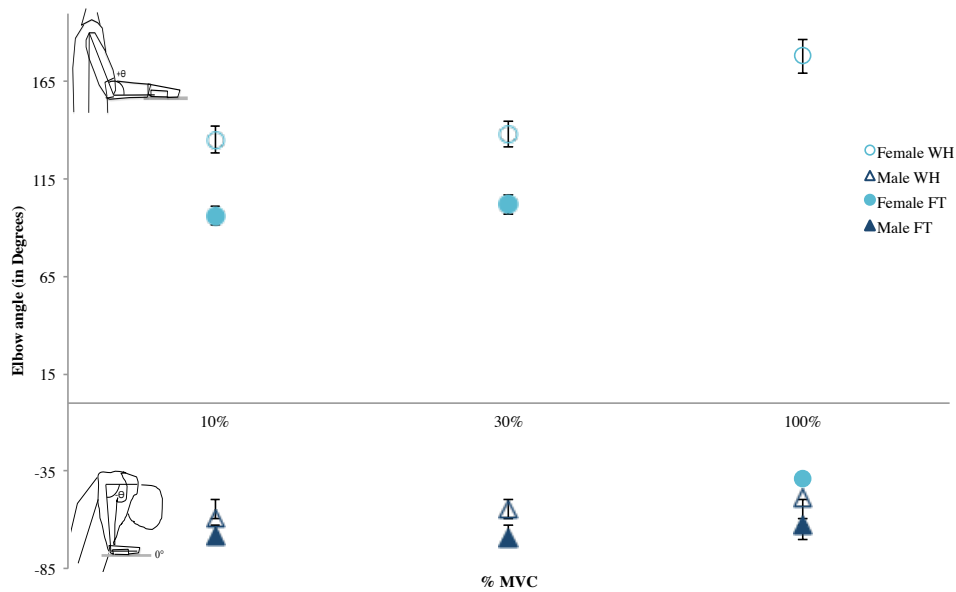
Figure 2.8 Elbow angles for female group (in red) and male group (in blue) pressing the plate in fingertip (FT) and whole hand (WH) postures at 0° pitch under 3 conditions (100, 30 and 10 %MVC).

Females acquired a posture with shoulder abduction and negative elbow angle (Figure 2.4, Figure 2.8) during fingertip posture at 100% MVC conditions. For the rest of the conditions female elbow angle had a positive value (Figure 2.8). Males elbow angle involved shoulder abduction without significant change between force levels (p>0.05) (Figure 2.8) during all conditions.

2.3.4. Joint Moments

Moments of the wrist, thumb and finger joints were calculated when pushing the plate in 4 orientations (-45˚, 0˚, 45˚ and 90˚) with fingertips and whole hand postures for 100%MVC exertions (Table 2.5).

26

Table 2.5 Joint moment magnitudes when pushing perpendicular to a flat surface with 4 orientations (-45˚, 0˚, 45˚ and 90˚) and 2 hand postures (whole hand-WH and fingertips- FT) during 100%MVC condition for females (upper) and males (bottom).

	Object Orientation (°)	Hand Posture	Females Finger Joint Moment Magnitudes (N*m)														
			Thumb		Index			Middle			Ring			Little			Wrist
			IP	MCP	DIP	PIP	MCP	DIP	PIP	MCP	DIP	PIP	MCP	DIP	PIP	MCP	
Females	-45°	WH	0.29	0.75	0.14	0.26	0.61	0.20	0.42	0.77	0.18	0.36	0.69	0.12	0.30	0.65	1.9
		FT	0.41	0.86	0.26	0.54	0.74	0.32	0.64	0.86	0.28	0.52	0.79	0.24	0.49	0.70	1.3
	0°	WH	0.57	1.71	0.32	0.77	1.09	0.54	0.82	1.31	0.35	0.83	1.17	0.29	0.79	0.95	1.88
		FT	0.83	2.62	0.43	0.91	1.52	0.76	1.37	1.99	0.64	1.01	1.73	0.41	0.85	1.56	3.0
	45°	WH	0.34	1.12	0.20	0.39	0.88	0.38	0.63	0.95	0.33	0.67	1.01	0.15	0.42	0.37	1.4
		FT	0.46	1.39	0.34	0.63	1.16	0.48	0.99	1.33	0.38	0.71	0.87	0.28	0.66	1.25	1.9
	90°	WH	0.56	1.53	0.24	0.68	0.95	0.45	0.75	1.22	0.42	0.76	1.04	0.21	0.71	0.88	1.7
		FT	0.77	2.20	0.39	0.88	1.40	0.63	1.12	1.68	0.53	0.93	1.61	0.46	0.80	1.42	3.2
	Object Orientation (°)	Hand Posture	Males Finger Joint Moment Magnitudes (N*m)														
			Thumb		Index			Middle			Ring			Little			Wrist
			IP	MCP	DIP	PIP	MCP	DIP	PIP	MCP	DIP	PIP	MCP	DIP	PIP	MCP	
Males	-45°	WH	0.34	0.88	0.17	0.36	0.75	0.28	0.5	0.95	0.25	0.44	0.99	0.16	0.4	0.81	2.9
		FT	0.53	1.12	0.35	0.65	1.04	0.45	0.92	1.08	0.39	0.65	1.05	0.31	0.63	0.83	1.9
	0°	WH	0.67	2.32	0.44	0.97	1.54	0.65	1.13	1.77	0.41	1.2	1.54	0.41	1.05	1.15	2.7
		FT	1.15	3.76	0.5	1.09	1.96	1.08	1.68	2.48	0.9	1.19	2.5	0.51	1.05	1.84	3.7
	45°	WH	0.42	1.36	0.26	0.47	1.01	0.51	0.73	1.09	0.41	0.78	1.46	0.17	0.55	0.43	1.9
		FT	0.6	1.81	0.44	0.83	1.69	0.69	1.21	1.75	0.47	0.94	1.03	0.36	0.8	1.62	3.0
	90°	WH	0.77	2.07	0.31	0.88	1.26	0.54	1.08	1.71	0.48	0.98	1.32	0.24	0.83	1.14	2.3
		FT	0.99	3.09	0.48	1.01	1.98	0.73	1.53	2.33	0.75	1.32	2.21	0.66	1.07	1.73	3.7

On average, finger joint moment magnitudes were 30% higher when pressing with fingertips vs. whole hand postures. However, during 0˚, 45˚ and 90˚ orientations, wrist moments were 36% higher when pressing with fingertips vs. whole hand postures but were 50% lower when pressing with fingertips vs. whole hand postures during exertions in the -45˚ orientation.

Thumb MCP moment magnitudes were 65% higher than its IP joint for whole hand posture and 63% during fingertips posture. On average, MCP moment magnitudes for the rest of the fingers (index to little fingers) were 70% higher than DIP and 34% higher than PIP during whole hand posture and 67% and 37%, respectively during

27

fingertips posture. Overall, wrist moment magnitude was 49% higher than MCP3 during fingertip exertions and only 11% higher than the moments on the MCP1 joint.

2.4. Discussion

This study was primarily concerned with exertions of the thumb, fingers and palm, which are in the same direction pushing on a flat surface. Hand strength measurements are typically based on maximum finger flexion against an object supported by the palm and thumb (Zhou, 2013; Salimi et al. 2003; Hamilton et al., 1992), a cylinder (Wu et al., 2012), or during push/pull tasks while holding a handle (Szychlinska et al., 2017; Nicholas et al., 2012; Di & Keir, 2010; Seo et al., 2007; Das & Wang, 2004; Chaffin et al., 1983).

In power grip the fingers are flexed against an object supported in the palm (Szychlinska et al., 2017; Seo et al., 2007; Napier, 1956) so that the fingers forces act in opposition to the thumb and palm. When pushing with a flat hand, the fingers, thumb and palm all exert force in the same direction. In pinch grip the thumb acts in opposition with one or more fingers, where the thumb or opposing fingers limits strength (Budgeon et al., 2008). Pinch strength and pressing on a flat external surface with fingertips are biomechanically similar; in both cases forces are exerted with the distal portion of the fingers. When pressing a flat surface with the fingers and thumb, all are exerted in the same direction so that the average maximum force is related to the sum of individual fingers and the thumb. However, results from Tables 2.1 and 2.2 show that grip strength was considerably greater than both whole hand and fingertips average maximum push exertions. Maximum thumb-index finger pinch strength was less than whole hand

average maximum push exertions and similar than fingertips average maximum push exertions.

Results from this study show that greater normal contact force can be exerted with the base of the palm than with the fingertips (Table 2.3, Figure 2.6) when pushing away from the body at 45° and 90° or downward at 0° (Table 2.2). The results also show that more force can be exerted horizontally at 90° than downward at 0° (Tables 2.2 and 3). Though, horizontal forces are limited by shoe-floor traction (Fischer et al., 2013), hand-handle friction (Seo et al., 2010), anthropometry (Chaffin et al., 1983), balance (Rancourt & Hogan, 2001) and strength of the legs, trunk and upper limbs (Hoffman et al., 2007). Finger joints are the weakest links in the kinematic chain. These are unable to counteract the load moments produced by the DP segments average maximum exertions away from the body, explaining the differences among average maximum forces for pushing with the fingertips versus the whole hand (Table 2.2). There is no reason to believe that the ability of the body to exert force with the base of the palm should be limited by hand strength when pushing with the whole hand.

Results also show that substantially more force can be exerted in a direction away from the body at elbow height. It appears that participants were unable to use their body weight when they reached over the plate and pushed in a downward and inward direction (-45° Table 2.2). As a result of this reduced force, finger strength was not limiting in this case and there were no significant differences between the average maximum forces exerted with the whole hand and the fingertips during -45° surface orientation.

It is not possible to determine which finger joint is limiting, but it is reasonable to assume that participants position their hands to equalize the relative moments (%MVC) about each joint (An et al. 1984; Bean et al. 1988). This is consistent with previous findings related to finger placement while grasping a flat plate (Zhou, 2013; Salimi et al. 2003), a cylinder (Wu et al., 2012), and in push/pull tasks (Nicholas et al., 2012) where participants modified digit positions and scaled fingertips forces to obtain higher comfort and balance based on the external torque created by changes in weight and center of mass location. It follows that all of inter-digit joints are at or near maximum during average maximum push exertions (Table 2.4).

Similarly it appears that participants position their bodies within the constraints of their workspace minimizing peak shoulder joint loads that would limit exertions. In all cases, participants leaned towards the surface for optimum force exertions and for minimizing the moment arm for the shoulder joint (Table 2.5, Figure 2.9).

		Moments (N•m)		
Joint		Posture A	Posture B	Posture C
Shoulder	Female	11.5	42.0	17.5
	Male	15.4	71.6	31.8
Elbow	Female	8.5	5.0	25.0
	Male	9.7	8.0	35.7
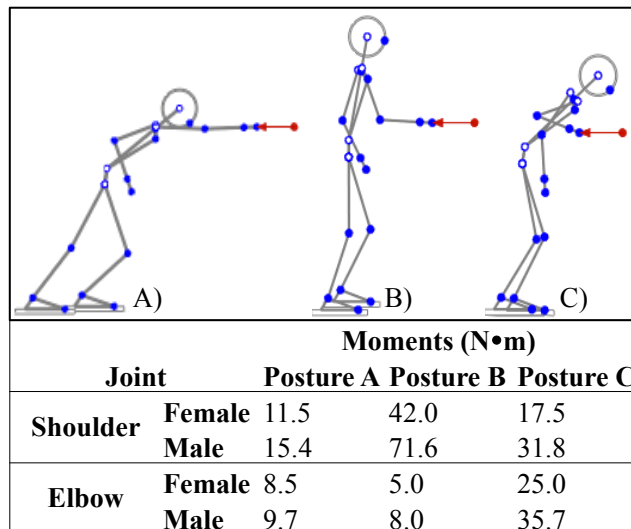
Figure 2.9 Sample of shoulder and elbow moment magnitudes while pushing at maximum exertions (198N for males and 128.5N for females) at 90° plate angle for 50th percentile females and males while pushing at elbow height leaving forward with (a) a straight arm, (b) without shoulder abduction, and with (c) shoulder abduction.

Maximum push (Table 2.2) and the University of Michigan 3D Static Strength Prediction Program (3DSSPP ™) were used to measure shoulder and elbow loads during representative postures while pushing the plate in four orientations (-45˚, 0˚, 45˚ and 90˚) with a whole hand. Similar to the results obtained in this study (Table 2.5), shoulder loads were limiting during all representative postures in Figure 2.9. Under all %MVC conditions, males maintained an arm posture involving the anterior side of the elbow facing down when pushing downwards (0°) with the whole hand (Figure 2.4, Figure 2.8). Females only acquired the same posture while pushing downward (0°) with the fingertips during 100%MVC (Figure 2.4, Figure 2.8) and while pushing forward (90°) with the whole hand during 100%MVC (Figure 2.7). This posture included shoulder abduction, and high wrist flexion with radial deviation (Figure 2.4). While this is one of the poorest upper body positions, which contributes to upper extremity musculoskeletal disorders (Garg & Kapellusch 2011), it suggests that the elbow joint didn't limit their strength and all efforts were focused on minimizing the moment arm between the resultant force and the shoulder joint.

For fingertip exertions, it was observed that participants leaned towards the surface with a straight arm when pushing forward (45° and 90°), also minimizing the angle between the resultant force and the shoulder to wrist vector (Figure 2.10a, Table 2.5). 3DSSPP ™ was used to calculate elbow and shoulder moments during three possible arm configurations while pushing forward (90°) (Figure 2.10).
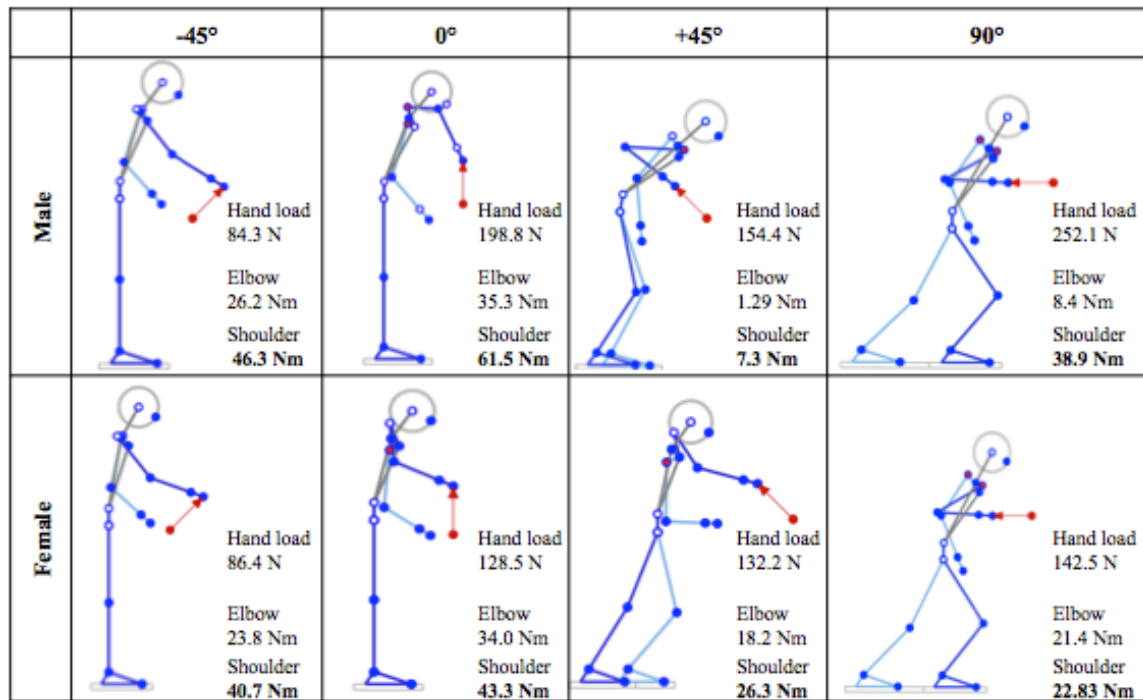
Figure 2.10 Representative shoulder and elbow moment magnitudes of the right arm while pushing a plate in 4 orientations (-45˚, 0˚, 45˚ and 90˚) at elbow height. Hand loads are maximum exertions with whole hand from Table 2.2.

Shoulder and elbow joint moments were affected by the different arm postures when pushing forward (90°). Both elbow and shoulder loads were minimized with a straight arm (Figure 2.10a). Shoulder loads were minimized when leaning towards the object, minimizing the distance between the resultant force and the shoulder joint (Figure 2.10c). As seen in sample postures in Figure 2.10, larger moment arms lead to greater loads that are applied to the joint axis through leverage. Thus, by aligning each arm segment to that axis, the loads on shoulder and elbow decrease. Overall, participants chose either postures similar to Figure 2.10a and c, minimizing shoulders moment arm, rather than a posture similar Figure 2.10a, which minimizes elbow loads. Although arm postures were usually different between sex, and between low %MVC and 100 %MVC ($p<0.05$) in both fingertips and whole hand conditions, results show similar moment arms and angles between the resultant force and the shoulder joint (Table 2.5).

Thumb and finger forces are consistently 40-50% less when pushing with the whole hand than with the fingertips (Table 2.3). A similar trend exists for finger moments (Table 2.5), but the moment differences between whole hand and fingertips are closer to 30%. The differences between forces and moments can be attributed to an increase in moment arms between the fingertips and joint centers while pushing with a flat hand. Maximum finger moments might be expected in both cases, but it is likely that the exertions with a flat hand on the 90°, 45° and 0° push plates are limited by traction, leg, torso and shoulder strength. Work by Elkus and Basmajian (1973) demonstrated that finger flexor muscles relax when ligaments can support hand loads. In this case, the fingers are partially relaxed when the loads are transmitted directly into the long axis of the upper limb. Given the resultant push force vector is aligned with the shoulder joint, it can be assumed that the trunk lower limbs or traction limits the force.

Forces are not distributed equally over the palmar surface of the hand. Thumb and finger forces during whole hand posture were concentrated primarily on distal segments vs. middle and proximal segments (Figure 2.6). This is consistent with previous studies that analyzed the ratio of the contact forces applied on the distal, middle, and proximal segments during grip exertions (Chao et al., 1989; Wu et al., 2012). The greatest force, 72-75% of total force, was exerted over the base of the palm followed by 11-13% with the thumb for exertions at 90°, 45° or 0° push plate angles (Table 2.3). While pushing at -45° plate angles, the force over the palm was reduced to 32% of the total force while the thumb force was increased to 31%; suggesting that thumb moments were the limiting joint during the -45° case.

Several studies examined relative finger strength for grip and pinch exertions (Barter et al. 1958; Fransson and Winkel 1991; Swanson et al. 1970; Hazelton et al. 1975; Seo et al., 2007). In all of these studies, the middle finger was the strongest, accounting for approximately 33% of the sum of all fingers. The index finger accounted for 21-31% as compared to the sum of all fingers, the ring finger for 22-26% and the little finger for 13-18%. For comparison purposes, in this study the relative finger forces (excluding thumb) for pushing away from the body or downward with the whole hand (90°, 45°, 0° - Table 2.3) were 12-13%, 22-24%, 25-33% and 17-36% for index, middle, ring and little fingers, respectively. For pushing inward and down (-45° - Table 2.3) the relative forces were 30%, 28%, 25% and 17% for index, middle, ring and little fingers, respectively. The relative finger forces (excluding thumb) for pushing away from the body or downward with the fingertips (90°, 45°, 0° - Table 2.3) were 27-31%, 23-28%, 23-27% and 19-23% for index, middle, ring and little fingers, respectively. For pushing inward and down (-45° - Table 2.3) the relative forces were 30%, 28%, 25% and 17% for index, middle, ring and little fingers, respectively. It appears that reaching over the plate (-45°) affected the orientation of the hand and the resulting load distribution (Table 2.2), but there were no significant changes between relative finger loads during different % MVCs.

Data obtained in this study can be used to develop empirical models that can be incorporated into hand models for ergonomic and/or biomechanical analyses. This information can then be used to design work tasks that might be subjected to high hand force while holding or positioning an object such as installing panels during auto assembly lines. It can also be used to design and/or analyze workplaces, household

spaces and products for which people would support their object or push against the surfaces. These surfaces and objects should be able to fit the entire hand and should be positioned between 0° (horizontal) and 90° (vertical).

2.5. Conclusion

An experiment was performed in which participants were asked to push with a single arm on a flat surface at elbow height. Results obtained in this study can help to understand and predict hand postures and finger loads based on object orientation and force required.

Object location, space for hand placement, and physical space should be considered when designing workplaces or household spaces. Results from this study (Tables 2.2 and 2.3) suggest that when a person is expected to press or support their body, spaces should be designed to provide enough space to fit the palm, especially if maximum exertions are required. If a person can use the whole hand to press on a surface, they will do so.

Although the advantages for pressing a surface with the whole hand are clear, some tasks require only the fingertips. We see this in sports, while grabbing a ball or in the starting position of race. This posture is also common in everyday activities, such as holding or positioning items against a surface when cooking, writing or performing other manual tasks. Using the fingertips adds a higher level of control and precision (Napier, 1956) over an object when lower exertions are required. Thus, it is important to understand the biomechanics involved and strength capabilities when supporting our body or pressing a surface with them.

This work can be used to prevent awkward postures and increase comfort for all users through improved design. A workspace should include enough clearance to accommodate the whole population so that the worker can stretch their arms if needed, to exert force and reach maximum force capability without the need of acquiring awkward postures. If the task could involve a person supporting their body on a surface or object (e.g. getting up from a chair, pressing on panels), enough surface space should be provided on that object to fit the whole hand to reduce risk of potential accidents. Software such as the 3DSSPP (TM) that includes posture data and male/female anthropometry (Drillis R. and Contini R., 1966) can be use to determine the required space and heights for the selected range of workers.

Joint moment calculations, finger force distributions, and joint moment ratios can be used to compare strength capabilities from one position to another and for further biomechanical analyses. These parameters can be used when designing work tasks to ensure a balance between safety, comfort and productivity.

2.5.1. *Limitations and Future Work*

This study considered only the normal force component due to the limitation of the pressure mapping system. Object orientation could result in significant friction forces and affect the magnitude of the resultant force. Future studies should examine the effect of friction on hand force distribution and hand placement. Average maximum whole hand forces exerted perpendicular to a flat surface may be limited by whole body strength and traction. This idea could be tested by providing external support for the body so that

foot friction is not limiting and subjects can assume a position of average maximum force.

Hand placement was constrained by the pressure sensor area. However, there was enough space for participants to place their fingers without constraints (Zhou, 2013; Duemmler et al., 2008). It is likely that participants would demonstrate similar behavior in a study with a larger pressure sensor area.

2.5.2. *Acknowledgements*

CHAPTER 3 3D Hand Anatomical Representations and Coordinate Systems Based on CT-Scan Images

Abstract

The International Society of Biomechanics (ISB) provides recommendations for defining coordinate systems (Wu et al., 2005) for 3D bone surfaces but doesn't specify how to find them. This study aimed to 1) develop quantitative and reproducible procedures to determine coordinate systems of hand bone segments, and 2) generate 3D-hand skin and bone models extracted from Computed Tomography. CT scans from the same hand in five different postures were used to extract bone shape and skin surface of the hand, and to develop a generalized method for determining global and local coordinate systems for each segment. All vertices of each bone segment were aligned using the iterative closest point algorithm with Procrustes alignment with the purpose of evaluation the manual segmentation process for shape extraction, and the methods for generating coordinate systems based on ISB recommendations while using a combination of principal component analysis and bone landmarks. Mean Euclidean distance, defined as the distance between centroids of two 3D meshes, was used to evaluate the geometry extraction process. The variance, defined by the rotation error of same axis between two 3D meshes, was used to evaluate the coordinate system of each bone. No difference was

found between different postures for each bone, with mean Euclidean distances less than 0.2 (mm), validating the segmentation process and coordinate systems.

3.1   Introduction

Computerized hand models have many applications for evaluating hand function in biomechanics (Chaffin, 2008), ergonomics (Seo et al., 2007; Frederick and Armstrong 1995; Buchholz and Armstrong, 1992), medicine (Westwood, 2002), and robotics (Bierbaum et al., 2009; Liu et al., 1989). This work is particularly concerned with the spatial relationship between the hand and externals surfaces/objects. This study aims to develop procedures and models for describing bone and skin surfaces that determine the shape, size and movements of the hand.

Early hand models were based on simplified representations of hand segments. Buchholz developed a kinematic model to predict prehensile postures by using ellipsoids and elliptical cylinders to represent finger segments and objects, respectively (Buchholz and Armstrong, 1992). Choi and Armstrong developed a model by representing bones with a link system and skin surface with truncated cones (Armstrong & Choi, 2008). This model was used to predict hand placement based on a contact algorithm (Choi, 2008). Although ellipsoids and truncated cones can provide posture predictions, models can be improved by using realistic representations of bone geometry to determine the kinematics.

Detailed bone geometry is needed for developing realistic models and determining differences in forces of joints, tendons and muscles. Therefore, an anatomically based coordinate system for each segment should be created to represent

realistic movement of one bone around another. Realistic skeleton geometry, as well as good estimates of the joint structures and surface deformation, can be obtained using Three-dimensional (3D) measurements from medical images (McInerney, T., & Terzopoulos, 1994).

3D images of various body parts, including the hands, are routinely used for diagnostic and research purposes. The 3D images generated from these procedures are not suitable for manipulation in its native form (DICOM). It is necessary to segment these files into smaller files that correspond to each segment of the hand. Miyata et al. 2007 used Magnetic Resonance imaging (MRI) modality to extract the surface of the cancellous bone (spongy bone) to represent a bone surface mesh for hand bones, resulting in a mesh that is smaller than the actual bone surface (cortical bone area). Cancellous bone was used rather than cortical bone because in MRIs cortical bone is hard to distinguish since it is shown in a low density (Miyata et al., 2007; McKinnis, 2010). In CT Scans, cortical bone (actual bone surface) is shown in high density. Thus, CT Scans can be used to create accurate representations of 3D bone surfaces for simulation models, as it provides the most precise details of bone shape and size (Thorhauer et al., 2010; Figueroa et al. 2016; Reed et al., 2014; McKinnis, 2010).

There is a need to describe 3D bone and skin surfaces geometries and their coordinate systems for realistic hand modeling. The most common approach for computing the alignment of 3D objects is the principal component analysis method (PCA) (Zhang and Chen, 2011; Chaouch and Verroust-Blondet, 2009), which normalizes the directions of the surface vertices/points. Although PCA method produces good

estimations of three principal axes of a 3D surface in space, there is a level of uncertainty due to bone curvature and surface details, especially along the distal and proximal ends of long bones (Liu et al., 2006). For long bones, such as phalanges and radius and ulna, the International Society of Biomechanics (ISB) defines the center of the shaft as the center symmetry and the direction of the shaft as the principal axes of symmetry corresponding to the long axis (local Y-axis) (Wu et al., 2005).

ISB provides recommendations for defining coordinate systems of 3D-bone surfaces (Wu et al., 2005) with the aim of encouraging consistency among researchers. However, Wu et al. does not specify how to determine these coordinate systems in a quantitative and repeatable method, and neither includes specific considerations for developing kinematics for hand modeling purposes such as identifying the origin of long bones in the middle of the bone along the long axis. However, it is more beneficial for hand modeling to establish the origin of phalanges at the proximal end. After decomposing medical images into bones and other tissue types, a current challenge is to maintain the spatial relationship between the different segments after segmentation for re-integrating them. Thus, maintaining a consistent global coordinate system is important for developing realistic hand models from medical images. On the other hand, localized coordinate systems are essential in digital human modeling for multiple applications such as, shape superimposing, assessing surface deformation and shape differences, and for creating representative surfaces by fitting a template for statistical analysis and finite element modeling (Klein et al., 2015). Additionally, accurate models of hand skeleton can be used to determine joint distances. These can be used as a metric to establish a minimum constraint for finger kinematics between consecutive segments.

This study aimed to 1) develop models that describe 3D-bone and skin surface geometries based on CT Scans, and 2) develop procedures to determine hand skin and bones coordinate systems that can be applied to any hand.

3.2 Methods

3.2.1 3D Bone and Skin Models using from CT Images

CT scan images of one male left hands in five postures (Figure 3.1) with a hand length of 0.195 m, hand breadth of 0.086 m and hand thickness of 0.027 m, without existing pathologies, were collected using a resolution of 512 x 512 pixels with 0.47mm between slices and an in-plane resolution ranging from 0.3 mm to 0.67 mm. Individual 3D surfaces of twenty-seven hand bones (Appendix A), two forearm bones, and skin were created through manual segmentation using Amira ® software (v. 5.2) with a Hounsfield Unit threshold of -200 for bone surfaces and -260 for skin surfaces.

Posture	Short Term	Description
Posture 0/ Template	Flat Hand	Pressing the hand against a flat surface in pronation at the forearm, minimum wrist ulnar/radial deviation and minimum flexion.
Posture 1	Resting Hand	Fingers are relaxed and wrist has ~35 degree flexion
Posture 2	Lateral Pinch	Holding a coin with the thumb and index finger
Posture 3	Power Grip	Holding a cylinder with a 90 mm diameter
Posture 4	Pinch Grip	Pressing the tips of 4 fingers with the thumb
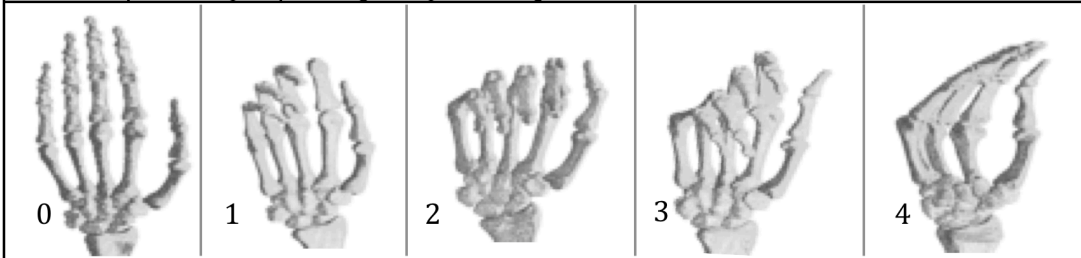
Figure 3.1 Description of the five hand postures used for the development of models of bone and skin for the forearm, wrist and hand.

Using an automated script in MeshLab (v. 1.3.2, sourceforge.net), the individual 3D meshes (in .PLY format) were simplified using the quadric edge collapse decimation.

The quadric edge collapse decimation tool, developed by Garland (1999), has been used in digital human model studies, such as for developing statistical shape models of the femur (Klein et al., 2015), and for analyzing endoscopy images (Pratt et al., 2010). The target resolution per bone was selected depending on the complexity of the bone geometry and ranged from 130,000 faces for the skin, to 15,000 faces for the distal and middle phalanges.

All decimated 3D-meshes for left hands were then imported into MATLAB (MathWorks, Natick, MA) and reflected along the long axis to generate 3D right-hand bone and skin polygon, performed under the assumption of bilateral symmetry of the human body across the sagittal plane (Hargittai & Hargittai, 1994). Based on ISB recommendations for defining coordinate systems (Wu et al., 2005), the eight carpal bones were considered as a single collection of bones).

Each triangulated surface representing right hand skin and individual bone surfaces were described with a geometry g_i.

$$g_i = [(p_{1,1,x} \quad p_{1,1,y} \quad p_{1,1,z}), \quad ... \quad (p_{i,j,x} \quad p_{i,j,y} \quad p_{i,j,z})]$$

(3.1)

Where p represents each point/vertex j on the surface mesh for bone i. Thus, i range from 1 to n (n=23 for the number of surfaces modeled), and j range from 1 to m (m equals the number of vertices/points on each individual 3D). Based on ISB recommendations (Wu et al., 2005), all bone and skin geometries g_i were transformed to share the same global origin at volumetric centroid of the carpal bones by multiplying the translation matrix below with a vector d to each homogeneous vector v.

$$T_d = \begin{bmatrix} 1 & 0 & 0 & d_x \\ 0 & 1 & 0 & d_y \\ 0 & 0 & 1 & d_z \\ 0 & 0 & 0 & 1 \end{bmatrix} \begin{Bmatrix} v_{ijx} \\ v_{ijy} \\ v_{ijz} \\ 1 \end{Bmatrix}$$

(3.2)

3.2.2   Coordinate Systems of the 3D Models

3.2.2.1   Bones Preliminary Local Axes

The preliminary axes of each bone were identified using PCA after determining the eigenstructure of the empirical covariance matrix of each triangulated surface i (Bredbenner et al., 2010; Zhu & Li, 2011). The first three eigenvalues (λ_k) and eigenvectors (PC_k) characterize the vertices along the 3 principal preliminary axes, Y', Z' and X', spanning a shape space centered at the mean (Appendix B).

3.2.2.2   Coordinate Systems for Radius and Ulna

Based on ISB definitions, the origin of was established between radioscaphoid fossa and radiolunate fossa (Wu et al., 2005) but at the distal end for hand modeling purposes. $\vec{Y}$ axis is directed along the long axis based on the direction of the radius shaft (Wu et al., 2005). $\vec{Z}$ is directed towards the styloid process perpendicular to $\vec{Y}$, and $\vec{X}$ is directed volarly (Wu et al., 2005) determined by the cross product of $\vec{Y}$ and $\vec{Z}$.

The Y-axis of radius and ulna was identify by isolating the portion of the bone that corresponds to the shaft and the center of this section along Y' (red line- Figure 3.2). Then, the center of this section along Y' was identified and a total of 21 perpendicular cross-sections were determined in increments of 5% along $\vec{Y}'$ towards the positive direction (10 cross-sections) and negative direction (10 cross-sections) from the center

section of the shaft (1 cross-section in red) (Figure 3.2). The centroids of each cross-sections were identified and a least square line was fitted to these centroids. This fitted line was identified as the local Y-axis for the radius $\vec{Y}_r$ and ulna $\vec{Y}_U$. The local origin of radius and ulna were determined by isolating the distal end of the bone (top 25% along $\vec{Y}$) and by identifying the last vertex along $\vec{Y}$. Based on ISB recommendations, the styloid process of the radius and ulna was used to determine their local Z-axis (Wu et al., 2005), identified programatically as the maximum vertex in the 3-D mesh along the **Y**-axis. The perpendicular vector between $\vec{Y}$ and the styloid process corresponded to the **Z**-axis. The **X**-axis was determined by the cross product of **Y** and **Z** –axes.
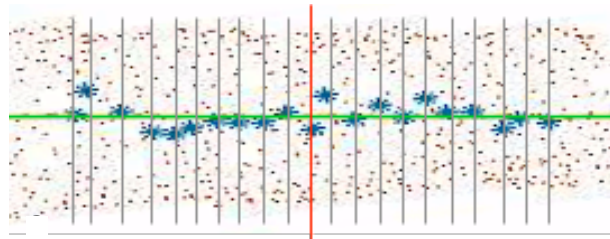
Figure 3.2 The shaft section was isolated using the preliminary Y-axis (Y' in green) and the local Y-axis for the radius/ulna was identified based on a least square line was fitted to the centroids of the 21perpendicular cross-sections determined at every 5% from the center of the shaft.

3.2.2.3 Coordinate Systems for Phalanges and Metacarpals of the Hand

Y-axes for all phalanges were obtained using the same method as described above. The positive *Y*-axis Y_i of each phalange is directed distally. The origin of each finger segment was established at the proximal end, specifically at the lowest point along the Y-axis as described by Miyata et al. (2007). The origin of each finger segment was determined by isolating the proximal end, corresponding to 25% of the bone along Y_i of each geometry matrix g_i. Local Z-axes (Z_i) were determined by adjusting the preliminary Z-axis (Z_i') so that is perpendicular to Y-axis, directed ulnarly. The preliminary Z-axis

$(Z_i{}')$ of each segment i was projected on the plane that is perpendicular to the segment's local Y-axis (Y_i). Thus, i ranged from 1 to n (n=13 for the number of bone segments modeled). The X-axes of each finger segment were directed volarly determined by the cross product of Y_i and Z_i – axes.

3.2.2.4   Global Coordinate System

The positive Y-axis Y_{global} is directed distally, the Z-axis Z_{global} directed to the right ulnarly, and the positive X- axis X_{global} directed volarly from the outer product of the Y and Z –axes. Similar with previous studies (Zhou, 2013; Miyata et al., 2007; Wu et al., 2005; Valero-Cuevas et al., 2003; Kobayashi et al., 1997), the carpal bone angular deviations and wrist motion were defined based on the wrist neutral position in neutral flexion/extension and neutral radial/ulnar deviation in respect to the radius. Therefore, following Wu et al. (2015) definitions, the orientation of global coordinate system at the carpal bones was defined parallel with the radius coordinate system with the wrist in neutral position. Y_{global} was defined parallel to Y_r, similarly for X_{global} and Z_{global}.

Figure 3.3 summarizes the process for developing models and the corresponding coordinate systems for hand, wrist and upper forearm bones and skin.

Hand CT
(1 DICOM file)

Amira (v. 5.3.3, FEI Visage Imaging, Inc.)

Manual segmentation
30 .ply files: 3D surface segments
19 phalanges   8 carpals
1 skin   2 upper arm bones

Downsample faces of 3D-Segments

Quadric Edge Collapse Decimation using MeshLab (v. 1.3.2, sourceforge.net)

Right hand?

Yes   No

Reflect hand

Translate global origin to centroid of carpals

Individual 3D-mesh of bone segment in .ply format

Establish bones preliminary directions of local axes with Principal Component Analysis

$\overrightarrow{Y_{Bt}}$

...ections of 3D
... but not precise due to surface/ curvature irregularities (e.g. distal ends)

• Isolate shaft and determine cross-sections every 5% along Δ **Y'**
• Determine final **Y** based on centroids of cross-sections

$\overrightarrow{Y_{Bt}}$

ISB Recommendations: Determine Y-axis based on shaft's direction

Radius/ Ulna?

Yes   No

Isolate distal end of Radius/Ulna (**max** 25% of bone along **Y**)

$\overrightarrow{Y_r}$

Isolate proximal end on phalanx (**min** 25% of bone along **Y**)

Local origin: at distal end at Max vertex along **Y**

Local origin: at proximal end at Min vertex along **Y**

Local **Z**: determined with Styloid Process

$\overrightarrow{Y_r}$

Local **Z**: **PC2**

Max point in mesh along Y Per ISB Recommendations

Local X-axis: cross-product of **Y** and **Z**

Per ISB Recommendations

Local X-axis: cross-product of **Y** and **Z**

Per ISB Recommendations

Carpals 3D-Mesh in .ply format

Carpals/Skin/Global axes based on Radius

Skin 3D-Mesh in .ply format

Per ISB Recommendations

Figure 3.3 Flowchart of method to develop models of the bones and skin surfaces for the hand, wrist and forearm and the corresponding coordinates systems

47

Figure 3.4 shows the 3D models developed in this study for realistically describing surfaces of skin, carpals, fore arm bones and phalanges. The axes directions were assigned automatically to each bone surface. The global coordinate system, located at the centroid of the carpals, corresponds to the coordinate system used for the skin surface.
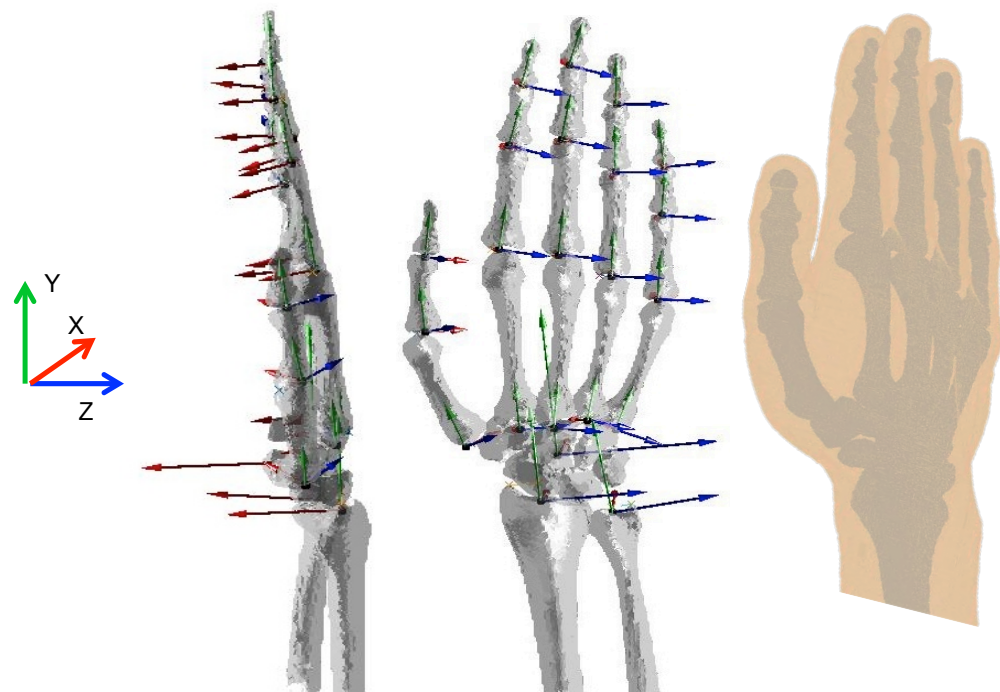
Global Coordinate System		Local Coordinate System for All Bones	
Origin ($O_{CAR/global}$)	Volumetric center of carpals	Origin ($O_{MC}, O_{PP}, O_{MP}, O_{DP}$)	In transverse plane: along the centerline of tubular shaft. In coronal plane: the most proximal point of the bone's base.
X axis (X_{CAR}, X_r)	Pointing volarly	X axis ($X_u, X_{MC}, X_{PP}, X_{MP}, X_{DP}$)	Pointing volarly
Y axis (Y_{CAR}, Y_r)	Pointing distally	Y axis ($Y_u, Y_{MC}, Y_{PP}, Y_{MP}, Y_{DP}$)	Pointing distally
Z axis (Z_{CAR}, Z_r)	Pointing ulnarly	Z axis ($Z_u, Z_{MC}, Z_{PP}, Z_{MP}, Z_{DP}$)	Pointing ulnarly

Figure 3.4 Lateral view (left) and dorsal view (middle) of the 3D models representing the surfaces of the hand and forearm bones with the local and global coordinate systems. The green arrow represents Y-axis, red represents X-axis, and blue represents Z-axis. The longer arrows are the hand's global axes. To the right, the 3D model of the skin on the template's posture, aligned by the global coordinate system.

3.2.3   Evaluate segmentation process

Procrustes alignment, proposed by Gower (1975), and the Iterative Closest Point (ICP) algorithm (Appendix C) were used to superimpose and align shapes and to calculate shape differences based on distance metrics (Appendix C), yielding an automated, landmark-free shape analysis to ensure an accurate point-wise homology.

Mean Euclidean distance were determined 1) among analysts for evaluating manual segmentation process, and 2) among postures segmented by the same analyst for evaluating the shape consistency of bone models. The metacarpal and three phalanges of index finger, from Posture 0, were used to evaluate the manual segmentation process. These were segmented six times by six different analysts with prior segmentation software experience but without experience in Amira software, all following the same protocol for manual segmentation developed for this study by Analyst 1. The bone surfaces segmented by Analyst 1 (first author of this study) were individually compared with the surfaces segmented by the other analysts (student research assistants). The consistency between postures was measured by comparing the shape differences of all metacarpals and phalanges between Postures 0-4, all segmented by the same Analyst. Posture 0 (hand pressed against a flat surface) was designated as the template surface, and was compared to the rest of the postures (all segmented by Analyst 1. Each metacarpal and phalanx from Posture 0 was compared with its corresponding 3D mesh in the other 4 postures (Postures 1-4 –Figure 3.1). This repeatability analysis was possible because all CT Scans were acquired from the same hand.

Localized shape differences were assessed by evaluating the locations of surface points between postures (all segmented by Analyst 1), located along 12 cross-sections, equally distributed along the Y-axis (Figure 3.5).
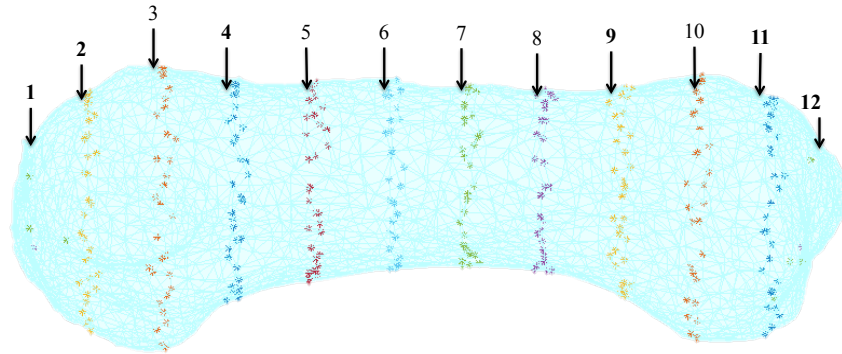
Figure 3.5 Twelve cross-sections along the Y-axis of MC, PP, MP and DP segments were determined to show localized differences in average Euclidean distances between postures.

3.2.4 Evaluate Difference between Coordinate Systems

The translation error (Appendix D) defined as the difference between centroids in three directions in space, and rotation error defined as the same axis rotation difference (Appendix D), between Template and each posture (4 comparisons) were used to evaluate the corrdinate system of each metacarpal and phalanx segmented by the Analyst 1 (Kamojima et al., 2004). The rotation error was also used to determine the difference between the preliminary Y-axis *Y'* and the local Y-axis *Y* per type of finger segment.

3.2.5 Joint Distances

The distance between each two proximate segments was calculated to determine the average joint distances. These were used to evaluate the minimum distance required to rotate two adjacent segments without overlapping the adjacent surfaces. To do so, the proximal and distal ends of two articulating bones were isolated. Then, maxima and minima of the y-axes proximal and distal ends respectively, were determined. The linear

50

distance between these points corresponded to he joint distance.

3.3 Results

3.3.1 Segmentation Process- Between Analysts

The mean Euclidean distance and the Procrustes error were examined for phalanges of the index finger between Analyst 1 and the rest of the Analysts (Table 3.1). Overall, the mean Euclidean distance was 0.199 ± 0.062 mm and the average Procrustes error was 0.0043 ± 0.0017 mm.

Table 3.1 Mean Euclidean distances and Procrustes error per bone segment, for shape comparison between Analyst 1 and other Analysts (2-6). (Mean ± std. dev.)

Posture	Bone segment	Mean Euclidean distance (mm)	Procrustes error (mm)
Analyst 2	MC2	0.191 ± 0.019	0.005 ± 0.0001
	PP2	0.145 ± 0.022	0.003 ± 0.0002
	MP2	0.164 ± 0.015	0.004 ± 0.0005
	DP2	0.241 ± 0.036	0.003 ± 0.0006
Analyst 3	MC2	0.301 ± 0.006	0.006 ± 0.0001
	PP2	0.109 ± 0.030	0.005 ± 0.0003
	MP2	0.166 ± 0.018	0.006 ± 0.0005
	DP2	0.213 ± 0.018	0.004 ± 0.0005
Analyst 4	MC2	0.270 ± 0.096	0.005 ± 0.0005
	PP2	0.266 ± 0.038	0.005 ± 0.0003
	MP2	0.255 ± 0.027	0.004 ± 0.0007
	DP2	0.110 ± 0.042	0.002 ± 0.0005
Analyst 5	MC2	0.122 ± 0.224	0.002 ± 0.0002
	PP2	0.133 ± 0.045	0.001 ± 0.0003
	MP2	0.215 ± 0.038	0.005 ± 0.0017
	DP2	0.283 ± 0.019	0.005 ± 0.0010
Analyst 6	MC2	0.136 ± 0.224	0.002 ± 0.0002
	PP2	0.274 ± 0.045	0.007 ± 0.0003
	MP2	0.184 ± 0.038	0.006 ± 0.0017
	DP2	0.209 ± 0.019	0.004 ± 0.0010

3.3.2 Segmentation Process- Between Postures

The mean Euclidean distance and the Procrustes error were examined for each bone segment between template posture and each target posture, all segmented by the

51

same Analyst. The Mean Euclidean distance were 0.48± 0.09 mm for the metacarpals (MC), 0.47± 0.03 mm for the proximal phalanges (PP), 0.46± 0.02 mm for the middle phalanges (MP), and 0.48± 0.03 mm for distal phalanges (DP). Overall, the Procrustes error ranged from 0.001 mm to 0.009 mm (Table 3.2).

Table 3.2 Euclidean distances and Procrustes error per bone segment, for shape comparison between template and other postures (1-4). (Mean ± std. dev.)

Posture	Bone segment	Mean Euclidean distance (mm)			Procrustes error (mm)		
Posture 1	MC	0.414	±	0.019	0.001	±	0.0001
	PP	0.447	±	0.022	0.002	±	0.0002
	MP	0.478	±	0.015	0.005	±	0.0005
	DP	0.470	±	0.036	0.008	±	0.0006
Posture 2	MC	0.419	±	0.006	0.001	±	0.0001
	PP	0.475	±	0.030	0.002	±	0.0003
	MP	0.438	±	0.018	0.005	±	0.0005
	DP	0.477	±	0.018	0.008	±	0.0005
Posture 3	MC	0.475	±	0.096	0.001	±	0.0005
	PP	0.481	±	0.038	0.002	±	0.0003
	MP	0.467	±	0.027	0.005	±	0.0007
	DP	0.495	±	0.042	0.008	±	0.0005
Posture 4	MC	0.593	±	0.224	0.001	±	0.0002
	PP	0.493	±	0.045	0.002	±	0.0003
	MP	0.472	±	0.038	0.006	±	0.0017
	DP	0.494	±	0.019	0.008	±	0.0010

Between all postures, major differences in mean Euclidean distances were localized along the distal/proximal ends, and the necks of the phalanges (Table 3.3).

Table 3.3 Mean Euclidean distances of surface points located on each cross-section (Figure 3.5) between five postures (pooled for all bone surfaces).

Cross-Section	Euclidean Distance
1	0.52 ±0.21
2	0.42 ±0.14
3	0.22 ±0.11
4	0.61 ±0.34
5	0.23 ±0.09
6	0.12 ±0.04
7	0.07 ±0.02
8	0.11 ±0.08
9	0.47 ±0.21
10	0.24 ±0.12
11	0.40 ±0.16
12	0.48 ±0.18

3.3.3 Coordinates Systems

To evaluate the coordinate systems, the translation and rotation of the axes were compared for each finger bone segment between template posture and each target posture. Table 3.4 shows a summary of the average resultant translation and rotation errors per type of bone. Overall, the translation error ranged from 0.076 to 0.613 (mm), and the average rotation error ranged from 1.962 to 12.851 (deg.).

Table 3.4 Average difference of resultant translation (Δ) of centroids and average rotation error between template and the rest of the postures per type of finger segment. All segmented by the same analyst. (Mean ± Std. dev.)

Posture	Bone segment	Difference in translation (mm)	Rotation error (deg.)
Posture 1	MC	0.236 ± 0.085	5.095 ± 2.563
	PP	0.281 ± 0.147	6.713 ± 3.424
	MP	0.259 ± 0.077	8.212 ± 3.582
	DP	0.371 ± 0.132	8.544 ± 1.827
Posture 2	MC	0.267 ± 0.089	4.473 ± 1.767
	PP	0.393 ± 0.177	5.970 ± 3.197
	MP	0.177 ± 0.102	7.689 ± 2.403
	DP	0.369 ± 0.168	7.191 ± 2.956
Posture 3	MC	0.254 ± 0.113	8.531 ± 3.221
	PP	0.372 ± 0.161	6.240 ± 2.269
	MP	0.216 ± 0.033	5.202 ± 1.653
	DP	0.361 ± 0.067	7.607 ± 2.179
Posture 4	MC	0.321 ± 0.173	10.900 ± 3.462
	PP	0.327 ± 0.195	6.263 ± 2.116
	MP	0.318 ± 0.039	7.488 ± 3.357
	DP	0.467 ± 0.093	6.771 ± 1.555

3.3.4 Preliminary vs. Final Y axes

Mean rotation differences of the angle between Y' and Y, for each type of finger and metacarpal segment are shown in Table 3.5. The preliminary and final axes differed most for the longer bone segments and the standard deviations follow the same pattern.

Table 3.5 Mean rotation error (deg.) between Y' and Y, per type of bone, pooled for all postures. (Mean ± std. dev.)

Bone Segment	Rotation Error: Angle Between Y' vs. Y (deg.)
MC	28.53 ± 17.12
PP	10.34 ± 04.45
MP	07.97 ± 03.67
DP	05.86 ± 03.16

3.3.5 *Joint Distances*

Table 3.6 shows the average distances for joints in the hand. On average among all postures, joint distances for the articulating finger joints were found to be 1.02 ± 0.34 mm (Figure 3.6).
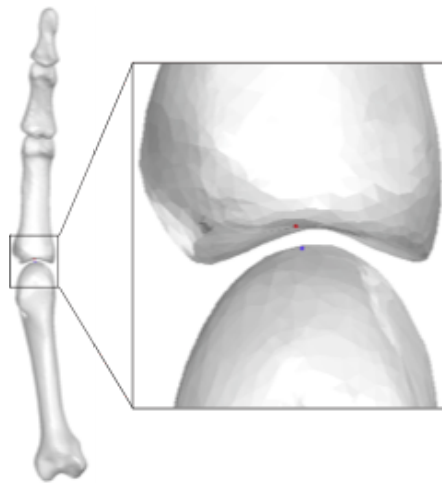
Figure 3.6 MCP2 joint distance, defined with the linear distance between the max vertex along Y in MC2 (blue) and the min vertex along Y in PP2 (red).

Table 3.6 Mean distances for joints in the hand, pooled for all postures (mm) (Mean ± std. dev.)

Joint	Joint Distance (mm)
CMC	1.51 ± 0.42
MCP	1.02 ± 0.23
PIP	0.71 ± 0.14
DIP	0.84 ± 0.08

3.4   Discussion

The CT image manual segmentation method for obtaining hand surfaces was performed with low variability between the six Analysts, with respect to the size of the

bones (Table 3.1). The overall shape difference between Analysts was less than 0.2 (mm), defined with the mean Euclidean distance based on the sum of all distances between corresponding vertices. This is considerably less than the resolution of the image dataset that ranged from 0.3 mm to 0.67 mm. This shape difference between Analysts the same as of those reported by DeVries et al., (2008) which are 0.19 (mm), 0.20 (mm), and 0.21 (mm) for the proximal, middle, and distal phalanx, respectively (DeVries et al., 2008).

Results also show that manual segmentation of high-contrast CT datasets accurately represents true surface geometry of bones; tested by comparing shape differences of bone surfaces from five hand-CT images of the same subject, all segmented by the same Analyst (Table 3.2). Several studies have reported on the accuracy (reproducibility) of shape difference based on segmentation of medical images (Klein et al., 2015; DeVries et al., 2008). In this study the results on shape difference correspond only 5% of those reported by Klein et al. (2015) for the femur, and approximately twice as of those reported by DeVries et al., (2008) (Table 3.2). Major differences in mean Euclidean distances were localized along the distal/proximal ends, and in the necks of the bone surfaces (Figure 3.5, Table 3.3). DeVries et al., 2008 evaluated manually segmenting CT Scans by comparing the shape differences of the resulting surfaces with laser surface scans of the same cadaver bones. The manual segmentation was performed on the coronal reformatted CT images (DeVries et al., 2008). DeVries et al. (2008) concluded that the surfaces created from CT datasets accurately represent the true surface geometry of bones based on their comparison with the surfaces from the laser scans which they considered as the true values. In this study,

the shape comparisons were made between CT Scans, and not only the coronal view was used segmenting the surfaces but also the sagittal and dorsal views. In DeVries et al. (2008), the number of vertices defining each surface differed. They determined the Euclidean distances using the percentage of points with a distance less than the resolution of the original image dataset (0.34 mm) (DeVries et al., 2008). In this study, the surfaces compared were homologous, and a pairwise comparison was made using all vertices in the surfaces to obtain the true values for the Euclidean distance. These differences between methods could explain the discrepancies between the shape differences obtained in this study versus DeVries et al. (2008). The 3D models developed in this study were accurate representations of hand bone surfaces. The Mean Euclidean distances, 0.48± 0.09 mm, 0.47± 0.03 mm, 0.46± 0.02 mm, and 0.48± 0.03 mm for MC, PP, MP and DP bones, respectively (Table 3.2). These results are considered minimal based on comparisons from literature and based on the range of the resolution of the original CT images (0.3 mm to 0.67 mm).

Coordinate system differences (translation and rotation) obtained in this study were within the same range to the results reported by Kamojima & Miyata (2004), corresponding to average translation and rotation raging from 0.001-1.013 (mm) and 1.927-16.085 (deg.), respectively (Table 3.4). Kamojima & Miyata used these metrics to compare manual segmentation to their proposed method: identifying the configuration of hand bones from MR images of multiple postures by registration of bone models for the same subject. They concluded that shape differences were minimal. In this study, the translation and rotation differences corresponded to 0.076 to 0.613 (mm), and an average rotation error that ranged from 1.962 to 12.851 (deg.). However, Kamojima & Miyata

obtained the 3D surfaces from MR images, which does not depict accurate bone sizes (McKinnis, 2010). The translation differences would not affect the model since the results are within the resolution of the original CT images (0.3 mm to 0.67 mm). The rotation differences may affect the model when used to determine kinematics involving a change in angle less than the rotation error obtained for that axis.

Results from this study show that 3D models can be develop to represent bone surfaces more realistically for construction and animation of anatomically based hand models. The results from the methods developed in this study to establish a local coordinate system for each bone are reliable when compared with comparable values in literature such as the ones reported by Kamojima & Miyata (Tables 3.1 and 3.2). Although the coordinate systems developed in this study can be applied to any hand, regardless of image modality or hand size, it is recommended to segment CT Scans when modeling bone surface geometries because CT Scans provide optimum resolution and contrast for segmenting b this type of segmentation (McKinnis, 2010).

3.4.1   Application

The proposed methods provide a basis for conducting spatial analysis of the hand using medical images, and specific data gathered in this study can be used to enhance the accuracy of current hand models in determining hand shape. The models of the 3D-bone and skin surfaces developed in this study can be used for in simulation models such as Choi (2008) (Figure 3.7). Current spatial analyses can be improved with the models developed in this study so that tendon locations can be accurately identified based on the bone geometry, and the skin surfaces can be used to determine the space requirements

57

needed for the hand. Kinematics can be improved by determining the CoR locations based on the realistic anatomical bone surfaces created in this study. This would lead into precise calculation of tendon moment arms based on the locations of the joint centers, and into realistic movements without overlapping adjacent bones during rotation.
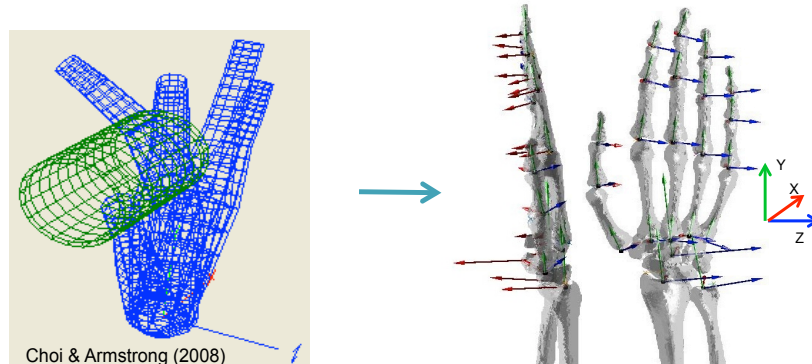
Figure 3.7 Current hand models based on simple representations such as Choi, 2008 can be enhanced by accurately representing the hand segments based on bone and skin geometries obtained through CT Scans.

3.4.2 Limitations

Symmetric superimposition in methods such as ICP is very dependent on the initial positions of the surfaces relative to one another (Shi et al., 2014). Although an automated process was used for alignment and superimposing, the last step was to inspect visually the aligned surfaces. This was done with the purpose of further evaluate the alignment process to ensure there was no reflection along exes (e.g. aligning distal end of template with proximal end of targeter posture). This step could be eliminated by automatically assigning pseudo-landmarks (Shi et al., 2014), using Wu et al. (2005) recommendations as a baseline, after simplyfying the 3D segments to avoid axes reflection when using ICP for symmetric superimposition.

3.5   Conclusion

This study shows that realistic models of hand, wrist and upper arm bones and skin surfaces can be develop from a dataset of CT Scans of one hand in five different postures. By leveraging existing ISB recommendations on definitions of joint coordinate systems (Wu et al., 2005), and combining them with mathematical and statistical methods, such as PCA, to identify bone landmarks, the authors successfully develop protocols for determining coordinate systems for these meshes. The average joint distance results can be used to establish minimum distances between adjacent bones. This would be useful when modeling rotation between adjacent bones with a pin joint center of rotation, ensuring no overlap between bone surfaces.

3.5.1   *Acknowledgements*

CHAPTER 4 Development of Procedures for Adapting Four Methods to Determine Centers of Rotation of Phalanges Based on Joint Geometry Obtained through CT-Scans for Hand Modeling

Abstract

This work is concerned with the development of methods to establish Centers of Rotations (CoR) of a kinematic model for predicting hand posture for better design of product, garments and manual work tasks. Anatomical parameters of the hand bones were obtained by medical imaging to determine instantaneous centers of rotation for each finger joint. Posture data were captured based on a single hand in five different postures. Four methods to determine CoR were implemented to each finger joints. These methods were 1) Sphere Fitting, 2) Ellipsoid Fitting with a fixed CoR, and 3) 3D-Reuleaux, and 3) Axes of Rotation (AoR) through Iterative Closest Point Algorithm (ICP) with instantaneous CoRs. The latter, takes into account where the CoR is located at each position of a joint, based on the contour of the anatomical surface. Several studies have validated their methods using sphere fitting as a gold standard. However, this study intended to deviate from that gold standard (sphere fitting) to achieve more accurate and realistic CoR locations by taking into account the rotation and translation caused by the anatomy of the joint that is not considered during sphere fitting method. Results from this study show that there was a significant difference between fixed and instantaneous CoRs but not within methods. Based on the results the methods were raked as ICP (1), 3D-

Reuleaux (2), Ellipsoid Fitting, (3) and Sphere Fitting (4) (1 being most accurate based on anatomical joint). Additionally, it was found that instantaneous centers were not suitable for angles between the two adjacent distal segments that are 1.3 degrees for the CMC joints, 5.43 for the MCP joints and 2.31 degrees for the DIP joints, or smaller.

4.1.   Introduction

Predictions of hand posture and motion are needed for better understanding of articular pathologies, safe manual work, and to manipulate hand-held tools, and for reducing overexertions. To most effectively describe hand motion, accurate estimations of joint centers of rotation (CoR) are needed (Panjabi, 1979). CoRs can be defined as *fixed* with constant link lengths or *instantaneous* with variable link lengths, where the CoR location moves based on the combined rolling (rotation) and gliding (translation) between two adjacent surfaces (Figure 4.1).
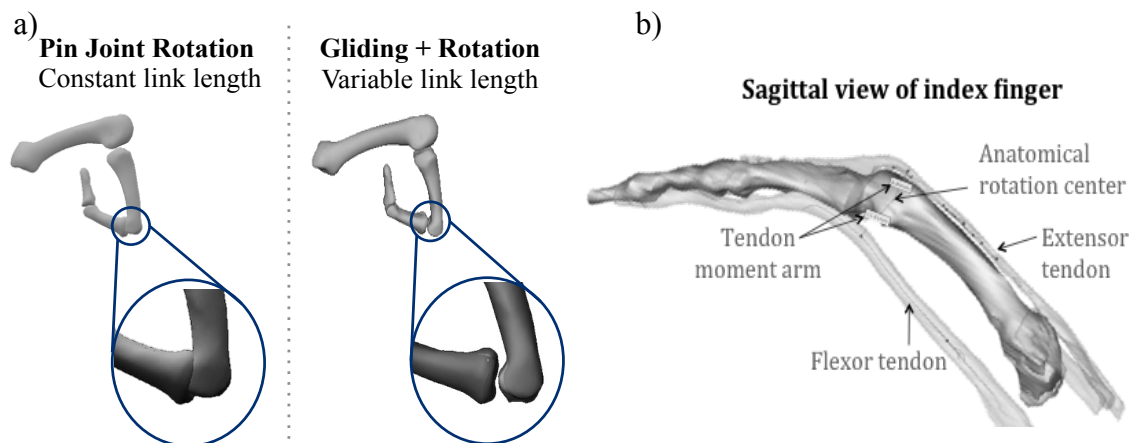
Figure 4.1 a) Fixed CoR involves pin joint rotation with constant link lengths. The instantaneous CoRs has variable link lengths, where the CoR location moves based on the combined rolling (rotation) and gliding (translation) between two adjacent surfaces. Fixed CoR can lead into overlap of the anatomical segments depending on the joint angle. b) Illustration of bone structure of the index finger and their relationship with tendon loads based on joint locations and changes in moment arms.

Kinematic models can be improved by predicting postures based instantaneous CoRs, based on bone structural geometry. This could lead to a better understanding in the relationship between external force, hand posture and tendon loads. Bone structural geometries of adjacent segments and joint center locations affect finger joint angles, locations of tendon attachments (tendon moment arms), tendon movements and forces, and geometric locations of the extrinsic and intrinsic tendons (Fowler et al., 2001) (Figure 4.1). Thus, these models can be used to estimate tendon excursions so that risks of upper extremity musculoskeletal disorders can be prevented (Schweizer et al, 2003; Armstrong et al., 1987). To date, several methods have been developed to estimate fixed and instantaneous CoRs for human joints (Woltring et al., 1985; Bell et al., 1989; Marin et al., 2003; Ehrig et al., 2006; Bey et al., 2006; Monnet et al., 2007; Lopomo et al., 2010; Nikooyan et al., 2011). However, not many of these approaches have been tested for hand kinematics.

4.1.1. CoR Estimation

Most studies have used vision-based (Rehg, 1994; Kuch, 1995), glove-based (Sturman, 1994), and Three dimensional (3D) marker position methods (Jan et al., 1997) to predict hand kinematics for posture data. These methods are limited by 1) skin deformation, 2) marker occlusion (for vision-based and 3D marker methods), and 3) loss of motion naturalness (for-glove based method).

Others have considered using underlying skeletal critical dimensions (Kurihara & Miyata, 2004; Lien, 2005) to predict hand joint motion. These methods include Radiography (Bell et al., 1989), Helical Axis (HA), (Woltring et al., 1985), Minimal

Amplitude Point (MAP) (Marin et al., 2003), SCoRE (Ehrig et al., 2006), Sphere Fitting (Pratt, 1981; Ehrig et al., 2006), Reuleaux (Reuleaux, 1875; Panjabi, 1979), and ICP (Besl & McKay 1992; Figueroa et al., 2016). Radiography involves manual selection of landmarks (Bell et al., 1989), a tedious, and error prone process (Mutsvangwa et al., 2015). In addition, as this is a two-dimensional analysis, combinations of x-rays must be available to predict hand postures. HA assumes fixed CoRs, requires long calculation times and has larger error at small rotation angles (Monnet et al., 2007). MAP also assumes fixed CoR and has being identified to be less effective than several other methods (Ehrig et al., 2006). SCoRE estimates instantaneous CoRs for each segment (Ehrig et al., 2006), but although better than MAP and HA, the error produced at small rotation angles is still significant.

Sphere Fitting it is most commonly used (Marin et al., 2003; Halverson et al., 1999; Cerveri et al., 2005; Ehrig et al., 2006; Chang & Pollard, 2007) among currently available methods for estimating CoRs. This method identifies a pair of matrices to best fit a sphere around a set of data points, such that the center and radius of the sphere are optimized (Pratt, 1987; Eberly, 1999). It is hypothesized that fitting an ellipsoid to the head of the hand bones would be more effective than a sphere (Turner et al., 1999; Li & Griffiths, 2004). Ellipsoid Fitting has been applied to estimate the three-dimensional geometry of bone segments but it has never been fitted specifically to human joints. This study adapted Pratt's (1987) and Eberly's (1999) Sphere- and Ellipsoid- Fitting techniques to hand joints. Spheres/ellipsoids were fitted on each proximal bone's head to obtain CoRs for each distal bone. Both of these methods assume a fixed CoRs, not taking into account the geometry of the anatomical joints.

Reuleaux (Reuleaux, 1875) is a classic technique that has been used for hand kinematics involving radiographs (Panjabi, 1979; Buchholz et al., 1992) to identify instantaneous CoR. But as a two-dimensional analysis is limited in its accuracy and effectiveness (Buchholz et al., 1992). Eberharter & Ravani (2006) developed a computational geometric method for the 3D kinematic registration using the classical two-dimensional Reuleaux method (Reuleaux, 1875). In this study, a 3D version of Reuleaux, proposed by Eberharter & Ravani (2006), was applied to hand joint for the first time.

ICP has been used in previous studies for hand modeling (Miyata et al., 2007). However, Miyata et al. (2007) used magnetic resonance imaging (MRI), segmenting cancellous bone (instead of cortical bone surface) and determining their corresponding bounding boxes to define geometry and coordinate systems for each segment. The International Society of Biomechanics (ISB) recommends using specific bone landmarks and true geometry to determine coordinate systems and axis of rotation (AoR) (Wu et al., 2005). CT Scans require shorter measurement times than MRIs (McKinnis, 2010), and provide the best quality for accurate bone surface (Kurihara & Miyata, 2004). This study expands on previous adaptation of ICP for hand modeling (Miyata et al., 2004), using CT Scans as the source for hand data.

This study aims to further develop four methods for estimating hand joint CoRs, to be applied to hand joints based on the 3D models of finger segments developed in Chapter 3. These methods are 1) Sphere fitting, 2) Ellipsoid fitting, 3) 3D-Reuleaux, and 4) Iterative Closest Point (ICP) algorithm. These CoR methods were compared based on

their accuracy and precision (Lempereur et al., 2010). Additionally, potential advantages, disadvantages and important parameters (e.g. joint angle, anatomical geometry) were identified. It is hypothesized that locations of fixed CoRs are different from instantaneous CoRs. Additionally, it is expected that methods using instantaneous CoRs will result in the best range of accuracy.

4.2.   Methods

3D models of finger segments, and their corresponding coordinate systems, developed in Chapter 3 were used for this study. In Chapter 3, CT images were segmented to create 3D models representing segments of a male's left hand in five different postures: neutral, pushing against a flat surface, lateral pinch, power grip, and pinch grip. These postures were used to adapt to hand joints four methods to estimate CoR locations between adjacent bone segments.

1. Sphere Fitting- CoR rotation

2. Ellipsoid Fitting- CoR rotation

3. 3D-Reuleaux- CoR rotation and translation

4.   Iterative Closest Point Algorithm (ICP)- CoR rotation and translation

4.2.1. Sphere and Ellipsoid Fitting

In this study a general Sphere Fitting method in 3D explained by Eberly (1999) and Pratt (1987) and the Ellipsoid Fitting method for 3D surfaces explained by Eberly (1999, 2011) were applied to finger joints for hand modeling considerations. Spheres and ellipsoid were fitted to the vertices corresponding to the distal end each proximal bone (Figure 4.2) to identify the CoR of the adjacent distal segment.
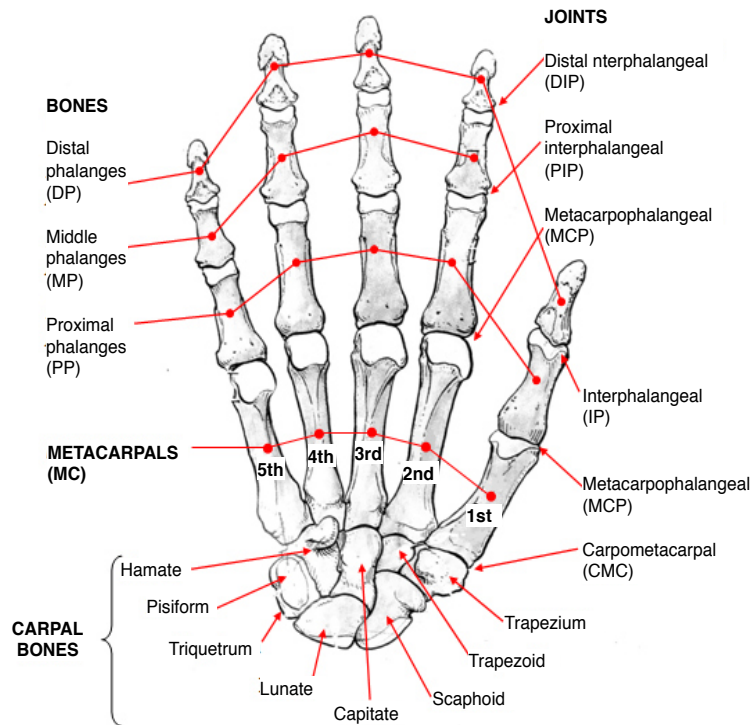
Figure 4.2 Bones and joints of the hand with the corresponding acronyms. The fingers are numbered starting from the thumb (finger 1) to little finger (finger 5)

The top 25% of the total length of each phalanx, defined with the local Y-axis, was

used to represents the surface of the distal end (Figure 4.3).
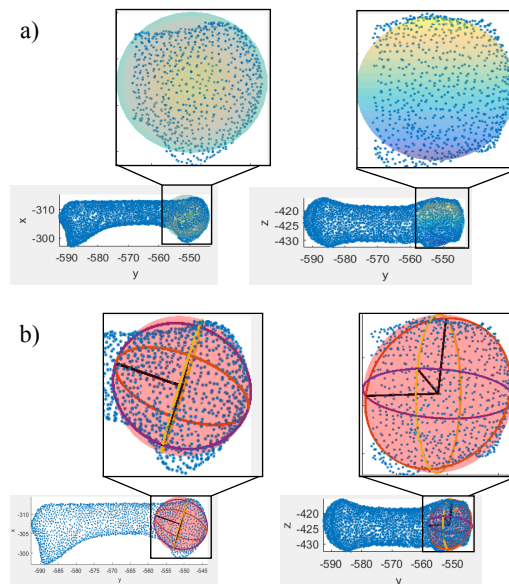
Figure 4.3 a) Sphere and b) Ellipsoid fitted to the head of an MC1 bone in the X-Y (left) and Z-Y (right) planes. The center of the sphere/ellipsoids corresponds to the fixed CoR of PP1.

For CMC joints, the carpal bone corresponding to each MC bone was used. Spheres/Ellipsoids were fitted to the trapezium, capitate, and hamate to obtain the CoRs for CMC1, CMC3, and CMC5, respectively. Based on the degrees of freedom for the CMC joints reported by El-shennawy et al. and for the sake of simplicity, a connection of the neighbor CMC CoRs and the Y-axis of MC2 and MC4 were used to determine the CoRs for CMC2 and CMC4 joints, respectively (El-shennawy et al., 2001).

3D- Reuleaux

This study adapted the 3D-Reuleaux method discussed by Eberharter & Ravani, (2006) to determine the instantaneous CoRs for anatomical hand joints between two postures. Instead of selecting representative points on each bone segment, all vertices were considered. The 3D models of the finger segments of the template posture from Chapter 3 were fitted to represent the 3D bone structures of the rest of the postures. All bone surfaces were individually morphed using Radial Basis Function (RBF) based on thin plate splines ($\phi(r) = r^2 \ln(r)$), described by Bennink et al. (2006) to ensure homology between meshes.

To obtain the instantaneous CoR of a distal bone based on 3D-Reuleaux, all proximal bones from each fitted posture were aligned to the template (Figure 4.4a). The instantaneous CoR was determined between every two consecutive postures based on the flexion angle (Figure 4.4b).
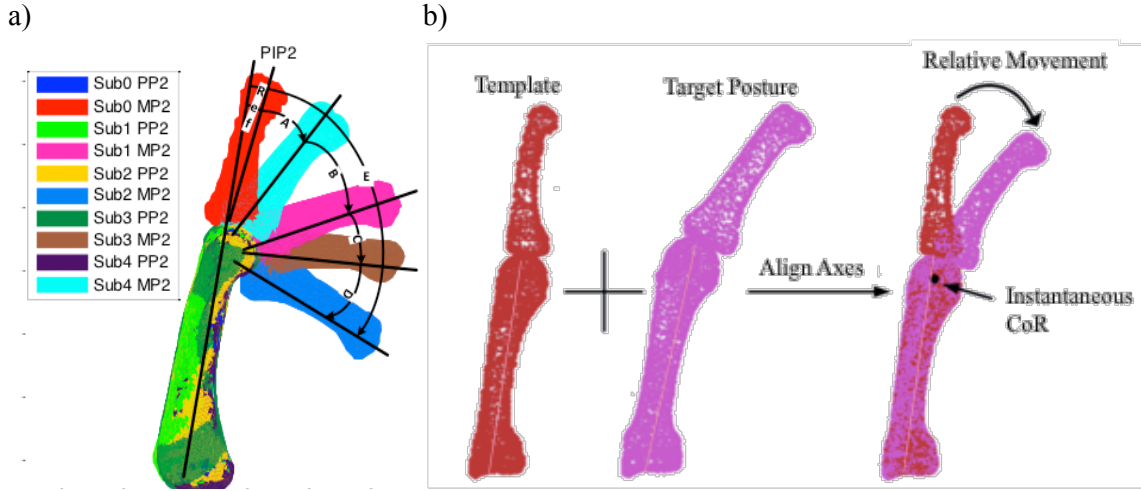
Figure 4.4 a) Proximal segments from all postures were aligned to identify the relative moment of the distal segments. The two adjacent distal segments between postures were identified based on the flexion angle. The reference angle was based between the first PP2 segment and the angle of the Y-axis of the PP2 segment. b) After aligning the proximal segments, the instantaneous CoR was identified between each two adjacent segments using 3D-Reuleaux

The 3D- Reuleaux method proposed by Eberharter & Ravani, (2006), was used to determine the AoR of a distal segment between every two consecutive postures. Given a set of m vertices pairs $\{P_j, P'_j\}$ between two postures and a set of m midpoints $\{M_j\}$, the vectors $\{\boldsymbol{G_i} = P'_j - P_j\}$ were computed. Then a plane ε was approximated by using the least square method. This plane ε was expressed in its explicit form

$$a + \vec{G}_{j,x} + \vec{G}_{j,y} = \vec{G}_{j,z}$$

$$\underbrace{\begin{bmatrix} 1 & G_{1,x} & G_{1,y} \\ \vdots & \vdots & \vdots \\ 1 & G_{m,x} & G_{m,y} \end{bmatrix}}_{A} \underbrace{\begin{bmatrix} a \\ b \\ c \end{bmatrix}}_{x} = \underbrace{\begin{bmatrix} G_{1,z} \\ \vdots \\ G_{m,z} \end{bmatrix}}_{B}$$

(1)

Where a, b, and c are constants. To find an approximate solution, a residual vector r was minimized using Euclidean norm (Eberharter & Ravani, 2006).

$$\vec{r} = Ax - B \neq 0 \; for \; all \; x \in \mathbb{R}_3$$

(2)

The minimized vector of $\vec{r}$ is orthogonal to the subspace, $A^T\vec{r} = 0$. Substituting $\vec{r} = Ax - B$ results in the Gaussian normal equation (3).

$$A^T Ax = A^T B$$

(3)

With the plane defined, the data midpoints and vectors were projected onto it to approximate a series of intersection points (I_j) (Eberharter & Ravani, 2006).

$$I = \sum_{j=1}^{m} \frac{I_j}{m}$$

(4)

The instantaneous CoR of a distal bone was defined as the intersection of the bone local Y-axis between the two compared postures and the AoR identified from 3D-Reuleaux.

4.2.2. Iterative Closest Point Algorithm

Procrustes alignment (Gower, 1975) joint with ICP algorithm (Chetverikov, et al., 2005), used by Figueroa et al., (2017), were applied in this study to derive the link from the relative movement of a distal bone after superimposing proximal segments from all postures to their corresponding template bone. Similar to the 3-D Reuleaux method, the instantaneous CoR was determined between every two consecutive postures based on the flexion angle (Figure 4.4b). Translation T and orthogonal rotation R matrices obtained from ICP with Procrustes, after superimposing proximal segments from two postures, were used to determine the AoR from the relative movement between each two

consecutive distal segments. The intersections of the AoR and the Y-axes of the distal segments were be used to identify the instantaneous CoR (Appendix E).

4.2.3. *Statistical Design*

A paired t-test (MINITAB®) was used to find the mean of the differences between the CoR locations, and subsequently the standard error of their mean. The t-statistic is then calculated by dividing the standard error by the mean. The analysis was performed within and between blocks to compare the fixed and instantaneous methods. Sphere Fitting was compared to Ellipsoid Fitting, and 3D-Reuleaux was compared to ICP. Then, Ellipsoid was compared to 3D-Reulueaux and ICP. Significance was set at *p<0.05*.

Outliers due to insufficient angle between the distal segments were taken out for the distances analysis and t-tests, and the angles were recorded. This is necessary in order to achieve results that accurately represent the data. Based on previous studies, these outliers were expected in the instantaneous CoR methods (Woltring et al., 1985; Marin et al., 2003; Ehrig et al., 2006) where a segment's relative movement is considerably small between two postures.

4.2.4. *Criteria to Evaluate Distances between CoRs*

The CoR locations were also compared against the locations of CoR from the ICP ICP method. The distance between methods corresponded to the resultant $CoR_{Resultant} = (CoR_X, CoR_Y, CoR_Z)$.

$$CoR_{Resultant} = \sqrt{CoR_X{}^2 + CoR_Y{}^2 + CoR_Z{}^2}$$

(5)

The difference between a given method and ICP was then found by subtracting the resultant $CoR_{Resultant}$ from ICP's resultant $CoR_{ICP\ Resultant}$.

4.3. Results

Figure 4.4a illustrates a sample joint with the legend for the order in which the angles were recorded, based on flexion angle. For example, for the MP2 segment, the letter A represents the angle between the red and the cyan segments. Table 4.1 includes joint angles between adjacent postures.

Table 4.1 Joint angles (degrees) between every two adjacent postures

Joint	A θx	A θy	A θz	B θx	B θy	B θz	C θx	C θy	C θz	D θx	D θy	D θz	E θx	E θy	E θz	Ref θx	Ref θy	Ref θz
CMC1	5.0	6.7	6.5	12.6	16.3	11.6	31.4	6.4	32.0	11.5	22.8	19.7	42.6	44.8	43.4	45.6	18.8	49.1
CMC2	1.4	2.1	1.9	1.3	2.1	1.7	2.4	2.7	1.7	3.8	4.0	1.6	8.5	8.9	3.0	15.0	6.2	13.9
CMC3	2.2	1.1	2.3	2.8	2.6	2.3	1.2	1.2	1.0	4.6	3.7	2.7	8.3	7.9	4.5	4.8	7.8	8.5
CMC4	4.1	4.4	4.5	27.0	3.2	27.2	31.7	5.4	31.5	1.7	1.4	2.2	9.2	7.5	7.3	29.3	18.8	31.2
CMC5	13.9	14.7	6.2	4.3	5.6	3.7	45.7	5.8	45.9	46.3	4.3	46.4	22.2	24.3	10.1	15.6	26.6	31.0
MCP1	5.2	5.2	1.6	5.2	5.4	2.9	14.3	15.0	9.4	12.1	12.9	9.7	13.8	13.6	16.1	7.9	8.4	3.9
MCP2	18.7	18.6	1.1	23.4	22.2	14.1	27.1	22.4	19.2	10.0	9.4	7.2	68.2	68.2	1.8	5.5	14.9	15.5
MCP3	30.3	30.5	11.6	41.1	41.4	6.0	7.9	3.6	7.8	7.4	7.5	1.4	81.1	80.6	9.1	11.1	3.8	9.1
MCP4	32.1	31.8	18.7	43.6	42.4	12.3	11.3	3.4	10.8	10.9	2.8	10.6	81.2	76.7	27.5	24.6	11.6	23.7
MCP5	24.9	26.3	29.1	53.4	60.3	27.5	91.8	86.7	135	94.9	84.8	166	74.4	71.2	24.2	3.6	17.2	17.6
IP1	16.1	15.9	3.9	21.2	21.0	4.9	3.1	1.8	2.7	23.7	23.2	7.0	61.0	61.6	8.2	35.4	32.4	19.5
PIP2	25.2	25.3	4.5	34.4	33.9	8.8	20.3	20.6	6.3	28.0	28.1	6.2	107	106.6	23.3	6.6	7.5	9.7
PIP3	10.5	10.4	2.1	57.3	57.2	6.0	11.9	11.9	0.5	24.4	24.3	5.7	104	103.3	12.5	5.4	7.8	5.8
PIP4	4.8	5.8	4.7	68.9	68.5	8.9	5.4	11.3	10.8	33.6	33.5	3.8	110	110.5	5.8	13.3	13.1	3.6
PIP5	2.2	4.5	4.5	44.3	44.5	4.8	18.8	18.8	1.6	30.2	30.1	2.1	94.6	94.8	4.6	11.7	11.7	2.5
DIP2	21.7	21.3	12.8	7.3	5.5	7.1	39.9	39.9	4.5	4.8	3.7	3.9	66.0	66.9	9.6	10.2	10.4	2.2
DIP3	29.0	29.7	7.1	11.8	8.7	9.0	24.2	29.8	19.3	20.8	25.8	15.8	81.9	80.5	15.6	11.2	11.4	5.7
DIP4	29.2	31.2	15.3	13.8	18.3	20.3	16.4	14.8	22.1	25.3	24.0	11.4	59.7	59.2	7.4	23.7	23.2	7.3
DIP5	-	2.3	-	44.8	44.7	2.7	12.9	15.5	11.1	23.1	24.2	7.8	-	-	-	-	-	-

Table 4.2 show fixed CoR locations for Ellipsoid Fitting and Sphere Fitting methods based on the global coordinate system.

71

Table 4.2 Locations of fixed CoR under Ellipsoid and Sphere Fitting methods (in mm)

Joint	Ellipsoid Fitting CoR Locations (mm)			Sphere Fitting CoR Locations (mm)		
	x	y	z	x	y	z
CMC1	6.6	6.9	-21.4	6.4	7.8	-21.3
CMC2	-7.6	7.2	-12.0	-7.8	3.4	-12.0
CMC3	-3.7	6.3	0.1	-3.8	4.1	0.0
CMC4	-8.7	6.3	10.9	-8.9	4.9	10.5
CMC5	0.5	5.2	13.4	1.9	4.8	12.9
MCP1	6.1	46.1	-45.6	6.0	46.1	-45.6
MCP2	-1.4	75.6	-12.3	-1.5	75.8	-12.3
MCP3	-2.2	72.4	10.3	-2.0	73.2	10.5
MCP4	5.2	61.4	30.7	5.4	61.9	30.9
MCP5	5.8	50.8	42.1	5.9	51.3	42.3
IP1	8.1	80.8	-43.0	8.2	80.6	-42.6
PIP2	4.5	121.1	-4.3	4.6	120.9	-4.4
PIP3	4.5	121.3	16.0	5.2	122.1	16.0
PIP4	4.0	108.3	32.1	4.3	108.0	32.0
PIP5	6.1	88.5	47.8	6.4	88.7	47.6
DIP2	9.0	146.2	1.6	9.1	145.8	1.3
DIP3	9.2	151.7	21.2	9.2	151.3	20.8
DIP4	9.3	135.0	35.0	9.4	134.7	35.0
DIP5	9.0	108.8	50.2	9.3	108.7	50.2

Table 4.3 shows instantaneous CoR locations between each two postures for ICP and 3D-Reuleaux, based on the global coordinate system.

Table 4.3 Locations of instantaneous CoRs between every two postures and the average location (in mm) under ICP algorithm and 3D-Reuleaux

Joint	ICP																	
	A			B			C			D			E			F (average)		
	x	y	z	x	y	z	x	y	z	x	y	z	x	y	z	x	y	z
CMC1	5.5	11.5	-40.2	12	9.7	-33.5	-1.9	-4.6	-28.6	12	16.4	-30.3	5.0	10.8	-31.6	7.1	8.3	-33.1
CMC2	3.4	5.9	-1.9	-7.9	17.4	-13.0	2.4	3.6	-8.2	1.6	6.9	-10.8	3.0	7.4	-10.9	-0.1	8.4	-8.5
CMC3	-9.5	34.1	5.7	-7.8	8.5	2.7	-4.6	5.0	-5.8	-1.6	14.6	4.2	-0.1	11.0	4.9	-5.9	15.5	1.7
CMC4	-7.0	19.2	22.9	-24	-78.7	-2.4	-8.0	11.5	13.7	-15	41.5	3.4	-5.9	22.9	15.8	-8.0	11.5	13.7
CMC5	6.3	15.9	21.9	129	3.4	21.2	-4.1	22.8	23.6	-18	-35.0	14.3	5.4	12.4	21.2	6.3	15.9	21.9
MCP1	5.1	54.6	-42.3	2.8	49.6	-46.0	3.8	50.8	-44.0	7.3	48.3	-42.2	7.1	45.3	-43.1	4.8	50.8	-43.6
MCP2	-0.5	79.8	-14.2	-0.5	78.9	-13.0	-6.4	77.8	-14.0	2.7	77.7	-13.0	-1.4	79.0	-14.3	-1.2	78.6	-13.5
MCP3	2.3	76.0	8.4	-0.3	75.4	8.0	-18	73.8	12.4	0.3	74.6	7.1	0.1	74.7	7.6	0.8	75.3	7.9
MCP4	3.6	64.2	27.5	-2.7	63.2	27.7	-1.8	64.2	28.1	-0.2	63.4	28.5	2.7	63.8	26.9	0.8	64.5	28.0
MCP5	5.7	51.6	42.3	6.2	52.4	42.5	5.6	73.6	54.2	3.2	54.7	38.8	5.7	52.3	42.0	4.8	53.0	41.4
IP1	8.9	82.2	-42.8	8.5	79.9	-43.6	9.7	83.6	-38.3	8.1	79.4	-43.7	8.4	80.6	-43.7	8.8	81.3	-42.1
PIP2	3.5	123	-6.4	4.0	122.2	-6.5	3.9	122.6	-6.5	4.8	121.8	-6.4	4.2	122.6	-6.4	4.0	122.4	-6.4
PIP3	3.2	123	13.4	4.3	123.3	13.6	3.5	122.5	13.4	4.9	122.6	14.1	4.5	123.1	13.7	4.0	122.8	13.6
PIP4	1.2	107	32.2	3.8	108.5	31.7	6.5	110.7	32.0	4.2	108.7	32.3	4.0	108.8	32.5	4.2	108.7	32.0
PIP5	8.2	96.2	51.8	4.9	88.3	46.9	6.5	89.8	47.1	6.0	89.2	47.3	5.9	89.1	47.3	6.4	90.9	48.3
DIP2	9.1	148	1.6	8.6	144.9	1.2	8.7	146.5	1.7	11	148.5	0.0	8.6	146.9	1.3	9.3	146.9	1.1
DIP3	8.8	153	19.7	8.1	151.9	19.1	8.7	152.4	20.9	8.4	152.2	20.6	8.1	152.8	19.1	8.5	152.5	20.1
DIP4	10	136	35.2	11	138.2	34.9	11	137.1	34.5	9.1	136.5	34.9	9.2	136.1	35.5	10	137.0	34.9
DIP5	8.5	115	50.7	8.6	109.2	50.6	9.9	109.5	50.3	8.5	108.4	50.4	4.4	102.9	50.2	9.5	107.8	50.4
	3D-Reuleaux																	
Joint	A			B			C			D			E			F(average)		
	x	y	z	x	y	z	x	y	z	x	y	z	x	y	z	x	y	z
CMC1	17.9	15.6	-32.5	4.7	-17.4	-18.6	-21	30.3	37.7	7.2	-48.6	-12.0	0.3	-13.6	-30.7	2.1	-5.0	-6.3
CMC2	-2.4	-4.1	-12.9	1.2	-6.1	-10.2	4.2	-13.9	-6.7	-0.1	-0.2	-2.6	1.5	2.5	-7.9	0.7	-6.1	-8.1
CMC3	-2.3	0.3	2.3	-4.0	0.0	-1.5	-7.5	-16.7	5.3	-6.9	-4.8	4.5	-4.3	4.9	4.1	-5.2	-5.3	2.6
CMC4	-9.0	-9.1	8.8	-13	8.6	9.6	-6.4	5.4	3.6	-14	-27.8	9.7	-13	-1.7	7.0	-11	-5.7	7.9
CMC5	-7.0	-5.9	9.4	-11	13.4	18.3	-8.6	9.4	19.9	-19	-31.1	19.0	-8.1	-1.3	-0.9	-12	-3.5	16.6
MCP1	6.2	54.8	-45.1	2.1	70.5	-45.2	3.9	49.5	-46.5	5.5	53.7	-46.3	7.9	52.0	-45.3	4.4	57.1	-45.8
MCP2	-2.4	77.7	-14.9	-1.3	77.3	-12.9	-3.7	78.2	-13.6	-4.4	78.9	-13.6	-2.5	78.3	-14.4	-2.9	78.0	-13.7
MCP3	3.4	76.9	10.2	-0.3	73.6	11.5	17.6	78.0	11.5	6.1	74.8	6.6	-1.3	72.0	9.2	6.7	75.8	9.9
MCP4	3.1	63.8	27.1	4.5	65.5	27.7	-2.1	63.3	31.3	-4.5	55.9	30.6	3.6	64.8	26.4	0.2	62.1	29.2
MCP5	5.6	47.4	42.0	5.7	52.1	44.2	9.5	52.9	44.8	8.7	53.2	44.7	6.0	52.1	43.0	7.4	51.4	43.9
IP1	9.1	82.3	-42.1	8.4	81.1	-46.4	11.9	65.0	-47.6	9.1	80.7	-41.7	7.9	81.1	-43.0	9.6	77.3	-44.4
PIP2	4.4	123.7	-4.5	3.3	120.4	-3.6	6.9	122.2	-4.3	3.8	121.7	-4.8	3.6	121.9	-5.4	4.6	122.0	-4.3
PIP3	5.2	123.1	14.1	5.0	122.1	16.8	6.0	122.2	16.6	4.2	122.0	17.1	3.6	121.9	15.1	5.1	122.4	16.2
PIP4	-3.2	101.0	28.1	4.0	108.8	33.0	10.9	109.7	31.7	3.9	109.2	32.6	3.5	108.6	32.6	3.9	107.1	31.4
PIP5	4.8	106.3	46.0	6.4	90.3	47.9	6.2	89.8	47.9	7.3	89.9	47.7	5.6	89.4	47.6	6.2	94.1	47.4
DIP2	10.5	148.6	1.6	7.9	144.7	0.8	8.4	146.2	1.3	-2.0	139.3	2.2	8.6	146.4	1.1	6.2	144.7	1.5
DIP3	9.1	152.4	20.0	10.0	151.4	20.5	8.3	152.6	21.7	7.9	152.3	20.9	7.9	152.5	20.0	8.8	152.2	20.8
DIP4	9.1	137.2	35.6	11.3	133.9	34.0	10.3	142.6	36.2	9.1	135.1	34.6	9.4	135.7	35.6	10.0	137.2	35.1
DIP5	8.6	109.5	50.6	9.3	109.6	51.0	9.7	114.4	49.5	8.1	109.2	50.0	8.8	109.3	50.6	8.9	110.7	50.3

Table 4.4 shows the minimum and maximum values of distances between CoR locations determined with Ellipsoid Fitting vs. the rest of the methods based on the

73

results from tables 4.2 and 4.3. Overall, all minimum values corresponded to the distance

between Ellipsoid and Sphere Fitting methods.

Table 4.4 Range of distances (Δ) in x, y, and z planes per joint based on the locations of CoR obtained with Ellipsoid Fitting vs. the rest of the methods.

Joint	Δ x (mm)		Δ y (mm)		Δ z (mm)	
	Min	Max	Min	Max	Min	Max
CMC1	0.2	27.6	0.9	55.5	0.1	59.1
CMC2	0.2	11.8	0.2	21.1	0.0	10.1
CMC3	0.1	5.8	1.3	27.8	0.1	5.9
CMC4	0.2	15.3	0.9	85.0	0.4	13.3
CMC5	1.4	128.5	0.4	40.2	0.5	14.3
MCP1	0.1	4.0	0.0	24.4	0.0	3.4
MCP2	0.0	5.0	0.2	4.2	0.0	2.6
MCP3	0.2	19.8	0.4	5.6	0.1	3.7
MCP4	0.2	9.7	0.5	5.5	0.1	4.3
MCP5	0.1	3.7	0.5	22.8	0.1	12.1
IP1	0.0	3.8	0.1	15.8	0.0	4.7
PIP2	0.1	2.4	0.2	2.6	0.0	2.2
PIP3	0.0	1.5	0.6	2.0	0.0	2.6
PIP4	0.0	7.2	0.2	7.3	0.1	4.0
PIP5	0.1	2.1	0.2	17.8	0.1	4.0
DIP2	0.1	11.0	0.0	6.9	0.0	1.6
DIP3	0.0	1.3	0.2	1.3	0.3	2.1
DIP4	0.1	2.0	0.1	7.6	0.0	1.2
DIP5	0.2	4.6	0.1	6.2	0.0	0.8

Results show significant differences between instantaneous CoRs versus fixed CoRs ($p<0.05$). Table 4.5 shows a summary of the results obtained from the paired t-tests, for comparisons of the Ellipsoid-fitting method with Sphere-fitting, 3D-Reuleaux, and ICP algorithm methods. Additionally, Reuleaux and ICP were compared (Table 4.5). Significant differences were found between Ellipsoid vs. 3D-Reuleaux, and Ellipsoid vs. ICP (both $p<0.02$).

Table 4.5 Summary of results from paired t-test analysis for comparing CoR methods between and within instantaneous and fixed techniques.

Pairs	df	T	P-Value
Ellipsoid vs. Sphere	19	0.96	0.348
Ellipsoid vs. Reuleaux	84	-2.48	**0.015**
Ellipsoid vs. ICP	82	-4.81	**0.000**
Reuleaux vs. ICP	83	-1.90	0.060

Figure 4.5a shows a representative figure illustrating that instantaneous CoRs found using the ICP method varied significantly from those found using the ellipsoid fitting method.

a)

- CoR between P_0_P_1
- CoR between P_1_P_3
- CoR between P_3_P_4
- CoR between P_4_P_2
- CoR between P_0_P_2
- ICP Average CoR
- CoR Ellipsoid

Ellipsoid vs. ICP
Mean Δ= 1.74 mm

b)

Δ 5.79 mm

Instantaneous CoRs for MCP2
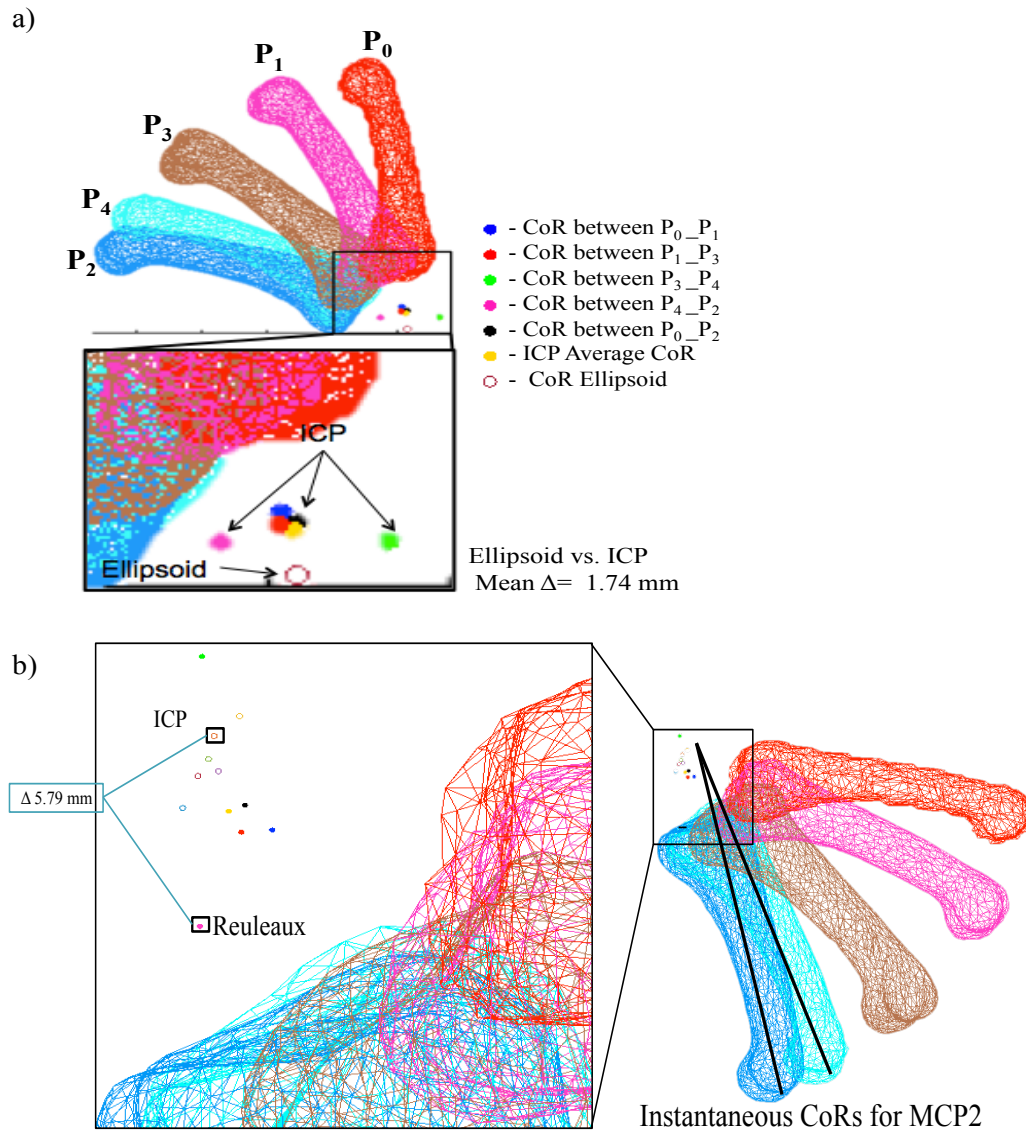
Figure 4.5a) Instantaneous CoRs for MCP2 determined with ICP (circles) and ellipsoid fitting (ring). b) Instantaneous CoRs for MCP2 found with Reuleaux (closed circles) and ICP algorithm (rings). The two locations boxed are outliers; they should correspond to a location a location of an instantaneous CoR between the same two postures. And it can be seen how dispersed they are.

Sphere Fitting resulted with the most distance from the average CoR location obtained from ICP, followed by Ellipsoid and 3D-Reuleaux (Table 4.6). Also, as Table

75

4.6 includes the average differences between CoR locations obtained with ICP versus 3D-Reuleaux, Sphere Fitting and Ellipsoid Fitting for the MCP2 joint.

Table 4.6 Average distance (in mm) between CoRs locations obtained from ICP vs. Sphere, Ellipsoid and 3D-Reuleaux for the resultant ($\Delta CoR_{Resultant}$) including all bones pooled, and for the MC2 bones ΔCoR_{MCP2} as a sample data.

Pairs	$\Delta CoR_{Resultant}$ (mm)	ΔCoR_{MCP2} (mm)
Sphere vs. ICP	3.77	2.90
Ellipsoid vs. ICP	1.74	3.19
Reuleaux vs. ICP	0.84	0.49

Outliers were found for the Reuleaux and ICP methods (Table 4.4). These outliers emerged as the angle decreased, although these methods displayed greater accuracy at a larger range of angles. Based on the results, instantaneous centers were not suitable for angles between the two adjacent distal segments that are 1.3 degrees for the CMC joints, 5.43 for the MCP joints and 2.31 degrees for the DIP joints, or smaller. Figure 4.5b displays an example of instantaneous CoRs and outliers found under 3D-Reuleaux and ICP methods.

4.4.   Discussion

In general instantaneous CoR methods, ICP algorithm and 3D-Reuleaux, were the most effective methods by taking into account the anatomical joint structure with the corresponding gliding and rotation movements on the CoR locations based on the joint angles. There was a significant difference between CoR locations under instantaneous vs. fixed methods (Table 4.2- 4.5). Several studies have validated their models by comparing how close their results kinematics aligned to the "gold standard" bone-pin kinematics based on Sphere Fitting techniques (Lopomo, et al., 2010; Lempereur et al., 2010; Ehrig et al., 2006; Halvorsen et al., 1999). In this study, deviating from Sphere Fitting meant

that they were more realistic, taking into account the joint structure and resulting with variable links lengths as a function of the joint angle.

Although, based on the results from the t-test we cannot conclude that a significant difference exists within fixed CoR methods- between Sphere Fitting and Ellipsoid Fitting (Table 4.5), fitting an ellipsoid is recommended over a sphere for finger joints because a higher percentage of the curvature of the joint was taken into account when establishing its centers. Similarly, based on the paired t-test it cannot be established that a significant difference exists within instantaneous CoR methods- between 3D-Reuleaux and ICP (Table 4.5).

All methods were further compared by evaluating the average distances between resultant CoRs from ICP vs. the rest of the methods (Table 4.6). Results showed the Reuleaux CoR located much closer to the ICP CoR than either of the fixed methods ($p > 0.05$). The locations of the CoRs obtained from ellipsoid were at a similar distance away from the average CoR obtained from ICP.

Instantaneous CoRs between two segments are identified by the rotation and the gliding action (translation) at the joints. The anatomical structure of the bones is considered when determining the location of the instant centers, making these types of methods not only significantly different than the fixed methods (Table 4.5) but also more robust and accurate. Kinematics using fixed CoRs assumes a fixed rotational axis based on simple links representing each segment, and pin joints representing centers of rotation. Under the pin joint assumption, irregularities of bone shape along the joints are not considered and physically unrealistic postures could be acquired (Figure 4.1).

Reuleaux method has been used to determine finger segments (Buchholz et al., 1992), based on radiographs, a 2D analysis. This study used data extracted from CT scans to adapt a 3D version of Reuleaux, described by (Eberharter & Ravani, 2006), to human joints and more specifically, hand joints. This study applied this 3D-Reuleaux to the human joints for the first time. Other studies for 3D kinematics generally based their kinematics using motion capture analysis (Miyata et al., 2006; O'brien et al., 2000).

In this study, four methods were proposed to determine CoR locations and establish 3D kinematics of the hand based on bone geometry. Taking into account the geometry around the anatomical joint for establishing CoRs, leads into more accurate and repeatable predictions. ICP algorithm resulted in the most robust method for identifying instantaneous CoR between two adjacent 3D segments. Although, in some cases faster approaches, such as ellipsoid fitting, can be useful and adequate like in the case kinematics for visualization purposes (e.g. video games). Sphere and Ellipsoid Fitting methods were determined to be faster because they just need to be identified once and there is no need on developing a function to determine CoR locations and link lengths based on the joint angles or to analyze the CoR location between each two postures.

4.5. Conclusion

In this study, four methods were proposed to establish CoRs for finger kinematics based on bone structural geometry. They all can be used to describe finger motion, although with different levels of accuracy. However, results from this study suggest that ICP and 3D- Reuleaux resulted in the most accurate methods to determine CoR locations

based on bone geometry (Table 4.5). The necessary level of accuracy needed for modeling finger motion, varies with different applications. Thus, all four methods discussed have their own place in the very broad field of hand modeling. For example, in many modern video games and virtual reality, human hands are included with rather realistic movements to enhance the user experience. The degree of accuracy needed for this motion is rather small, and using a quicker method such as pin joints most likely would be preferred. In such a case the Sphere or Ellipsoid Fitting methods would be ideal. However, when assessing work limits through biomechanical, ergonomic or clinical assessments where a doctor performs surgery, a high level of accuracy is required. In these cases, accurate CoR locations and posture predictions are preferred, regardless of time. In instances such as these, the Reuleaux or ICP algorithm methods would be a much more appropriate approach to CoR estimation in this case. Results from this study highlight the differences in CoR locations when instantaneous CoRs are considered (Tables 4.5 and 4.6). These CoR locations affect kinematics, and joint and tendon moment loads.

4.5.1. *Limitations and Future Work*

This study was limited by existing hand CT images, which were in pre-determined postures based on common grasping postures (e.g. power grip, pinch grip) rather than standardized posture with controlled changes in joint angles. Future work should include further analyzing CoR locations based on joint angle so that a more accurate model can be developed. It would also be beneficial to gather data from several subjects in more standardized postures to maximize the joint angle analysis, which would

enable an evaluation of size variation and sex effects on the accuracy of the methods. Standardized postures could include a flat hand, a resting hand, and grasping of spheres/balls or cylinders (Miyata et al., 2007).

Additionally, based on the paired t-test it cannot be established a significant difference exists between Reuleaux and ICP. However, the p-value approached the borderline of significance and it should be further investigated with more a larger sample size and a standardize data based on controlled joint angles instead of predetermined postures.

4.5.2. *Acknowledgements*

CHAPTER 5 Development of Statistical Models of Hand Skeletal Geometry

Abstract

An accurate prediction and representation of skeletal geometry is needed to improve biomechanical models used to simulate hand posture and hand interactions with external surfaces and objects. In this study, statistical models were developed to predict bone surface geometry and the positions of the bones with respect to the skin. This was achieved by aligning, morphing and fitting template meshes onto bone geometries extracted from hand CT scans. Measurements obtained from the skin surface geometry of the template hand were rotated and transformed accordingly with the template so that the hand length, breadth and thickness could be measured for each scan and the relationships between skin surface and bone locations could be modeled. Principal component analysis (PCA) was applied to the resulting nodal coordinates, and regression on principal component (PC) scores was performed to develop models that describe how these scores, and in turn, hand bone geometries, vary based on hand length, hand breadth, hand thickness, and sex. A Linear Mixed Models (LMM) analysis was performed on cross-sectional areas at five different locations along the long axis of each individual finger bone to assess the importance of interaction effects. The model was evaluated by comparing predicted bone geometry with the geometry extracted from the CT scans. The resulting statistical models can be incorporated into biomechanical models representing men and women with a wide range of hand size and shape.

5.1 Introduction

Three-dimensional (3D) anthropometric hand models can be used to predict joint angles, contact point locations and hand envelope, all of which greatly vary with respect to hand size and shape. Much progress has been made in the development of biomechanical models that can be computerized to apply various aspects of hand function. Subject- or population-specific 3D hand models have been widely used in biomechanics and ergonomics research to characterize hand shape, posture and movements (Seo et al., 2007; Miyata et al., 2007; Frederick and Armstrong 1995; Buchholz & Armstrong, 1992), and in medicine, for surgical planning and navigation, and for hand function assessments (Figueroa et al., 2014). Work has been focused on developing the kinematics for hand models using vision-based methods (e.g. 3D markers) to obtain kinematic joint centers for scaling and/or calibration (Cerveri et al., 2005; Kurihara & Miyata, 2004). Miyata, et al. developed a statistical shape model for predicting hand skin surface based on skin landmarks from plaster mold models and incorporating a skeleton based from motion-capture data (Miyata, et al., 2013, 2012).

Rogers et al. collected hands from different subjects in several postures (Rogers, et al. 2008) to reconstruct a scalable 3D-hand model. However, marker positions were limited to the palmar surface of the hand, resulting in rough 3D shapes without hand thickness information. Generally, the dimensions of each finger segment in previous hand models assume segment symmetry across its breadth (Buchholz, Armstrong & Goldstein, 1992). Additionally, they are scaled based on relative distances between pairs of markers defining link lengths (Delp et al., 2007; Dennerlein et al., 1998) or as a function of hand length and breadth based on fractions proposed by Buchholz, Armstrong & Goldstein

(1992). However, it is not known how handbreadth and thickness are related to bone shapes and sizes. Underlying skeletal critical dimensions from bone geometry can be used to develop factors to predict bone shapes and sizes, with the purpose of accurately determining locations of anatomical joint centers, tendon attachments, hand envelope, and ultimately for predict hand placement.

Currently, 3D bone and surface geometries can be obtained from CT Scans with a high level of accuracy (Lian et al., 2010). Recently, medical images have been widely used to develop using statistical shape analysis to reconstruct subject-specific 3D models. Statistical shape models based on Principal Component Analysis (PCA) and Regression have been developed for multiple parts of the body, such as knee (Tsai et al., 2015), femur (Klein et al., 2015; Bedbenner et al., 2010), clavicle (Lu & Untaroiu, 2013), rib cage (Shi et al., 2014), child pelvis (Reed et al., 2009), torso (Hsiao et al., 2009), hand skin surface (Miyata et al., 2013), and whole body (Park, et al., 2015). All these methods are based on manual landmarking. In practice, manual landmarking is difficult and error prone (Mutsvangwa, 2015). Recently, there has been considerable progress on general landmark-free approaches by defining correspondences automatically and using statistical shape modeling analyses (Mutsvangwa, 2015; Brett & Taylor, 2000). With the aim of providing a subject-specific 3D model, Giles et al. (2010) proposed a method for fitting a template of skeleton to a given volumetric shape extracted from medical images. Although Giles et al. shows encouraging results, it uses PCA only to match existing surfaces by applying elastic deformation to individual segments and not to perform independent predictions of the skeleton shape and size. PCAR is widely used for predicting shape/sizes of 3D meshes because it allows the user to reduce the data from

83

more than tens of thousands of points to a set number of principal components (PC) by applying a projection model for multivariate factor analysis, aiming to find a low-dimensional manifold in the Cartesian space of the data (Fodor, 2002). PCA also allows independent visualization of the main modes of variation (PC).

Prediction models of individual bone surfaces of the hand can be beneficial for orthopedic surgical planning, biomechanics research, and 3D-bone shape reconstruction. Although there has been several reports on the development of statistical shape models of individual bones (Klein et al., 2015; Bedbenner et al., 2010; Reed et al., 2009), there has to date been little reported on individual hand bone surface geometry.

Thus, this study aimed to use PCAR to 1) develop landmark-free statistical models to describe variations in individual hand bone geometries and in the full skeleton of the hand with respect to hand length, hand breadth, hand thickness and sex, and 2) scale skin surface based on hand bone skeleton shape/size predictions.

5.2   Methods

To achieve the above aims, protocols developed in Chapter 3 were used to segment clinical CT data and to establish the coordinate systems for the 3D surfaces. The 3D models of the template hand from Chapter 3 were used to create homologous surfaces to represent each hand. Additionally, kinematics developed in Chapter 4 from the average location of the CoR from ICP were used to rotate finger segments of fitted hands for 1) obtaining hand skin measurements in a common posture, 2) performing whole hand skeleton predictions, and 3) evaluating final predictions in the original postures.

5.2.1 *Sample Collection and Geometry Extraction*

Anonymized clinical CT scans of 29 male and 14 female hands were obtained through collaboration with the University of Michigan Department of Radiology. An institutional review board at the University of Michigan approved the protocol. The CT scans were collected using a resolution of 512 x 512 pixels with an in-plane resolution that varied from 0.135mm to 0.644mm. Patient ages ranged from 19-79 years old (Appendix F). Hand length, thickness, and breadth were moderately correlated, as expected (Figure 5.1). Height (stature), hand length hand breadth, and hand thickness percentiles on Figure 5.1 were based on Garret (1971).
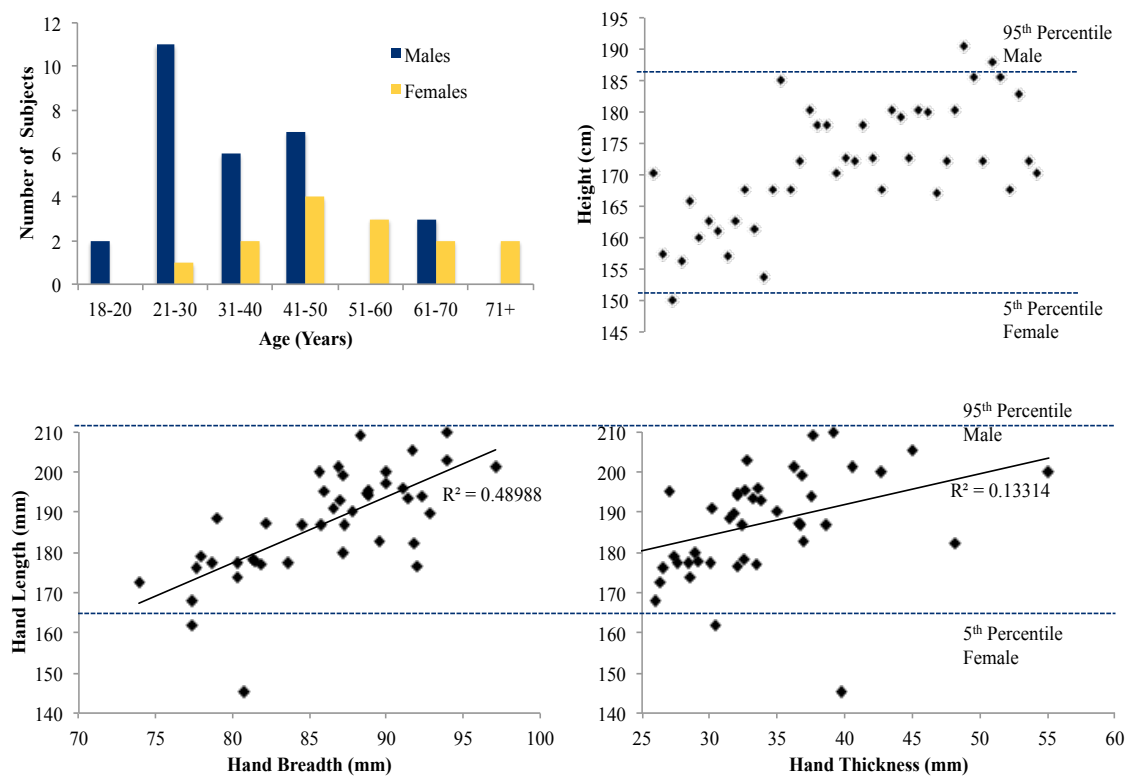
Figure 5.1 Subject Statistics. Hand length, breadth and thickness based on Garret (1971)

Twenty hand bones, two forearm bones, and skin were segmented and 3D surfaces were extracted using Amira ® software (v. 5.2) with a 3D volume-rendering mode of Hounsfield Unit threshold of -200 for bone surfaces and -260 for skin surfaces. The eight

carpal bones were considered as one bone (Wu et al., 2005). Using an automated script in MeshLab (v. 1.3.2, sourceforge.net) the 3D meshes (in PLY format) were simplified using the quadric edge collapse decimation filter (Klein et al., 2015; Pratt et al., 2010; Garland, 1999) to the targeted size of polygonal faces. The target resolution per bone was selected depending on the complexity of the bone geometry and ranged from 15,000 faces for the carpals to 1,000 faces for the distal phalanges.

All simplified 3D meshes were then imported into MATLAB (MathWorks, Natick, MA) and reflected along the long axis to generate 3D right-hand bone and skin surfaces, performed under the assumption of bilateral symmetry of the human body across the sagittal plane (Hargittai & Hargittai, 1994). Each triangulated surface representing individual bone segment s of a right hand per subject i was described with a geometry vector $\boldsymbol{g}_i$.

$$\boldsymbol{g}_i = [(V_{1,1,x} \quad V_{1,1,y} \quad V_{1z}), \quad \ldots \quad (V_{s,j,x} \quad V_{s,j,y} \quad V_{s,j,z})]$$

(1)

Where V represents each point/vertex j on the surface mesh for bone s. Thus, j range from 1 to m (m equals the number of vertices/points on each individual 3D surface which differs from type of surface) and s range from 1 to n (n=23 for the number of surfaces modeled- 19 phalanges, 1 set of carpals, 2 forearm bones and 1 skin surface) and i range from 1 to 43 (number of subjects).

Joint centers of rotation (CoR), from the average CoR location obtained from the ICP methodology determined previously, in Chapter 4, were identified in the template hand. For the sake of simplicity, the kinematics in this study were developed as simple links with fixed CoRs. To avoid overlapping between two adjacent bones, a minimum of

1 mm was set as a minimum distance between two consecutive bone segments, based on results from Chapter 3.

5.2.2 *Standardizing the Data*

5.2.2.1 *Morphing and Fitting Process of Hand Bones*

Figure 5.2 illustrates the landmark-free processes for standardizing the data by using the template developed in Chapter 3. Local and global coordinates systems developed in Chapter 3 were applied to each subject's hand (target). The surfaces of the template hand, developed in Chapter 3, were aligned to each target by the global origins. Local axes of each template bone were then aligned and scaled individually into the corresponding geometry of target. Template bone geometries were further aligned to each targeted bone using a Procrustes approach (Goodall, 1991; Gower, 1975). Then, each template bone was morphed to match the geometry of the corresponding bone geometry from each scan. Morphing was performed using a method based on radial basis functions (RBF) using a thin-plate-spline kernel function ($\phi(r) = r^2 \ln(r)$). This methodology is widely used to morph one surface to another based on a set of landmarks or vertices (Klein et al., 2015; Park, et al., 2015; Bennink et al. 2006) to obtain sets of morphed nodes representing each segment's geometry from each clinical scan. The information on CoRs distal end of each bone and at the carpals were transformed and rotated accordingly when fitting the surfaces.

| Align Template's Carpals with Target hand | → | Use ICP to align bone axes of template bones with target | → | Scale template axes (X,Y, Z) to fit target | → | Morph template to fit target with RBF** | → Fitted data |
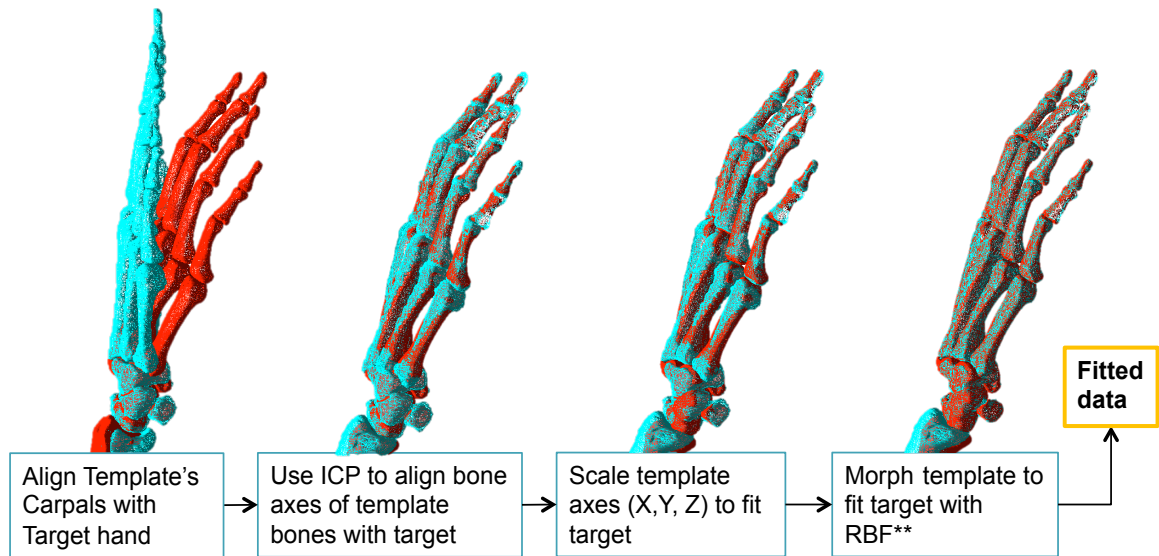
Figure 5.2 Fitting template with landmark-free alignment, morphing and fitting processes for template hand and wrist bone meshes onto extracted hand bone surface geometries to standardize the data.

All fitted hands were rotated to a common posture (flat hand) to standardize the data for the statistical analysis (Park et al., 2015; Reed & Parkinson, 2008), for acquiring skin reference points and anthropometric measurements, and subsequently for shape/size predictions of the whole hand.

5.2.2.2 *Skin Surface Reference Points*

Reference points were identified from the skin surface geometry of the template hand based on standard techniques of measurement defined by Garret (1971) (Figure 5.3).
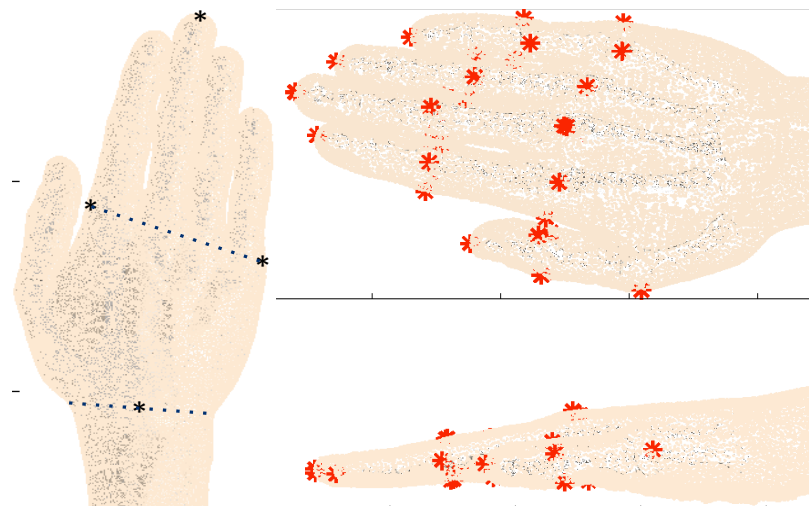
Measurement	Short Description
Hand Length	Wrist crease to the tip of Digit 3 (middle finger)
Hand Breadth	Metacarpals (MC)
Hand Thickness/Depth	Metacarpal III (MC3)
Digit 1: Breadth	Interphalangeal joint (IP)
Digit 1: Thickness/Depth	Interphalangeal joint (IP)
Digit 2: Breadth	Proximal Interphalangeal joint (PIP)
Digit 2: Thickness/Depth	Proximal Interphalangeal joint (PIP)
Digit 3: Breadth	Proximal Interphalangeal joint (PIP)
Digit 3: Thickness/Depth	Proximal Interphalangeal joint (PIP)
Digit 4: Breadth	Proximal Interphalangeal joint (PIP)
Digit 4: Thickness/Depth	Proximal Interphalangeal joint (PIP)
Digit 5: Breadth	Proximal Interphalangeal joint (PIP)
Digit 5: Thickness/Depth	Proximal Interphalangeal joint (PIP)

Figure 5.3 Reference points placed skin surface of the template hand used to measure hand length, width and thickness (Left), and length, breadths and thicknesses/depths for each finger (Right). Hand measurements based on Garret (1971).

These locations were rotated and transformed accordingly with the template alignment, morphing and fitting so that 1) hand length, width and thickness could be measured for each scan, 2) relationship between skin surface and bone locations could be modeled, and 3) allows to position the bones with respect to the skin surface.

5.2.3   *Analysis of bone cross-section areas*

Similar to the methods in Klein et al. (2015), a Linear Mixed Models (LMM) analysis was performed on the cross-sectional areas at five different locations along the shaft of the finger bone surfaces (Figure 5.4a). The LMM analysis was performed to 1)

determine what are the significant predictors to be included in the statistical models, 2) investigate whether interaction effects between predictors could be ignored, and 3) to test the assumption of symmetry across the thickness/breadth of finger segments (Buchholz, Armstrong & Goldstein, 1992). Random effects with an assumed normal distribution were age, height, weight, race, bone length, hand length, handbreadth, and hand thickness. Fixed effects were sex and the cross-sectional locations. The α-level indicating significance was set to $p < 0.05$.

5.2.4   *Principal Component Analysis and Regression (PCAR)*

Statistical models of bone surfaces were developed using PCAR methods used in this study follows the method discussed by Reed and Parkinson (2008), Klein et al. (2015) and Jolliffe (2002). All surfaces were aligned using Procrustes (Goodall, 1991; Klein et al. (2015). The geometry vector g_i of each segment per subject (*i*) was defined with a length of L= total number of nodes x 3 for coordinates (*3i*). All information gathered about the subjects was added to this g_i matrix, as well as extra columns to further describe each subject (e.g. sex, locations of CoRs on each segment, local coordinate system, bone lengths, bone thicknesses). All subjects' geometry vectors were compiled in a geometry matrix G, which was centered by subtracting from each subject's vector g_i the overall mean $\overline{g}$. PCA was computed by calculating the eigenstructure of the covariance matrix of **G** with the purpose of finding the linear projection that reduces dimension of the matrix while preserving the variance in the data. A regression analysis was performed to predict PC scores from subject anthropometric data (hand length, hand width, hand thickness, sex) (Reed & Parkinson, 2008). PC scores were used to reconstruct finger bone surface geometries (Appendix H). The PCAR models in this

study used the same number of PC scores as number of subjects (43 subjects), covering more than 99% of the variance in the data. Statistical models using PCAR (Tsai, 2015; Li, 2011; Reed and Parkinson 2008) were developed for 1) each phalanx surfaces for female and male, and 2) the hand whole skeleton surface for female and male were developed using PCAR.

To model the whole skeleton, the initial geometry vector g_i contained the data of the whole skeleton instead of each bone surface so that the whole hand could be predicted. All information gathered about the subjects was added to this $\boldsymbol{g_i}$ matrix, as well as extra columns for further describing each subject (e.g. finger measurements, skin surface measurements, sex, locations of CoRs on each segment, local coordinate system, bone lengths, bone thicknesses). This matrix included subject specific external anthropometric data from the reference points identified on the skin surface. By including these reference points and their relationship with the skeleton, the hand and finger surface envelop can be estimated based on the skeleton shape/size predictions.

5.2.5 *Evaluating the Error of the Prediction Models*

A leave-one-out cross validation (Klein et al., 2015) per subject was performed to evaluate the statistical models. This method was performed by removing one subject from the data, refitting the regression model to the data without that subject, predicting that subject's geometries and calculating the error in the resulting model.

Procrustes Analysis (Gower, 1975) and with ICP algorthm (Besl & McKay, 1992) were used to superimpose each individual bone segment predictions to each subject's original fitted surface (observed values) for shape comparisons. The Mean Square Error

(MSE) and Mean Absolute Errors between the predictions and the observed geometries were calculated based on the sum of Euclidean distances between corresponding vertices.

$$MSE = \frac{1}{m}\sqrt{\sum_{j=1}^{m}(g_{Predicted,j} - g_{Observed,j})^2}$$

(2)

$$MAE = \frac{1}{m}\sum_{1}^{m}|g_{Predicted,j} - g_{Observed,j}|$$

(3)

where m is the number of vertices per surface modeled.

Whole-hand skeleton predictions were evaluated against the fitted hands representing the original data in 1) the common posture, and 2) in the posture of the original scan. Procrustes error, MSE and MAE were calculated to evaluate the predictions of the whole hand skeleton and skin surface measurements.

5.3   Results

5.3.1   LMM Analysis on the Total Cross-Section Areas

An LMM analysis was performed to evaluate the significance of the predictors based on cross-sectional areas at five different levels across the shaft of each bone. The predictors considered were age, height, weight, race, bone length, hand length, handbreadth, hand thickness and cross-sectional location.

LMM results varied between bones. Table 1 shows a summary of the effect significance per bone based on the analysis of 215 cross-sectional areas (43 subjects, 5 levels per bone).

Table 5.1 Significance based on 215 cross-sectional areas (43 subjects, 5 levels per bone) for the predictors considered for the model: age, height, weight, race, bone length, hand length (HL), handbreadth (HB), hand thickness (HT) and cross-sectional location (location level), and interaction between sex and hand measurements. Significance set at p<0.05.

Bone Segment	Age	Sex	Height	Weight	HL	HB	HT	Bone length	Location Level	HL_Sex	HW_Sex	HT_Sex
MC1	✔[3]	✔[5]			✔[5]	✔[4]	✔[2]	✔[5]	✔*		✔[1]	✔[1]
MC2		✔[2]	✔[2]		✔[5]	✔	✔[4]	✔[3]	✔*			
MC3	✔[2]	✔[5]	✔[4]	✔[1]	✔[4]	✔[5]	✔[2]	✔[3]	✔*			
MC4		✔[5]			✔[4]	✔[3]	✔[5]	✔[5]	✔*	✔[1]		
MC5		✔[4]	✔[4]	✔[3]	✔[4]	✔[2]	✔[2]	✔[4]	✔*			
PP1		✔[5]			✔[4]	✔[5]	✔[4]	✔[5]	✔*	✔[1]		
PP2	✔[2]	✔[4]	✔[4]		✔[5]	✔[2]	✔[2]	✔[4]			✔[1]	
PP3		✔[5]	✔[4]		✔[4]	✔[3]	✔[4]	✔[3]	✔*			
PP4		✔[4]		✔[3]	✔[3]	✔[2]	✔[5]	✔[2]	✔*			✔[1]
PP5		✔[2]			✔[4]	✔[4]	✔[2]	✔[4]		✔[1]		
MP2	✔[3]	✔[5]	✔[4]		✔[4]	✔[2]	✔[4]	✔[5]	✔*			
MP3		✔[4]	✔[4]		✔[5]	✔[4]	✔[4]	✔[4]	✔*			
MP4		✔[5]			✔[4]	✔[4]	✔[3]	✔[3]	✔*			
MP5		✔[4]	✔[4]		✔[4]	✔[5]	✔[2]	✔[4]	✔*			
DP1		✔[4]			✔[4]	✔[4]	✔[5]	✔[5]	✔*	✔[1]		
DP2				✔[4]			✔[3]	✔[2]	✔*			✔[1]
DP3	✔[3]	✔[5]	✔[4]		✔[4]	✔[4]	✔[2]	✔[4]	✔*			
DP4			✔[4]			✔[3]		✔[3]				
DP5					✔[4]	✔[3]	✔[4]					

[1]P<0.05 for less than 50 cross-sectional areas
[2]P<0.05 for 51-100 cross-sectional areas
[3]P<0.05 for 101-150 cross-sectional areas
[4]P<0.05 for 151-200 cross-sectional areas
[5]P<0.05 for 201-215 cross-sectional areas
*P<0.05 difference in location level of cross-sectional areas

Hand length, breadth and thickness were significant predictors for 84%, 67% and 36% of the bones, respectively. Age and sex were not found significant for the majority of the bones (p >0.05). The 2-way interactions were examined between hand length,

width and thickness with sex. Although bone length was found to be significant, it will not be included in the statistical model because the purpose of the model is to use external anthropometric data to predict surfaces shapes/sizes. Overall, no significance was found for these 2-way interactions.

In general, male phalanges have a higher total bone area than female bones (p<0.05) when other predictors are held constant. Representative data for the sex effect on total bone area at cross-sections located at 5 levels along the shaft are shown in Figures 5.4b and 5.4c.
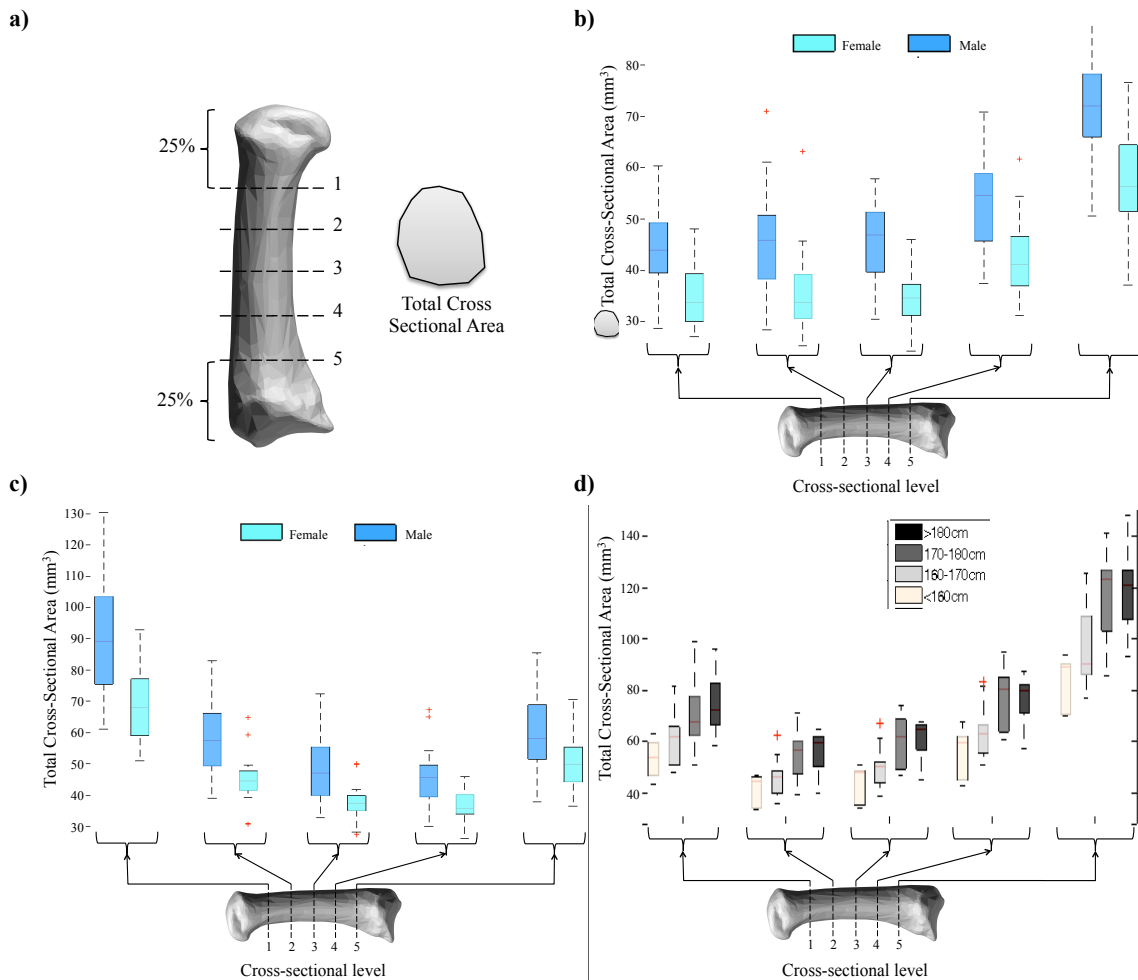
of the PP2 bone, used to analyze thickness along the shaft.
l bone length below the max point on the Y-axis and cross-
ve the minimum point on the Y-axis. Cross-section 2, 3, and

4 were spaced evenly between 1 and 5. Distribution of cross-sectional areas by sex and cross-section location level for b) MP3 and c) MC4 bone surfaces. d) Distribution of PP1 (representative of data) cross-sectional areas by stature (cm) and cross-section location level.

For all MP, PP and DP bones, Level 5 cross sections (proximal side of shaft) obtained the highest total bone area (Figures 5.4b and c). In contrast, the largest total bone area for MC bones was located along Level 1 (distal side of shaft) ($p<0.05$). The same behavior between levels was observed for hand length ($p<0.05$). The total bone area and cortical bone area at each of the levels increase when stature increases ($p<0.05$) (Figure 5.4d) holding other predictors constant.

5.3.2   *Statistical Shape Models using PCAR*

Statistical shape models were developed in this study to predict shapes and sizes of individual phalanges using principal component analysis and regression (PCAR). Additionally, a statistical shape model was developed to predict shape and size of a whole hand skeleton, including skin measurements with the purpose of identifying the factors for scaling the skin surface.

5.3.2.1   *Predictions of Individual Phalanx Bone Geometries*

PCA was used to reduce the original geometry data of each bone surface by applying a projection model for multivariate factor analysis, aiming to find a low-dimensional manifold in the Cartesian space of the data (Fodor, 2002). Table 5.2 shows representative data of the results for the Euclidean Error (MSE), Mean Absolute Error (MEA) and Procrustes Error for evaluating the shape predictions. These results are 50% lower than Devries et al. (2008), who reported Mean Euclidean Distances close to 0.9 mm for the MP and DP bones, when testing the results of their 3D meshes.

Table 5.2 Mean square error (MSE) and standard deviation (SDev) values based on the Euclidean distances. Also included the Mean Absolute Error (MAE) for all predictions of the DP2 and MP5 bone geometries, all hand bone predictions in the common posture and rotated to the predict each subject's original posture. All distances are in millimeters (mm).

Subject	DP2			MP5			Common Posture			Target Original Posture		
	MSE	SDev	MAE	MSE	SDev	MAE	MSE	Sdev	MAE	MSE	Sdev	MAE
Sub8	0.27	0.11	0.24	0.26	0.11	0.23	7.1	1.0	20.1	15.8	12.4	21.3
Sub10	0.22	0.11	0.19	0.17	0.09	0.15	11.4	3.6	48.7	35.0	34.7	48.6
Sub16	0.49	0.24	0.43	0.53	0.25	0.47	13.9	11.0	63.5	53.1	34.8	66.5
Sub17	0.57	0.24	0.52	0.42	0.16	0.39	4.0	3.4	12.2	9.2	8.1	15.2
Sub19	0.33	0.15	0.30	0.30	0.11	0.28	5.3	2.1	21.4	5.6	4.8	8.3
Sub20	0.29	0.13	0.26	0.43	0.20	0.39	12.1	11.0	28.5	22.1	18.0	32.6
Sub24	0.21	0.09	0.19	0.24	0.11	0.21	21.8	12.9	21.6	9.9	8.3	16.3
Sub26	0.35	0.17	0.31	0.19	0.09	0.17	5.9	5.3	18.5	14.1	12.0	18.3
Sub30	0.37	0.16	0.33	0.43	0.16	0.40	7.8	6.3	14.0	10.6	9.2	14.1
Sub33	0.28	0.13	0.25	0.30	0.13	0.27	61.1	10.5	96.8	84.0	33.9	107.0
Sub35	0.18	0.09	0.16	0.22	0.10	0.20	8.7	4.8	18.8	16.6	8.8	19.4
Sub36	0.61	0.26	0.55	0.32	0.13	0.29	4.6	3.1	27.4	18.5	20.2	32.8
Sub39	0.30	0.13	0.27	0.27	0.12	0.24	16.2	8.6	39.6	30.4	25.4	43.8
Sub41	0.27	0.11	0.24	0.19	0.09	0.17	3.8	1.5	13.9	10.1	9.6	15.7
Sub42	0.37	0.17	0.33	0.16	0.07	0.15	10.6	4.0	13.4	10.0	9.6	18.8
Sub44	0.33	0.15	0.30	0.22	0.10	0.20	18.9	5.8	19.7	14.7	13.1	23.1
Sub45	0.32	0.15	0.28	0.85	0.45	0.72	120.6	73.3	152.7	146.7	62.0	180.6
Sub47	0.26	0.12	0.22	0.16	0.08	0.14	5.8	4.5	29.4	21.2	20.4	28.6
Sub49	0.31	0.11	0.29	0.26	0.14	0.21	2.5	14.9	10.2	8.3	5.9	15.3
Sub50	0.24	0.12	0.21	0.24	0.11	0.22	6.7	3.4	20.0	15.1	13.1	21.5
Sub52	0.23	0.11	0.20	0.24	0.11	0.21	24.4	13.1	32.8	29.5	14.4	33.7
Sub53	0.29	0.12	0.27	0.24	0.10	0.21	12.8	8.3	13.0	9.8	8.6	13.1
Sub57	0.49	0.24	0.43	0.28	0.16	0.24	16.2	9.9	16.3	13.3	9.4	17.4
Sub60	0.25	0.12	0.22	0.19	0.09	0.17	12.5	10.4	13.9	11.0	8.5	17.4
Sub65	0.33	0.13	0.31	0.18	0.09	0.15	12.0	6.7	16.1	12.2	10.4	17.1
Sub66	0.36	0.17	0.31	0.36	0.15	0.33	19.0	5.9	28.7	21.4	19.1	31.2
Sub71	0.18	0.09	0.16	0.20	0.08	0.18	17.5	20.9	20.9	13.1	11.6	22.3
Sub72	0.32	0.15	0.28	0.29	0.13	0.26	13.6	2.4	37.5	10.5	8.7	17.5
Sub76	0.23	0.11	0.20	0.33	0.14	0.30	21.3	6.2	22.6	15.6	14.5	27.0
Sub77	0.31	0.14	0.28	0.35	0.18	0.30	24.6	4.7	29.4	19.1	15.6	26.8
Sub79	0.55	0.21	0.51	0.29	0.10	0.27	11.9	2.1	14.1	11.2	8.7	13.9
Sub81	0.48	0.21	0.44	0.32	0.16	0.28	15.7	9.2	29.6	19.5	22.4	34.9
Sub82	0.31	0.14	0.27	0.22	0.11	0.19	14.0	5.9	14.4	12.1	7.9	17.9
Sub83	0.63	0.33	0.54	0.22	0.09	0.20	14.2	3.2	19.8	14.6	13.3	23.1
Sub84	0.65	0.30	0.57	0.21	0.11	0.17	19.9	6.0	19.5	16.2	11.0	20.1
Sub85	0.51	0.23	0.46	0.29	0.13	0.26	14.8	4.5	16.6	11.5	9.3	18.8
Sub86	0.35	0.15	0.31	0.28	0.12	0.25	3.5	5.5	26.7	17.8	20.0	26.9
Sub90	0.21	0.09	0.19	0.22	0.10	0.19	21.8	18.4	23.9	14.0	12.3	19.0
Sub96	0.66	0.28	0.59	0.23	0.11	0.20	16.7	11.5	19.7	14.6	13.2	21.5
Sub99	0.40	0.22	0.34	0.24	0.11	0.21	12.3	5.1	29.8	22.7	19.3	32.8
Sub103	0.25	0.11	0.22	0.26	0.12	0.23	4.8	1.5	24.8	17.9	17.7	25.2

Figure 5.5a shows resulting individual bone models (in cyan) superimposed to the original fitted data (cyan).
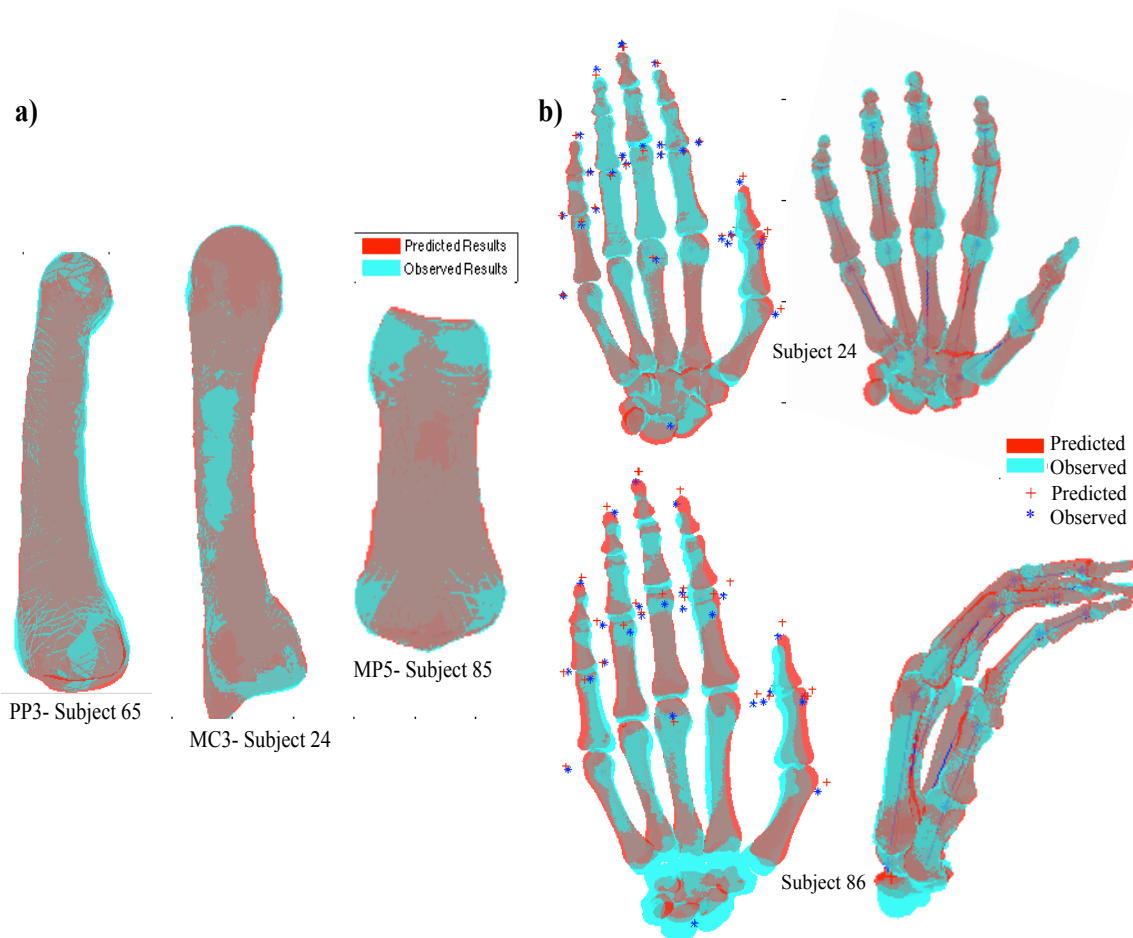
Figure 5.5 a) Illustration of predicted individual bones (red) aligned to the original fitted data (cyan) representing the true value of the geometry (not to scale). b) Hand skeleton predictions in template's posture, including skin landmarks related to skin surface and bone locations. The hand on the right is the prediction for the same subject on its original posture; links lengths are shown in blue.

PCA is also useful to decompose the set of shapes to investigate the correlations by visualizing the principal modes. These main modes are ranked in descending order of variance and can be visualized by modifying one component at a time. Table 5.3 summarizes the number of modes needed to reach 99% of the variance per type of bone. To reach, DP bones needed the lowest number of PCs, and MCs and Carpals needed the highest number, indicating the greatest variability among individuals in bone size and shape.

97

Table 5.3 Number of Principal Components (PCs) needed to account for 99% of the variance in the data

Bone Segment	Number of PCs to reach at least 99% of variance
Distal Phalanges (DP)	12
Middle Phalanges (MP)	20
Proximal Phalanges (PP)	23
Metacarpal (MC)	26
Carpals (CAR)	31

Appendix G a full list of the principal modes and their corresponding variance per individual bone surface geometry.

Modifying one component at a time illustrates the principal modes. Figure 5.6 illustrates how the PC affected the shape variance for the first 3 PCs of the MP3 bone. These first 3 PCs accounted for 81.5% of the variance, with variance fractions of .59, .14 and .08, respectively. From Figure 5.6 we can interpret that the primary relation of the first PC corresponds to bone length, based on changes observed from PC1. The second PC shows variations slightly related to width/thickness and the third PC is associated with bone curvature.
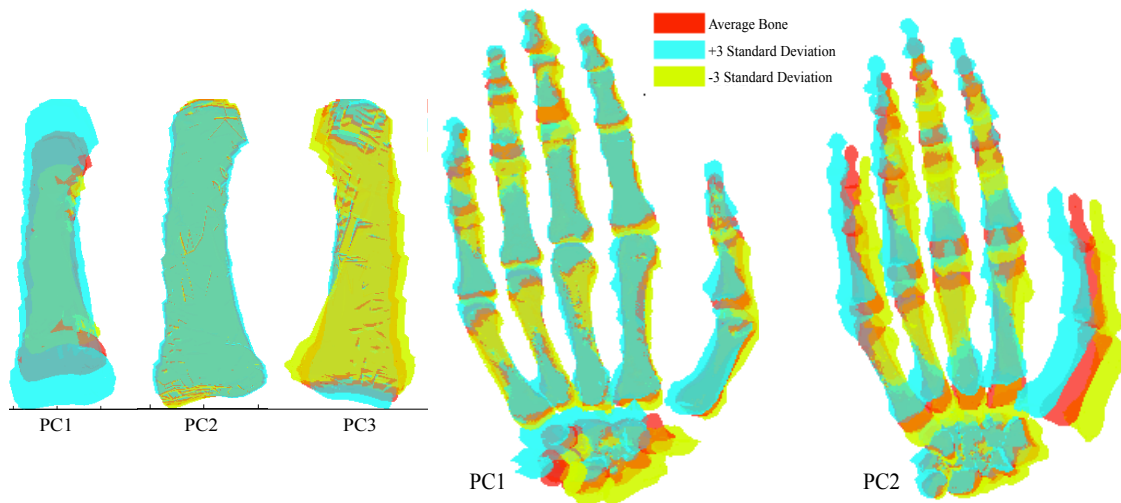
Figure 5.6 Illustration of ±3 SD on the first three principal components for the MP3 bone (left), and the first two principal components for the skeleton of the whole hand (right).

5.3.2.2   Prediction of Surface Geometry of a Whole Hand Skeleton

Analogous to the individual bone surface predictions, PCA was used to describe the geometry of a whole hand skeleton, followed by a regression analysis with the PC scores to predict the hand geometry based on hand length, handbreadth, hand thickness and sex. Table 5.2 includes representative data of the results for the Euclidean Error (MSE), Mean Absolute Error (MEA) and Procrustes Error for evaluating the shape predictions of a whole hand skeleton in 1) common posture and 2) rotated to the scan's original postures, using the CoRs obtained in Chapter 4 for the kinematics.

In addition, measurements corresponding to hand length, breath and thickness, and individual finger's lengths, widths and thicknesses were included in the geometry vector. These reference points representing the skin measurements were included so that their locations in relation with the skeleton can be predicted simultaneously with the bone skeleton predictions. Figure 5.5b illustrates representative data of whole hand predictions in the common posture and after rotating the prediction to match the subject's original posture. The skin surface predictors were included in the common posture predictions (Figure 5.5b) for the purpose of including hand envelope and identifying the factors that can be used by others to accurately place the skeleton model inside measured or predicted skin surfaces.

Analogous to the individual bone analysis, a good way to investigate the correlations would be to decompose the shapes using PCA. This would result in an order basis where each component (PC mode) is ranked after variance (Table 5.4).

Table 5.4 Cumulative percent of variance accounted of principal components in the geometry data

Principal component	Cumulative Percent
1	94%
2	97%
3	98%
4	99%
5	99%

Figure 5.6 illustrates the first two principal modes modifying one component at a time. From Figure 5.6 we can interpret that changes in shape are mainly related to the first PC since the predictions based on this mode include changes in the general shape of the hand and not solely in a specific direction (as was observed for the individual bone predictions).

5.4   Discussion

This study documents for the first time the relationships with bone breadth/thickness along the shaft and potential covariates sex, stature, bone length, hand length, hand breadth and hand thickness. After measuring the total bone areas of five cross-section areas along the shaft, as expected, results show that males have larger total bone areas than females. Although is a positive correlation, such as those observed and expected in relation to hand length and body stature, the analysis suggests that the relationship is not linear and the scaling factor would depend on the cross-section level across the shaft. This differs from the current assumption of symmetry across the segment's breadth/thickness (Alexander & Viktor, 2010; Delp et al., 2007; Dennerlein et al., 1998).   These findings are consistent with previous studies that suggest the same relationship for femur bones (Klein et al., 2015). However, for the femur this relationship was anticipated because lower extremity segments are highly affected by pelvis size

(Klein et al., 2015), observation that has not been made before between wrist and phalanges.

This study provided good predictions for individual bone surface geometries from patient anthropometric data. The mean Euclidean distance results for individual bone predictions were 10 times smaller than the ones reported Klein et al. (2015), and similar to the ones reported by Zhu & Li (2011) for femur geometry predictions. The mean Euclidean distance results were close to those reported by DeVries et al., which are 0.19 (mm), 0.20 (mm), and 0.21 (mm) for the proximal, middle, and distal phalanx, , respectively (DeVries et al., 2008). Bone shape predictions from this study can be useful for analyzing bone fractures and shape density, tendon attachments, and for orthopedic surgical planning, biomechanics research, and 3D-bone shape reconstruction and to build FE models. These individual bone predictions can also be used to fit missing bones to obtain a complete hand skeleton from partial data.

The statistical shape analysis of the individual bones indicated that the DP bones required the fewest number of PC scores to account for 99% of the variance in the data (Table 5.3), indicating that the primary modes of variance in DP shape are similar across subjects. In contrast, the Carpals required twice the number of PC Scores versus the DP segments to account for 99% of the variance in the data, indicating greater idiosyncrasy in bone shape variability. Anatomical differences in the alignment of the carpals could also have reduced the relative importance of the first few PCs. Improvements to the segmentation process of the carpals and separate modeling of each bone could increase accuracy of carpal predictions.

Skeleton shape predictions were compared to the original hands using MSE and MAE results (Table 5.2). The MSE results were similar to the ones reported by Klein et al. (2015). As expected, the MAE results (Table 5.2) were slightly larger for the predictions rotated to match the original postures, since these errors include discrepancies due to kinematics.

5.5   Conclusion

This study presented two statistical shape models: 1) for modeling individual bone geometries and 2) for modeling all bones of the hand at once, using external anthropometric data. The model performance was evaluated using a cross-validation technique.

The whole hand skeleton developed can be used to enhance hand modeling across a range of simulation models. Figure 5.7 illustrated the bone segments predicted, applied to a simple kinematic system that used a contact algorithm developed by Choi, 2008. Additionally, the skin surface reference points predicted based on classic measurements (Garret, 1971) could be use as a baseline for future research so that the whole hand skeleton predictions can be fitted to any hand surface models.
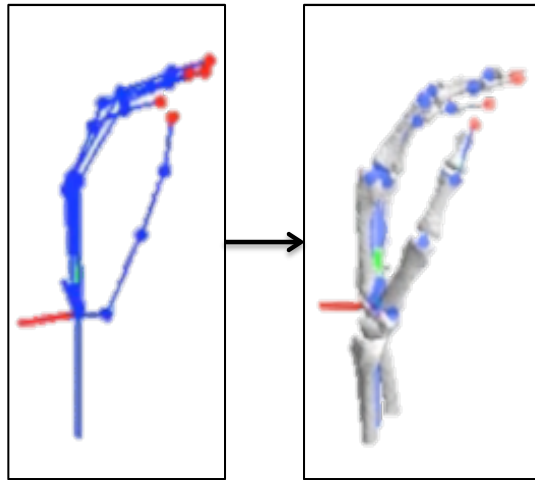
Figure 5.7 Bone shape/size predictions developed in this study can be used for estimating the hand's skeleton based on external anthropometric and for developing kinematic models with these predictions

5.5.1 Limitations and Future Work

This study was limited by the data available. Male and female subjects were not evenly distributed in different age groups. Future studies may consider increasing the sample size and balancing the sex distribution to further improve the model and adding larger number of subjects, particularly improving the range of age represented for both sexes. Consideration should be given to expanding the model to include certain types of pathology, such as osteoarthritis.

This study included fixed CoR locations based on an instantaneous CoR method. Much more data from hands measured in multiple postures are needed to improve the representation of joint kinematics and to assess the relationships between kinematics and the bone geometry. Expanded kinematics data would allow constraints to be added to the model to establish such that the instantaneous CoR could be evaluated as a function of the joint angles.

5.5.2 Acknowledgements

CHAPTER 6 Conclusions

This dissertation developed a skeleton-driven 3-D anthropometric model of the hand that can use to predict hand posture, to estimate hand shape, and to predict bone shapes and sizes. In addition, the relationship between hand surface orientation, posture, and force when pressing a flat surface was examined. This was achieved through the following aims:

1. Determine the relationship between hand surface orientation, posture, and hand force when pressing a flat surface.

2. Generate 3-D hand anatomical representations and the segment coordinate systems based on medical images.

3. Modify four methods to determine centers of rotation for adapting them to finger joints using internal measurements obtained through CT-Scans.

4. Develop a 3-D statistical model of the hand, predicting geometry of bone shape/size and scaling skin to determine hand envelope for any population.

This chapter summarizes the findings and discusses their potential applications for hand modeling.

6.1   Summary of Major Findings and Discussion

Hand posture is important for designing safe tasks, providing enough clearance for the hand, and understanding strength capabilities (Armstrong, Choi & Ahuja, 2008; Sancho-Bru et al. 2006; Chaffin, Andersson & Martin, 2006). Hand posture can be

predicted in two ways: 1) based on biomechanical behaviors per population predetermined empirically as a function of force exerted by the hand, and 2) by modeling possible postures based on the internal structure of the hand. This dissertation aims to push forward the state of the art by increasing the understanding on the variables needed to realistically model a human hand (Figure 6.1).
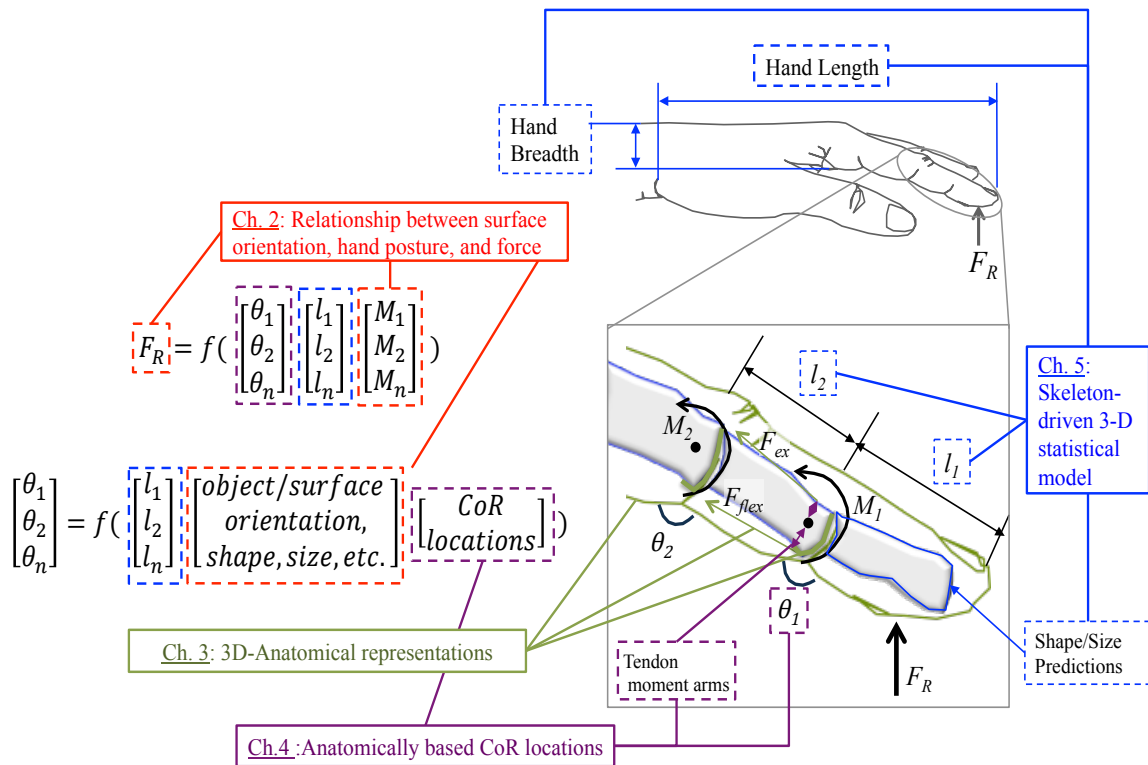
Figure 6.1 Hand force exertions and placement can be modeled by understanding the internal structure and the relationship between the internal and external surfaces. In this dissertation, four studies determined key components needed for a 3-D anthropomorphic hand model.

As shown in Figure 6.1, building a complete understanding in 1) hand posture, 2) internal and 3) external forces, 4) bone geometries, 5) hand shape (externally) and 6) external constraints is imperative for accurately developing an anthropometric model of the hand. Force (F_R) exerted against a surface or object can be described as a function of the joint loads and hand posture. These joint loads (M) are relative to their location based

on the link lengths (l) and angles between segments (θ), and can be deconstructed based on tendon excursions (F_{ex} and F_{flex}) and their relative distance to the center of each joint. The external environment (e.g. obstruction, object properties, task requirements) also plays a major role when determining potential hand placements and angles between the segments (θ) (Armstrong, Choi & Ahuja, 2008; Chaffin, 2008).

The relationship between the external forces, joint loads and hand placement can be empirically analyzed and modeled (Chapter 2), but will be naturally limited by the assumptions of each study. These empirical models can be subsequently leveraged to develop generalized computer hand models to determine hand force, posture (Chapter 4) and shape (Chapter 3), based on different types of external forces, internal factors, (Chapters 3-5) object and task requirements and subject anthropometrics (Chapter 5). The goal of Chapters 3-5 is to leverage existing technology (e.g. widely available medical images, current hand models, current methods never applied to the hand) to provide answers to difficult questions on hand capabilities posed by engineers and designers of aircraft, automobiles, spacecraft, and workplaces. A more precise understanding of hand motion in this context will not only improve fundamental understanding and design in the work environment, but also allow medical providers to track individual patient performance during rehabilitation, thereby increasing treatment effectiveness and improving quality of life.

Over the years, many biomechanical and ergonomic models (based on different parameters) have been developed to attempt to characterize probable hand-object/surface interactions based on task specific assumptions (Miyata et al., 2016, 2005; Armstrong,

Choi & Ahuja, 2008; Buchholz & Armstrong 1992). Previous studies have evaluated subject–specific grip strength capabilities, when fingers work against the thumb or palm (Szychlinska et al., 2017; Zhou et al., 2011; Kargov et al., 2009; Rosenbaum et al., 2009, Seo et al., 2007; Salimi et al. 2003; Blackwell et al., 1999; Fransson and Winkel, 1991; Mathiowetz et al., 1985; Chaffin et al., 1983). However, there is lack of quantitative information describing hand and finger forces when oriented in the same direction. Chapter 2 addresses that gap by providing new data to help characterize the relationship between hand postures, object orientation and force distribution across the palmar side of the hand while pressing a flat surface. The broader research community can leverage this new data by contrasting empirical results to increase the understanding of hand posture and force distribution depending on the type of posture and task requirements.

Chapter 2 showed that subjects exert twice the force if pressing with a flat hand instead of using just the fingertips, indicating that tasks involving push forces should be designed with clearance for the whole hand so the worker can use the whole hand. Overall, the greatest force, 72-75% of total force, was exerted over the base of the palm followed by 11-13% with the thumb when pushing forward (45° and 90°) and downward (0°). The clear preference to exert force over the base of the palm indicates that tasks involving push forces should also be oriented such that the worker can use the base of the palm for maximum effectiveness.

Additionally, results from Chapter 2 showed that thumb/finger forces and moments were consistently lower in magnitude when pushing with the whole hand than with the fingertips (Table 2.3), indicating reduced risk of injury for whole hand tasks. Although it

was not possible to determine which finger joint is limiting, it is reasonable to assume that participants positioned their hands to equalize the relative moments (%MVC) about each joint (An et al. 1984; Bean et al. 1988). Available relative finger strength data for grip and pinch exertions (Barter et al. 1958; Fransson and Winkel 1991; Swanson et al. 1970; Hazelton et al. 1975; Seo et al., 2007) suggests that the third finger is the strongest, accounting for approximately 33% of the total force exerted by the sum of all fingers. However, in contrast from gripping tasks, this study found that while pressing with a flat hand the distribution of force among the fingers varies depending on the orientation of the surface (Table 2.3). These results indicate that tasks involving push forces should be oriented in a position that enables the worker to leverage finger strength, and perhaps to minimize it by adding enough clearance to use the base of the palm.

Chapter 2 also showed that substantially more force is exerted in a direction away from the body at elbow height (Tables 2.2 and 2.3) compared with pushing towards the body (-45°). When pushing forward (45° and 90°) and downward (0°), participants tend to align the force vector along the shoulder by extending or flexing their elbows, and increasing torso flexion. These pushing postures are congruent with findings reported by Granata et al. (2005) and De Looze et al. (2000) during pushing experiment while holding a handle. Perhaps, as noted by Hoffman et al. (2007), the strategy during flexed–elbow push exertion is to direct the hand force vector along the spine and/or the shoulder, which would imply that tasks involving push forces should be oriented to enable the worker to align the force vector with the shoulder. Further analysis is required to test this hypothesis.

Lastly, results obtained Chapter 2 can help to understand and predict hand postures and finger loads from object orientation and force required. Data obtained in this study can be used to design work tasks that might be subjected to high hand force while holding or positioning an object such as installing panels in auto assembly lines, holding objects against a flat surface, or supporting their body while performing a task. Joint moment data and finger force distributions from this study can be incorporated in hand 3D-models and in computerized manikins (e.g. Jack) for accurate posture predictions during ergonomic assessments.

The focus of Chapters 3-5, is to develop a three dimensional (3D) anthropometric hand models that can be used to study hand postures and forces which affect force exertions while grasping objects, supporting their body and/or interacting with surfaces. Despite the advances already made in human hand modeling (Armstrong, Choi and Ahuja, 2008, Miyata et al., 2006; Kurihara et. al 2004), prior work has represented finger segments with simplified geometries, including ellipsoids (Buchholz and Armstrong 1991, 1992) and truncated cones (Armstrong & Choi, 2008). Other prior work has based kinematics joint centers and/or calibrations on vision-based methods (e.g. 3D markers) (Cerveri et al., 2005; Kurihara & Miyata, 2004). Although these assumptions can provide good posture and hand envelope predictions, these models could not be used for accurate clinical applications such as surgical planning and navigation, or anatomical studies anatomical, due to low accuracy. Results can be significantly improved by building realistic representations of bone geometry to determine the kinematics. To realistically simulate hand posture and its interaction with external surfaces and objects, precise reconstruction of hand segments is required (Lien 2005; Kurihara & Miyata, 2004).

Today, high-resolution CT-scan imaging allows researchers to obtain accurate joint data in a short period of time. Accuracy is necessary to provide proper diagnosis, but it is also a prerequisite to generate valid surface models from which kinematics parameters are derived. In this dissertation, a skeleton-driven hand model was developed using novel methods while leveraging existing data and technologies, including available medical images, current hand models and statistical bone shape models developed for other parts of the body.

In Chapter 3, 3D meshes were developed for skin surface and bone segments of the hand based on a single hand in five different postures obtained through CT scans. Then, a quantitative method to establish local and global coordinate systems with hand and upper arm bones was developed, such that it could be applied to any hand after bone segmentation. ISB recommendations on definitions of joint coordinate systems (Wu et al., 2005) were adapted for hand modeling, accounting for the potential lack of availability of the proximal end of the radius from patient hand CT scans. Although Wu et al. (2005) provides good guidelines for defining coordinate systems for hand bone segments, it lacks quantitative specificity. A quantitative protocol, to establish local and global coordinate systems, was developed for hand segments to strengthen these guidelines (Wu et al., 2005).

This study used a combination of Procrustes Analysis (Gower, 1975) and ICP algorthm (Besl & McKay, 1992) to achieve a landmark-free approach to symmetrically superimpose two 3D segments, with the purpose of evaluating the 3D geometries and their coordinate systems. Results from Chapter 3 show that the CT image manual

segmentation method obtained hand surfaces with minimum variability between operators. The variability was measured by comparing 3D surfaces that were manually segmented by six different operators. The shape difference, defined by mean Euclidean distance, was less than 0.2 (mm), validating the protocol developed in this study. Furthermore, results from Chapter 3 show that manual segmentation of high-contrast CT datasets accurately represents the true surface geometry of bones. In this study, one operator segmented all surfaces (skin and bones of the hand, wrist and upper arm) of the five hand-CT images of the same subject. 3D shapes of all finger segments were compared based on the mean Euclidean distance. The mean Euclidean distance results were considerably less than the ones reported in other bone shape comparison studies (Klein et al., 2015; DeVries et al., 2008), indicating an improved protocol compared with prior studies. This study also showed that the methods to establish a local coordinate system for each bone are similarly reliable to those reported by Kamojima & Miyata (2004), proven by comparing the translation and rotation errors between the two studies.

The 3D bone geometries and their corresponding coordinate systems, developed in Chapter 3, were leveraged in Chapter 4 to adapt four methods to determine Centers of Rotations (CoR) in hand joints. These four methods were: 1) Sphere Fitting, 2) Ellipsoid Fitting, 3) 3D-Reuleaux, and 3) Axes of Rotation (AoR) through Iterative Closest Point Algorithm (ICP). Sphere- and Ellipsoid-fitting CoRs were considered fixed CoRs, with a fixed rotational axis based on simple links representing each segment. Reuleaux- and ICP-based CoRs were considered instantaneous, with variable link lengths identified by the rotation and the gliding action (translation) at the joints. Instantaneous CoRs consider the anatomical structure of the bones when determining the location of the instant centers,

making them not only significantly different than the fixed CoR methods (Table 4.5) but also more robust and accurate, which is critical particularly for clinical and therapeutic applications, and for accurate analysis on tendon loads around the joints Under the pin joint assumption of the fixed CoR methods, irregularities of bone shape along the joints are not considered so physically unrealistic postures could be acquired with these methods.

Instantaneous CoRs enable higher accuracy for several hand model outputs, as structural bone geometries of adjacent segments affect finger joint angles, locations of tendon attachments (tendon moment arms), tendon movements and forces, and geometric locations of the extrinsic and intrinsic tendons. Thus, kinematic models of the hand can be improved by determining the postures based on structural bone geometries. These models can be subsequently used to estimate tendon excursions to reduce risks of upper extremity musculoskeletal disorders (Schweizer et al, 2003; Armstrong et al., 1987).

Lastly, in Chapter 4 landmark-free statistical models were developed from clinical CT scans of 29 male and 14 female hands, validating the approaches discussed in Chapter 3 across a broad set of different hands. Protocols developed in Chapter 3 were used to segment clinical CT data and to establish the coordinate systems for the 3D surfaces. The 3D-bone surface geometries of the template hand from in Chapter 3 were then used to create homologous surfaces to represent each hand. Additionally, kinematics developed in Chapter 4 were used to rotate finger segments of fitted hands for 1) obtaining hand skin measurements in a common posture, 2) performing whole hand skeleton predictions, and 3) evaluating final predictions in the original postures.

The LMM analysis on the cross-sectional areas along the finger bone shafts provides new insight by establishing a relationship between bone breadth/thickness along the shaft and sex, height, bone length, hand length, handbreadth and hand thickness, (Figure 5.4). After measuring the total bone areas of five cross-section areas along the shaft, results show that males have larger total bone areas than females. Although is a positive correlation between those observed and expected in relation to hand length and body stature (Figure 5.4d), the analysis suggests that the relationship is not linear and the scaling factor would depend on the cross-section level across the shaft. This differs from assumptions in previous studies, where phalanges are assumed to be symmetric across breadth dimensions (Alexander & Viktor, 2010; Delp et al., 2007; Dennerlein et al., 1998). With the methods outlined in Chapter 4, underlying skeletal critical dimensions from bone geometry can be used to develop factors to predict bone shapes and sizes, with the purpose of accurately determining locations of anatomical joint centers, tendon attachments, hand envelope, and ultimately to predict hand placement. Results from this study suggest that models should take into account sex differences, especially along the dimensions related to breadth and thickness, to ensure accurate 3D kinematics.

In Chapter 4, two types of landmark-free statistical shape models were developed: 1) model for bone surface geometries of individual finger segments, and 2) model for all bones of the hand at once. In this study, the model's building methodology and its posture and hand envelope predictions were examined quantitatively and qualitatively. Multivariate statistical analyses (based on PCA) were used to establish shape variations in hand bone surface geometries and skin measurements with respect to hand length, handbreadth, hand thickness and sex. The statistical models for both individual bones and

114

for the whole hand skeleton included subject-specific information such as age, sex, stature, weight, race, hand length, hand breadth and hand thickness, increasing the accuracy of scaling capabilities of current models (Appendix F). The statistical model for the whole hand skeleton model also included hand and individual finger lengths, widths and thicknesses, and average position of CoR on each distal head of the proximal bones, based on ICP (from Chapter 4).

Based on the Mean Euclidean Distance results and their relation to the errors reported in literature (Klein et al., 2015; Devries et al., 2008; Miyata & Ota, 2004), this study shows favorable results in predictions of shape/size of the whole hand skeleton and scaling of hand skin surface. The shape predictions of the hand bones developed in Chapter 5, in conjunction with the reference points located around the skin surface, can be used as a baseline for any hand surface models to establish kinematics based on internal bone segments, thus bringing more efficacy and accuracy to hand modeling field.

The landmark-less shape/size prediction models for bones, skeleton and skin surface developed in Chapter 5 enable rapid model fitting with much lower data requirements than prior models. Additionally, this was the first time statistical bone shape modeling of the hand was undertaken using bone geometry for kinematics, allowing simple generalization to any population.

Methods discussed in Chapters 3-5 can be applied in broader geometry modeling, both for hand posture and shape prediction models, to morph biomechanical models of the hand in virtual reality. These methods are also highly relevant across medical fields to perform anatomical studies and diagnosis, plan surgeries, and build training and

navigation tools to improve understanding and communication across the wider medical and patient communities (Figueroa et al., 2014; Jan et al., 1997). Benefit goes beyond just providers, as payers could increasingly require proof of outcome to trigger payment as the share of value-based care continues to grow due to an increase in objective and accurate evaluation for simulating various outcomes. The whole hand prediction model, however, can be used for better hand shape predictions in medical and other domains. For example, there is a current need in the Army for creating and testing gloves, both virtually and physically. They tests gloves for fire protection using rigid, fixed-size hand physical models. As the air gap inside the gloves has a big effect on heat conduction, having more-realistic models would improve their predictions for hand glove design and sizing.

This dissertation builds into the broader set of research related to hand placement. The different studies performed develop many areas of study (Figure 6.2) related to hand modeling beyond the current state-of-the-art, aiming to understand and model hand force, posture, and shape based on different types of external forces, internal factors, object and task requirements, and subject anthropometrics.
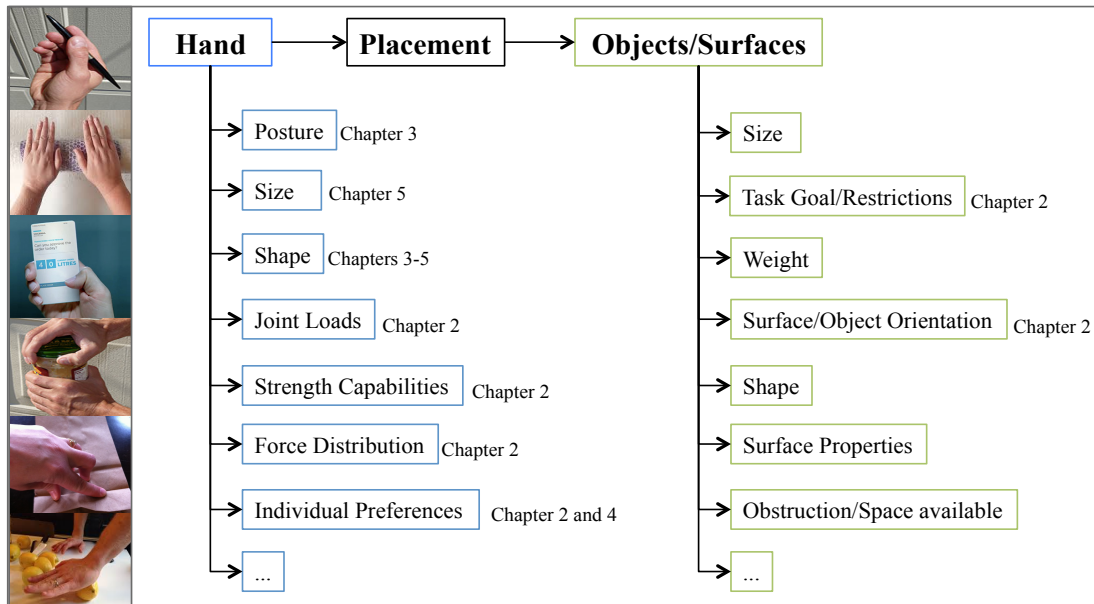
Figure 6.2 Information needed to accurately depict hand placement on an object or surface.

Thus, the overall aim of this dissertation was achieved with the development of bone and skin 3D-models with coordinate systems based on ISB recommendations (Chapter 3) and joint centers based on bone geometry (Chapter 4). Additionally, these models can represent specific groups with the shape/size predictions of skeleton and individual surfaces from this dissertation (Chapter 5). The developed models can be incorporated into current posture prediction models (e.g. Choi, 2008- Figure 6.3) for establishing realistic representations and hand kinematics (Figure 6.4).
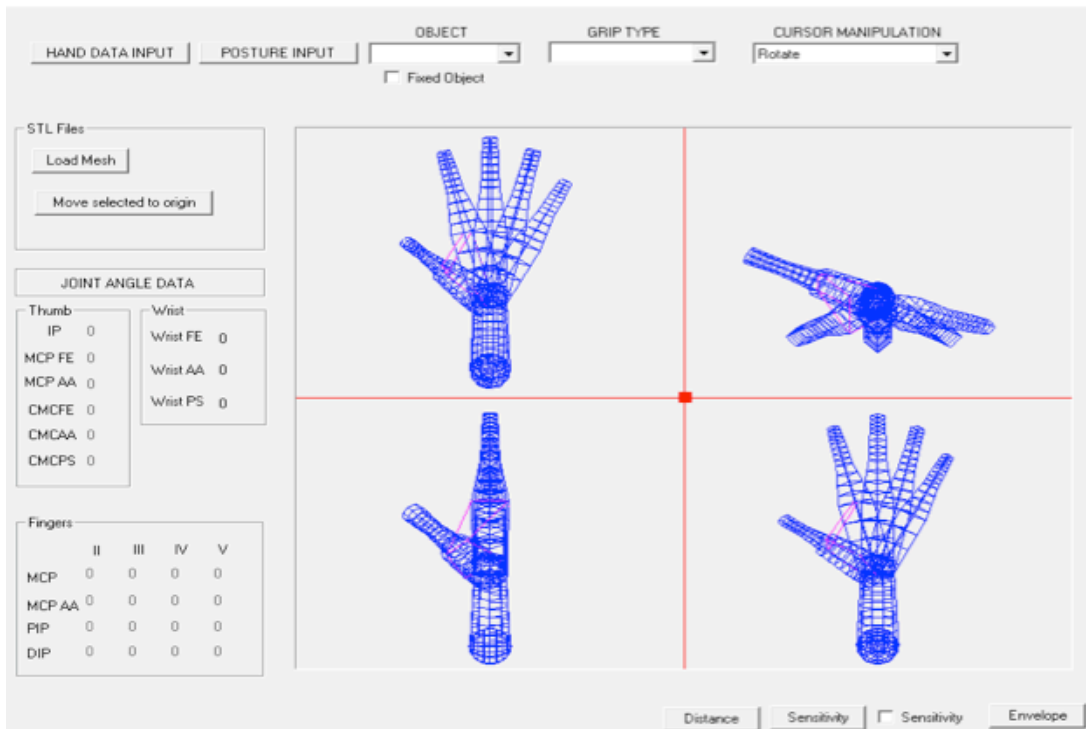
Figure 6.3 Screenshot of hand posture prediction model developed by Choi, 2008 at the Center for Ergonomics at the university of Michigan.
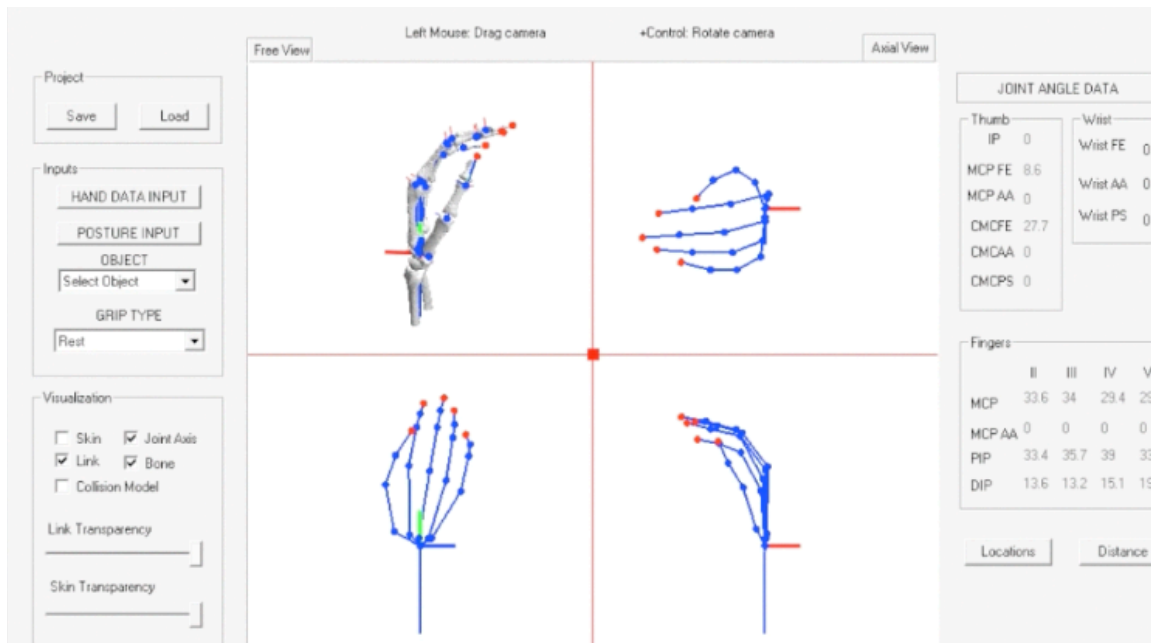
Figure 6.4 Models developed in this dissertation were incorporated in the kinematic model developed by Choi, 2008.

These models can be used to establish the kinematics and constraints to realistically rotate one bone segment around the other (Figure 6.5).
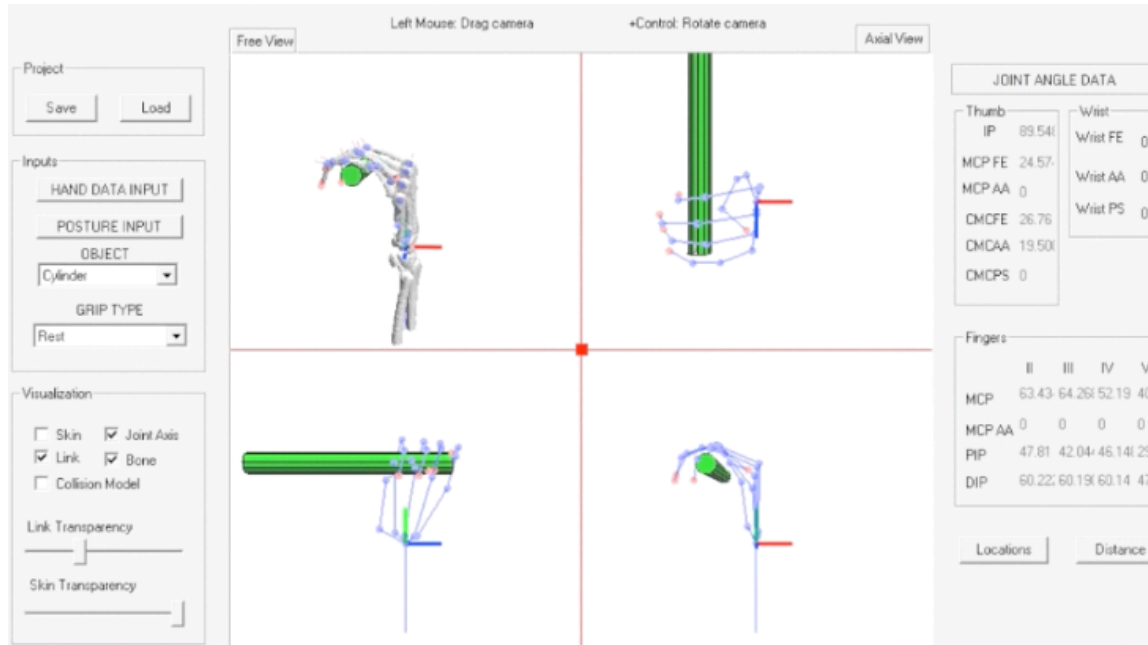
Figure 6.5 Joint centers obtained from the ICP method and constraints based on the minimum joint distance required and the anatomical joint geometries were used to enhance current kinematics of the model originally developed by Choi, 2008.

6.2   Suggestions for Future Research

While the model proposed in this dissertation can be used to predict hand postures and envelope, as well as bone shapes and sizes, further work is needed to improve the capability of the model predictions and to expand the model's applicability. Therefore, the following suggestions are proposed for future studies:

- The study presented in Chapter 2 only examined the normal force component due to the limitation of the pressure mapping system. However, object orientation could result in significant friction forces and affect the magnitude of the resultant force. The influence of friction on

hand force distribution and hand placement while pushing a flat surface needs further investigation. Previous studies have found that object/hand interaction (Frederick and Armstrong 1995) and shoe/floor interactions (Fischer, et al., 2013; Granata et al., 2005) affect push/pull forces while grasping a handle. This study found that fingers were not the limiting factor for maximum forces exerted when pushing perpendicular to a flat surface with a flat hand. Based on the upper body postures observed in this study, the strategy during flexed–elbow push exertion was to direct the hand force vector along the spine and/or the shoulder. Further analysis is required to test if maximum whole hand force exerted perpendicular to a flat surface is limited by shoulder, whole body strength or traction. External support for the body, so that foot friction is not limiting, could be used for this test.

- Symmetric superimposition in methods such as ICP is very dependent on the initial positions of the surfaces relative to one another (Shi et al., 2014). Although in Chapter 3 an automated process was used for alignment and superimposition, the last step was a manual visual inspection of the aligned surfaces. This was done to further evaluate the alignment process to ensure no reflection along axes (e.g. aligning distal end of template with proximal end of targeter posture). If this method was adapted for analyzing numerous subjects, the manual visual inspection could be eliminated by automatically assigning pseudo-landmarks (Shi et al., 2014), using Wu et al. (2005) recommendations as a baseline, after

simplifying the 3D segments to avoid axis reflection when using ICP for symmetric superimposition. Alternatively, alignment methods, such as RBF for morphing as explained in Chapter 4 for 3D- Reuleaux and in Chapter 5 for fitting the template to all targets, can be used for creating homologous meshes for a pair-wise comparison.

- Chapter 4 was limited by the existing hand CT images that were donated for this study. These images were in pre-determined postures based on common grasping postures (e.g. power grip, pinch grip) rather than standardized posture with controlled changes in joint angles. Future work should include further analyzing CoR locations based on joint angle so that a more accurate model can be developed. It would also be beneficial to gather data from several subjects in more standardized postures to maximize the joint angle analysis, which would enable an evaluation of size variation and sex effects on the accuracy of the methods discussed in this dissertation. Standardized postures could include a flat hand, a resting hand, and grasping of spheres/balls (Table 6.1, Figure 6.6) or cylinders (Miyata et al., 2007). As Table 6.1 shows, joint angles vary significantly in such postures and further exploration of them would be beneficial in creating a model on how to predict the location of the CoR based as a function of the joint angle.

Table 6.1 Joint angles of the index finger, of a 47.2 percentile male, for 5 different poses.

Posture	MCP	PIP	DIP
a) Flat Hand	178°	179°	177°
b) Resting Hand	138°	144°	151°
c) Large sphere (11 mm)	155°	140°	148°
d) Medium sphere (8 mm)	145°	133°	155°
e) Small sphere (5 mm)	128°	75°	135°
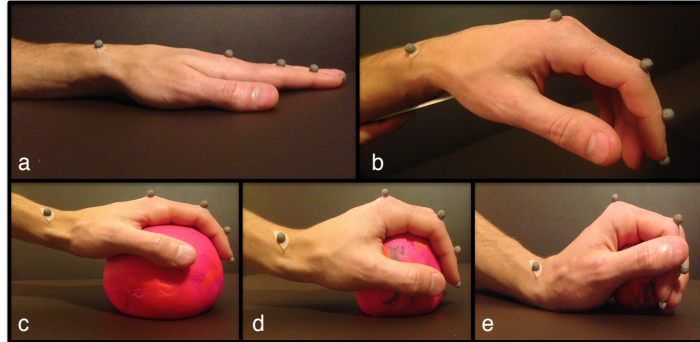
Figure 6.6 A hand from a 47.2 percentile male in 5 different poses: a) Flat hand, b) resting hand, c) large sphere, d) medium sphere and e) small sphere.

Additionally, based on the paired t-test it cannot be established that a significant difference exists between Reuleaux- and ICP-based CoR positions. However, the p-value approached the borderline of significance and it should be further investigated with more standardize data, as explained above.

- In Chapter 5, landmark-free statistical models were developed for predicting bone shape and sizes. Although the whole hand predictions included measurements predictions for the skin surface as a function of the whole hand skeleton deformation, it did not include a full prediction of the skin surface. The whole hand skeleton predictions can be used as a baseline for creating a framework to incorporate our skeleton-driven model with existing soft tissue models. Other investigators have been

working with finite element analysis and algorithms to model skin deformation (Mohr, 2003). Alternatively, the whole hand skeleton could be fitted to detailed hand surface data that could be obtained non-invasively through depth cameras (e.g. Microsoft Kinect [TM]). Integrating detailed hand surface data to the skeleton modeled in this study would increase be beneficial for the analysis of friction, skin deformation and soft tissue analyses.

APPENDICES

APPENDIX A
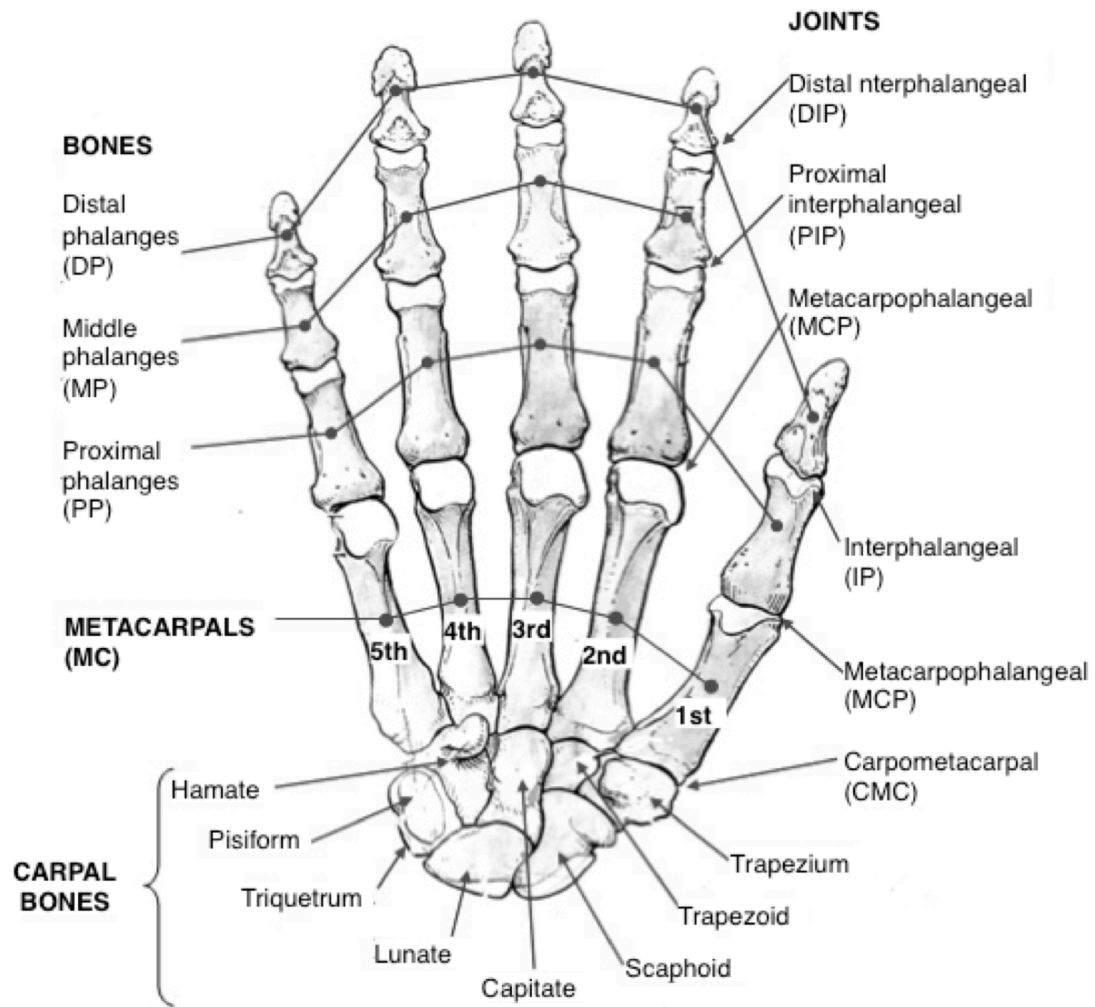
Figure A.1 Bones and joints of the hand with their corresponding acronyms. The fingers and phalanges are numbered starting from the thumb (finger 1) to little finger (finger 5)

APPENDIX B : Details on Principal Component Analysis, used to determine the preliminary axes of each metacarpal and phalanx.

The preliminary axes of each bone were identified using PCA after determining the empirical covariance matrix of each triangulated surface *i* (Bredbenner et al., 2010; Zhu & Li, 2011).

$$S = \frac{1}{m_i - 1} \sum_{j=1}^{m_i} (p_{ij} - \bar{p_\iota})(p_{ij} - \bar{p_\iota})^T \text{ with } p_{ij} = (x_{i,1}, y_{i,1}, z_{i,1}, \dots x_{i,m}, y_{i,m}, z_{i,m})$$

$$\bar{p_\iota} = \frac{1}{m_i} \sum_{j=1}^{m_i} p_{ij}, \quad j = 1:m$$

(1)

Where m_i is the number of vertices of each bone surface *i*, and $\bar{p_\iota}$ is the centroid of the 3D-mesh. Then, the eigenstructure of the covariance matrix **S** was computed to identify the principal components

$$S\,U = U \wedge, \quad \wedge = |S - \lambda \cdot I|$$

(2)

where $\wedge$ is the diagonal matrix with the corresponding eigenvalues (λ_k, k = number of eigenvectors) and **U** is a 3x3 matrix with unit length eigenvectors (***PC**_k*, k = number of eigenvectors) as its columns (Reyes et al., 2007). The first three eigenvalues (λ_k) and

eigenvectors (PC_k) characterize the vertices along the 3 principal preliminary axes, **Y'**, **Z'** and **X'**, spanning a shape space centered at the mean.

$$\Lambda = (\lambda_1, \lambda_2, \lambda_3), \lambda_1 \geq \lambda_2 \geq \lambda_3 \geq 0$$

$$U = (PC1, PC2, PC3)$$

(3)

APPENDIX C : Summary of steps performed for Procrustes alignment, proposed by Gower (1975), and the Iterative Closest Point (ICP) algorithm, used to superimpose and align shapes and to calculate shape differences

1. Pair each vertex/point of 3D-mesh $g_{A,i,j}$ with vertices $p_{A,i,j}$ to the closest point of a similar 3D-mesh $g_{B,i}$ with vertices $p_{B,i,j}$; were j range from 1 to m (*m*= number of vertices in the triangulated surface) without duplicates.

2. Compute the transformation (rotation and translation) to minimize a cost function between the paired points and record the error based on the Procrustes Analysis.

$$Min\ C_A = \sum_{j=1}^{m_i} \| p_{A,i,j} - (H\ p_{B,i,j} - t) \|^2$$

(1)

Where C_A is the cost function for a basic point-to-point ICP algorithm, $p_{A,i,j}$ and $p_{B,i,j}$ are a point on surface A (template) and its nearest neighbor on surface B (posture 1-4), i range from *1* to n (*n*=19 corresponding to the number of finger segments modeled), j ranges from 1 to m (m equals to the number of points on surface A (template), H and t are rotation and translation terms and k is the error iteration.

3. Apply the optimal transformation to 3D-mesh A and update error between A and B based on Procrustes alignment (Hill et al., 2001; Goodall, 1991; Gower 1975). Error for the first iteration was defined as the sum of the magnitudes of the

Euclidean distances between each vertex of template $g_{A,i}$ and each target posture $g_{B,i}$.

$$Error_1 = \sqrt{\sum_{j=1}^{m}(g_{A,i} - g_{B,i})^2}$$

(2)

4. Repeat steps 1-3 are repeated until the distance between surfaces cannot be reduced through additional iteration based on equation 8.

$$Error_{k-1} - Error_k < 0.000001 \; mm$$

(3)

In addition to calculating Procrustes error to evaluate the difference between segments, the final mean Euclidean distances were recorded for each shape comparison.

$$d = \frac{1}{m}\sqrt{\sum_{j=1}^{m}(g_{A,j} - g_{B,j})^2}$$

(4)

APPENDIX D : Rotation differences between axes or two 3D meshes

Rotation error, defined for the same axis between two 3D meshes (Kamojima et al., 2004). Where a_i, b_i represent the local axes in X, Y and Z directions of template bone $g_{A,j}$ and target bone $g_{B,j}$, respectively, and i is the bone aligned.

$$a_i = \begin{bmatrix} X_A \\ Y_A \\ Z_A \end{bmatrix} = \begin{bmatrix} X_{A,x} & X_{A,y} & X_{A,z} \\ Y_{A,x} & Y_{A,y} & Y_{A,z} \\ Z_{A,x} & Z_{A,y} & Z_{A,z} \end{bmatrix} \quad b_i = \begin{bmatrix} X_B \\ Y_B \\ Z_B \end{bmatrix} = \begin{bmatrix} X_{B,x} & X_{B,y} & X_{B,z} \\ Y_{B,x} & Y_{B,y} & Y_{B,z} \\ Z_{B,x} & Z_{B,y} & Z_{B,z} \end{bmatrix}$$

(1)

The angles between a_i and b_i were defined as α, and β and γ for the x-axes, y-axes and z-axes, respectively. The average rotation error (*Average Var$_\theta$*) per axis per bone is represented in Equation 3.

$$\alpha = arcos\left(\frac{\vec{X_B} \cdot \vec{X_A}}{|\vec{X_B}| \cdot |\vec{X_A}|}\right) \quad \beta = arcos\left(\frac{\vec{Y_B} \cdot \vec{Y_A}}{|\vec{Y_B}| \cdot |\vec{Y_A}|}\right) \quad \gamma = arcos\left(\frac{\vec{Z_B} \cdot \vec{Z_A}}{|\vec{Z_B}| \cdot |\vec{Z_A}|}\right)$$

(2)

$$\text{Average Var}_\Theta = \frac{\sum_{i=1}^{4} \text{Var}_{\Theta,i}}{4} \begin{bmatrix} \alpha \\ \beta \\ \gamma \end{bmatrix} = \begin{bmatrix} (\sum_{i=1}^{4} \alpha_i)/4 \\ (\sum_{i=1}^{4} \beta_i)/4 \\ (\sum_{i=1}^{4} \gamma_i)/4 \end{bmatrix}$$

(3)

APPENDIX E
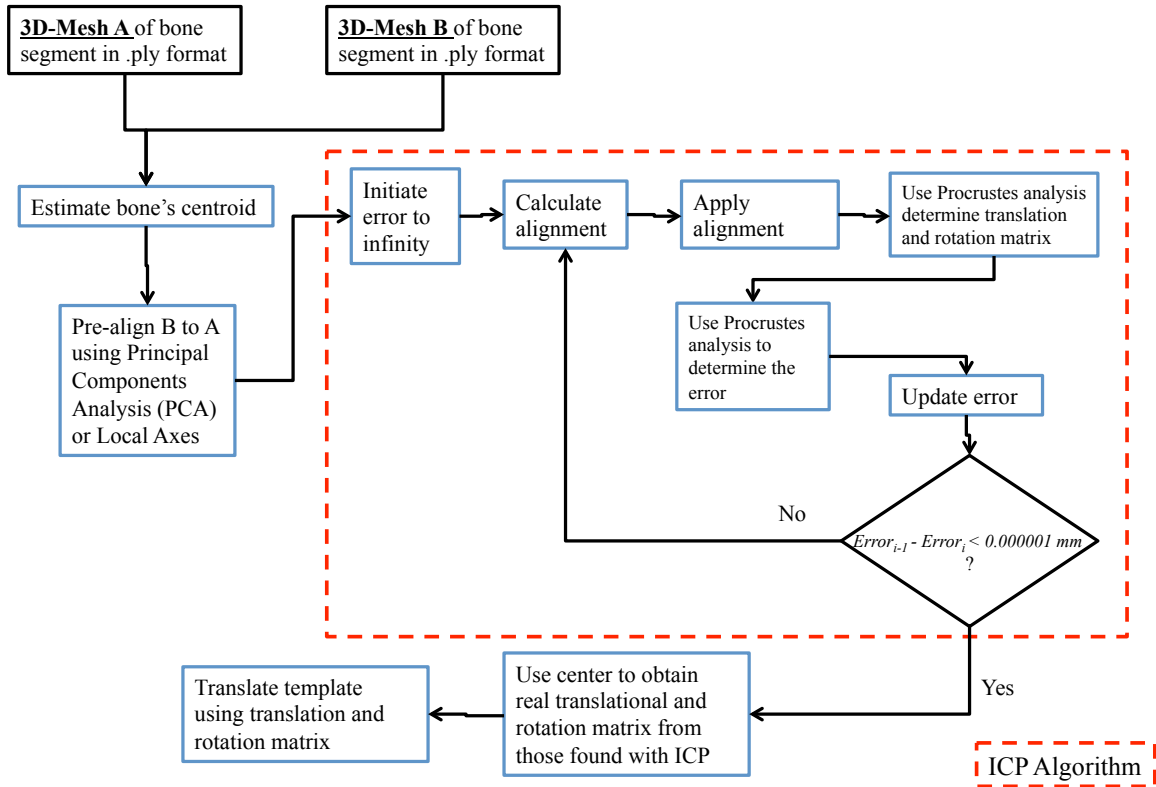
Figure A.2 Flowchart demonstrating the utilization of the ICP algorithm and Procrustes to superimpose two bone surfaces.

APPENDIX F

Table A.1 Subjects' anthropometric data from medical records and hand measurements from skin surface

ID	Age	Sex	Height (cm)	Weight (kg)	Ethnicity	Race	Hand length (mm)	Hand Breadth (mm)	Hand Thickness (mm)
0	41	M	185	70	Not Hispanic nor Latino	White	195	86	27
8	53.9	M	167.6	83.7	Not Hispanic nor Latino	White	182.7	89.5	36.9
10	45.2	M	172	79	Not Hispanic nor Latino	White	209	88.3	37.7
13	53.6	F	170.2	90.3	Not Hispanic nor Latino	White	173.6	80.3	28.5
16	79	M	180.3	81.4	Not Hispanic nor Latino	White	201.4	97.1	40.6
17	47	M	177.8	102.9	Not Hispanic nor Latino	Black African American	194.5	88.7	32.1
19	30	M	177.8	63.5	Not Hispanic nor Latino	White	186.7	84.5	32.4
20	41	M	170.2	71.5	Not Hispanic nor Latino	White	182.3	91.8	48.2
24	37	M	172.7	90.2	Not Hispanic nor Latino	White	190.8	86.6	30.2
26	31	M	172	63	Not Hispanic nor Latino	White	186.9	85.7	38.6
30	63.1	F	157.5	105.2	Not Hispanic nor Latino	White	161.9	77.3	30.4
33	62.8	F	149.9	77	Not Hispanic nor Latino	White	176.5	92	32.1
35	58.6	F	156.2	41.7	Not Hispanic nor Latino	White	172.5	73.9	26.3
36	71.3	M	177.8	63.2	Not Hispanic nor Latino	White	197.3	89.9	24.6
39	66	F	165.9	85.1	Not Hispanic nor Latino	White	193.3	91.4	33.2
41	49	F	160	107.6	Not Hispanic nor Latino	White	178	81.4	29.1
42	45	M	172.7	72.6	Not Hispanic nor Latino	Asian	194.4	88.8	32
44	24.8	M	167.6	75.7	Not Hispanic nor Latino	White	190.1	87.8	35
45	64.5	M	180.3	94.2	Not Hispanic nor Latino	White	200	90	42.7
47	48.7	M	179.1	68.9	Not Hispanic nor Latino	Asian	201.3	86.9	36.2
49	28.9	F	162.6	64.2	Not Hispanic nor Latino	Black African American	179.2	77.9	27.4
50	36.2	F	161	103.6	Not Hispanic	White	177.2	80.3	28.4

						nor Latino				
52	44.4	M	172.7	64.5	Not Hispanic nor Latino	Black African American	199.9	85.6	55.1
53	40.9	M	180.3	78.9	Not Hispanic nor Latino	Hispanic or Latino	189.8	92.8	31.8
57	50.6	M	180	110.2	Not Hispanic nor Latino	White	194	92.3	37.5
60	50.6	F	157	56.7	Not Hispanic nor Latino	White	177.6	78.7	27.6
65	39.9	M	167	71.5	Not Hispanic nor Latino	White	178.1	81.3	32.5
66	40.1	M	172	79	Not Hispanic nor Latino	Black African American	209.9	94	39.2
71	25.9	M	172	79	Not Hispanic nor Latino	Others	188.5	79	31.5
72	21.3	F	162.6	69.5	Not Hispanic nor Latino	White	179.9	87.2	28.9
76	21.3	M	180.3	87.5	Not Hispanic nor Latino	Others	199.3	87.2	36.8
77	25.3	M	190.5	96.5	Not Hispanic nor Latino	White	195.9	91.1	33.6
79	26.9	M	185.4	74.2	Not Hispanic nor Latino	Others	177.4	83.6	30.1
81	20.8	M	170.2	65.8	Not Hispanic nor Latino	White	145.2	80.7	39.8
82	30.2	F	153.7	65.3	Not Hispanic nor Latino	White	168	77.3	26
83	43.9	M	172	79	Not Hispanic nor Latino	White	195.4	88.8	32.6
84	68.7	F	167.6	84.4	Not Hispanic nor Latino	White	192.9	87	33.8
85	29.9	M	188	112.4	Not Hispanic nor Latino	White	203.1	94	32.8
86	19.9	F	161.3	68	Not Hispanic nor Latino	White	176.8	81.8	33.5
90	23.3	F	167.6	67.2	Not Hispanic nor Latino	White	176.2	77.6	26.6
96	34.3	M	167.6	77.1	Not Hispanic nor Latino	Black African American	187.1	82.2	36.6
99	33.4	M	185.4	81.6	Not Hispanic nor Latino	Black African American	205.4	91.7	45
103	26.2	M	182.9	92.1	Not Hispanic nor Latino	Hispanic or Latino	186.9	87.3	36.7

Table A.2 Cumulative variance per individual bone from PCA that can be used to select the number of PC Scores to be used in the modes

Principle component	DP1	DP2	DP3	DP4	DP5	MC1	MC2	MC3	MC4	MC5	MP2	MP3	MP4	MP5	PP1	PP2	PP3	PP4	PP5	CAR
1	58.6	62.0	55.9	48.8	48.3	46.7	62.8	69.9	68.7	59.5	58.9	59.4	60.5	60.5	47.1	53.7	58.9	61.2	53.8	68.0
2	75.4	73.9	68.4	64.6	65.0	69.0	73.4	79.7	78.2	70.3	75.1	73.7	72.4	72.1	77.2	76.9	74.9	74.9	68.6	74.8
3	83.9	83.5	79.9	77.0	76.8	78.9	80.8	84.6	82.9	76.9	83.5	82.1	81.7	82.2	83.4	83.0	81.5	81.9	77.7	79.6
4	91.6	91.9	87.7	86.3	87.1	83.7	85.0	87.8	85.9	80.7	91.4	90.2	88.9	89.3	88.4	89.0	87.3	87.6	85.3	82.4
5	93.9	93.8	91.0	90.9	91.6	86.8	87.5	90.0	88.6	84.4	93.8	92.8	91.4	92.3	92.1	91.8	90.3	91.2	89.0	84.5
6	95.6	95.4	93.7	93.5	94.1	89.0	89.4	91.6	90.7	87.1	95.2	94.2	93.4	94.3	94.1	93.8	92.4	92.9	91.4	86.2
7	96.7	96.8	95.3	95.2	95.8	90.9	91.1	92.8	92.6	89.1	96.4	95.4	94.9	95.8	95.3	95.0	94.0	94.3	93.1	87.5
8	97.6	97.8	96.7	96.7	97.3	92.3	92.3	93.7	93.8	91.0	97.1	96.4	96.1	96.8	96.3	96.0	95.2	95.4	94.6	88.7
9	98.2	98.4	97.8	97.8	98.2	93.4	93.5	94.6	94.9	92.5	97.6	97.2	96.8	97.7	97.0	96.8	96.2	96.1	95.8	89.7
10	98.7	98.8	98.3	98.4	98.8	94.3	94.3	95.2	95.6	93.5	98.1	97.9	97.4	98.2	97.4	97.4	97.0	96.7	96.5	90.6
11	98.9	99.1	98.6	98.9	99.0	95.0	95.0	95.7	96.2	94.4	98.4	98.3	97.8	98.6	97.8	97.8	97.7	97.3	97.0	91.5
12	99.1	0.0	98.8	99.1	0.0	95.6	95.6	96.2	96.7	95.1	98.7	98.6	98.3	98.8	98.1	98.1	98.2	97.7	97.5	92.3
13	0.0	0.0	99.0	0.0	0.0	96.1	96.1	96.7	97.1	95.6	98.9	98.9	98.6	99.0	98.4	98.4	98.4	98.0	97.9	93.0
14	0.0	0.0	0.0	0.0	0.0	96.5	96.6	97.1	97.5	96.2	99.1	99.1	98.8	99.1	98.6	98.6	98.6	98.3	98.2	93.6
15	0.0	0.0	0.0	0.0	0.0	96.9	96.9	97.5	97.8	96.6	0.0	0.0	99.0	0.0	98.7	98.8	98.8	98.6	98.4	94.1
16	0.0	0.0	0.0	0.0	0.0	96.9	96.9	97.8	98.0	97.1	0.0	0.0	99.1	0.0	98.8	98.9	98.9	98.7	98.6	94.6
17	0.0	0.0	0.0	0.0	0.0	97.2	97.2	98.0	98.2	97.4	0.0	0.0	0.0	0.0	99.0	99.1	99.1	98.9	98.8	95.1
18	0.0	0.0	0.0	0.0	0.0	97.5	97.4	98.2	98.4	97.7	0.0	0.0	0.0	0.0	99.1	0.0	0.0	99.0	98.9	95.5
19	0.0	0.0	0.0	0.0	0.0	97.8	97.7	98.4	98.6	98.0	0.0	0.0	0.0	0.0	0.0	0.0	0.0	99.1	99.0	95.9
20	0.0	0.0	0.0	0.0	0.0	98.0	97.9	98.5	98.7	98.2	0.0	0.0	0.0	0.0	0.0	0.0	0.0	0.0	0.0	96.3
21	0.0	0.0	0.0	0.0	0.0	98.2	98.1	98.7	98.8	98.4	0.0	0.0	0.0	0.0	0.0	0.0	0.0	0.0	0.0	96.6
22	0.0	0.0	0.0	0.0	0.0	98.4	98.3	98.8	98.9	98.5	0.0	0.0	0.0	0.0	0.0	0.0	0.0	0.0	0.0	96.9
23	0.0	0.0	0.0	0.0	0.0	98.6	98.4	98.9	99.0	98.7	0.0	0.0	0.0	0.0	0.0	0.0	0.0	0.0	0.0	97.3
24	0.0	0.0	0.0	0.0	0.0	98.7	98.6	99.0	0.0	98.8	0.0	0.0	0.0	0.0	0.0	0.0	0.0	0.0	0.0	97.6
25	0.0	0.0	0.0	0.0	0.0	98.8	98.7	0.0	0.0	99.0	0.0	0.0	0.0	0.0	0.0	0.0	0.0	0.0	0.0	97.8
26	0.0	0.0	0.0	0.0	0.0	99.0	98.9	0.0	0.0	99.1	0.0	0.0	0.0	0.0	0.0	0.0	0.0	0.0	0.0	98.1
27	0.0	0.0	0.0	0.0	0.0	99.1	99.0	0.0	0.0	0.0	0.0	0.0	0.0	0.0	0.0	0.0	0.0	0.0	0.0	98.3
28	0.0	0.0	0.0	0.0	0.0	0.0	0.0	0.0	0.0	0.0	0.0	0.0	0.0	0.0	0.0	0.0	0.0	0.0	0.0	98.5
29	0.0	0.0	0.0	0.0	0.0	0.0	0.0	0.0	0.0	0.0	0.0	0.0	0.0	0.0	0.0	0.0	0.0	0.0	0.0	98.7
30	0.0	0.0	0.0	0.0	0.0	0.0	0.0	0.0	0.0	0.0	0.0	0.0	0.0	0.0	0.0	0.0	0.0	0.0	0.0	98.9
31	0.0	0.0	0.0	0.0	0.0	0.0	0.0	0.0	0.0	0.0	0.0	0.0	0.0	0.0	0.0	0.0	0.0	0.0	0.0	99.1
32	0.0	0.0	0.0	0.0	0.0	0.0	0.0	0.0	0.0	0.0	0.0	0.0	0.0	0.0	0.0	0.0	0.0	0.0	0.0	0.0
33	0.0	0.0	0.0	0.0	0.0	0.0	0.0	0.0	0.0	0.0	0.0	0.0	0.0	0.0	0.0	0.0	0.0	0.0	0.0	0.0
34	0.0	0.0	0.0	0.0	0.0	0.0	0.0	0.0	0.0	0.0	0.0	0.0	0.0	0.0	0.0	0.0	0.0	0.0	0.0	0.0
35	0.0	0.0	0.0	0.0	0.0	0.0	0.0	0.0	0.0	0.0	0.0	0.0	0.0	0.0	0.0	0.0	0.0	0.0	0.0	0.0
⋮	⋮	⋮	⋮	⋮	⋮	⋮	⋮	⋮	⋮	⋮	⋮	⋮	⋮	⋮	⋮	⋮	⋮	⋮	⋮	⋮

APPENDIX H : PCAR methods and P and C values for whole hand predictions

According to Jolliffe (2002) and Reed and Parkinson (2008), G was decomposed as follows,

$$G = SP$$

(1)

$$S = GP^T$$

(2)

Where S is an $N \times l$ matrix called principal component (PC) scores and P is the eigenvectors of G, which is an $l \times N$ normalized matrix. The matrix G can be approximated by taking the first k PCs based on a preset desired cumulative variance.

$$G^* = S_k P_k$$

(3)

Any subject's nodal coordinates could be obtained based on Equation 4.

$$g_i^* = \overline{g} + P_k^T S_{Ni}^T$$

(4)

Where S_{Ni} is the row of matrix S_N corresponding to the PC scores of i-th subject. In simple terms, the PC scores are re-arrangements of the data so that it can be explained with significantly fewer variables. For predicting the relationship between the PC scores S_k and the subject's parameters such as hand length, handbreadth, hand thickness and sex, as well as a detailed geometry, a regression analysis was performed.

This regression model was generated based on the method proposed by Reed and Parkinson (2008)

$$S_k^T = CF + \varepsilon^T$$

(5)

Where $\boldsymbol{F}$ is the feature matrix, $\boldsymbol{C}$ is the coefficient matrix and ε^T is a vector of zero mean and normally distributed residuals. After, $\bar{\boldsymbol{g}}$, $\boldsymbol{P}$ and $\boldsymbol{C}$ are determined, the model regression can be represented as

$$\begin{bmatrix} X_i \\ Y_i \\ Z_i \end{bmatrix} = \begin{bmatrix} \bar{\boldsymbol{g}}_{3i-2} + [\boldsymbol{Px}[\boldsymbol{C}[\text{hand length, hand breadth, hand thickness, sex, 1}]^T]]_{3i-2} \\ \bar{\boldsymbol{g}}_{3i-1} + [\boldsymbol{Px}[\boldsymbol{C}[\text{hand length, hand breadth, hand thickness, sex, 1}]^T]]_{3i-1} \\ \bar{\boldsymbol{g}}_{3i} \ \ + [\boldsymbol{Px}[\boldsymbol{C}[\text{hand length, hand breadth, hand thickness, sex, 1}]^T]]_{3i} \end{bmatrix}$$

(6)

Where X_i, Y_i, and Z_i are the coordinates of the i-th vertex and the units for age, stature, and BMI are year, centimeter, and kg, respectively, and sex (assigned as 0 for female and 1 for males). The PCAR models in this study used the same number of PC scores as number of subjects (43 subjects), covering more than 99% of the variance in the data.

Table A.3The following table provides the PC Scores for the predictors obtained from the PCAR in order to model the whole hand skeleton. These coefficients can be used to determine the shape/size of the hand bones using the regression model developed in Chapter 5.

	1	2	3	4	5	6	7	8	9	10	11	12	13	14	15	16	17	18	19	20
1	-696.0	-217.2	-121.5	101.3	27.0	-79.7	-54.3	33.5	66.9	-77.0	125.5	-96.1	47.0	5.0	-48.0	-58.4	-18.6	56.7	-27.8	-8.6
2	-33.8	-406.6	1470.6	59.2	1412.7	700.1	2.1	49.4	45.9	11.7	-26.1	-20.3	-8.5	17.3	-4.7	7.0	-2.0	-10.8	5.6	12.8
3	2288.9	3438.7	-60.0	1723.0	46.4	-85.0	-36.2	188.7	248.2	71.8	-39.1	-15.3	-18.7	-8.7	-14.1	20.0	-11.9	-30.3	-10.5	-8.1
4	-623.2	-369.4	243.2	165.3	-44.2	3.9	-68.2	-8.9	148.5	-206.5	87.8	218.8	34.9	31.9	-1.5	-37.1	101.0	128.8	-32.4	-63.0
5	-846.6	-200.9	-80.6	137.7	-37.4	-59.1	-63.7	73.5	80.0	-147.8	17.5	-47.3	-101.9	-14.9	21.3	-50.2	36.2	152.8	25.9	37.5
6	-689.0	-252.6	69.8	97.6	-63.5	-28.8	-45.1	-8.8	-14.2	-21.5	4.2	-17.4	-5.7	-26.9	58.2	-71.2	-37.5	-42.5	-80.0	126.4
7	-753.8	-214.9	146.5	44.1	-48.8	-46.3	-65.1	12.5	-83.2	-11.6	-5.2	-43.3	11.0	5.6	9.6	10.8	-14.4	-4.3	7.4	-7.6
8	-693.3	-314.4	-305.2	12.4	111.4	-35.1	-142.5	-9.6	-134.9	512.3	204.2	80.5	-234.6	-33.2	-13.7	-131.9	40.9	18.0	5.2	-51.3
9	-2633.3	-197.9	-1077.2	-34.5	97.4	10.9	-73.0	38.9	24.6	-20.9	-31.5	-47.1	-109.9	92.9	-7.5	-39.1	-13.7	-39.1	24.4	71.1
10	605.6	336.4	-1070.6	140.4	-696.3	1114.3	81.9	-187.9	-26.7	54.5	6.4	-47.8	49.1	-73.2	-32.2	21.6	53.8	24.7	-8.6	7.8
11	-2666.5	2513.8	-311.0	-1027.9	217.5	-66.7	-263.0	46.3	-331.2	65.3	-254.9	72.5	136.6	50.4	-116.4	-69.8	18.8	37.5	7.1	-6.4
12	56.0	-433.1	610.9	73.1	-37.5	-283.3	287.2	-307.1	135.5	168.4	-263.0	-102.0	6.0	-15.4	-58.3	-45.9	75.6	72.1	-71.8	105.4
13	-0.8	293.6	577.8	-1440.0	-426.1	107.8	-114.2	461.0	524.3	106.2	-32.1	-64.5	-43.9	-29.9	-13.9	23.3	-13.2	-33.1	-7.3	-8.3
14	-1728.7	-210.2	-336.9	-44.9	91.9	-82.4	-81.0	5.6	-14.9	-68.4	-47.1	36.3	10.1	-25.1	-0.9	4.2	12.5	-66.9	24.8	14.7
15	-134.9	-255.7	371.7	113.9	-164.0	-25.0	6.9	-0.2	-83.1	45.6	28.2	31.0	-90.0	-15.0	9.6	86.2	-96.8	3.4	19.5	40.0
16	-608.9	-191.8	81.1	59.9	-84.6	-23.8	-23.2	-3.3	-124.6	-7.7	23.6	-76.3	-52.1	-39.0	0.3	38.1	-87.5	-7.3	-20.9	-45.1
17	30286.6	-179.4	-426.2	-267.3	123.3	-69.5	0.1	-20.2	-34.4	-30.6	-11.0	5.9	-2.0	8.6	0.4	-4.9	-4.1	-1.1	3.8	-1.4
18	-56.5	-234.2	681.1	133.6	-206.7	6.6	-67.4	38.8	-132.4	-51.5	36.2	-63.1	6.1	-43.5	-91.2	16.2	-76.5	31.5	3.8	-20.8
19	-1709.7	-166.0	-449.5	-33.1	93.0	-5.8	-96.2	-27.8	-42.0	-127.6	-49.9	-152.8	-24.9	-17.8	95.0	-45.8	-12.2	-26.1	-74.3	-54.3
20	-1480.8	-203.5	-601.7	-31.1	240.6	-149.6	-22.0	-70.3	140.2	24.4	110.3	-34.1	114.7	-88.3	86.6	9.1	113.6	-35.1	20.0	16.1
21	-1025.1	2686.2	707.0	-930.7	-3.8	-45.8	289.7	-371.7	-66.0	-145.1	280.1	10.9	-101.2	-5.8	130.8	37.9	-0.6	9.1	1.5	22.6
22	-511.8	-291.0	27.0	79.4	52.9	-114.8	-67.2	27.9	-7.1	41.4	-12.2	39.8	1.8	45.1	44.2	89.2	26.5	24.6	46.0	-44.7
23	-255.4	-339.4	371.8	102.0	-188.6	5.3	-91.4	57.8	-35.0	-31.8	-173.8	185.8	-49.9	7.5	160.7	16.5	116.4	-89.2	-74.6	-40.8
24	-1709.4	-225.0	-558.3	-63.8	184.8	-70.9	-107.4	-47.9	-25.9	48.3	4.9	-80.0	93.4	-61.3	62.3	-10.2	9.0	-62.2	15.1	-14.9
25	-1519.1	-277.7	-429.6	43.0	-73.0	123.1	-9.8	-17.4	103.3	-80.9	-26.5	165.2	-8.1	132.3	-16.2	-4.4	-75.7	8.3	63.1	52.3
26	543.5	-264.9	1118.6	232.3	-478.2	95.9	-79.5	25.6	-233.9	-0.1	-167.1	-45.2	-13.6	27.1	109.3	-16.3	-22.1	-16.4	60.2	-21.0
27	-1054.5	-198.8	21.3	32.5	-21.2	-14.6	-26.8	-18.5	-42.8	-153.8	-31.4	-38.9	-19.3	-22.4	-18.0	-66.1	-27.7	-72.8	-93.3	-60.8
28	-969.0	-358.2	-424.0	3.5	23.5	-14.5	-43.6	-37.9	44.0	269.1	14.0	59.5	155.6	198.4	162.8	122.3	-99.2	75.4	-63.8	14.4
29	-136.2	-221.9	510.7	209.6	-224.7	44.8	-2.1	76.6	20.2	-113.7	26.0	4.4	-54.2	131.0	-41.9	-108.5	-29.3	31.6	-17.3	-24.9
30	-25.6	-322.4	399.5	74.0	-204.4	-16.2	-48.6	-39.7	-68.5	-13.0	89.6	182.4	40.8	-101.7	-71.5	-15.8	-39.9	-81.6	-18.1	79.2
31	-1336.2	-306.2	-494.9	10.0	131.3	-86.7	-13.1	-49.3	92.6	-85.2	88.9	97.8	-4.4	47.7	-44.4	-53.1	9.3	-79.8	57.0	45.4
32	-1554.1	-160.5	-587.8	-38.0	126.9	-34.0	949.2	524.2	-204.1	5.8	-4.4	67.2	45.4	-63.7	22.1	-17.9	-4.3	21.5	-9.8	-4.3
33	-2423.6	-213.5	-1186.7	-146.6	299.0	-45.3	-85.1	-65.4	36.2	-91.2	-33.6	-84.0	20.0	12.1	7.0	9.9	-15.4	33.6	-11.4	-33.0
34	-275.3	-289.3	473.1	45.5	-215.1	-74.0	288.9	-88.3	-52.6	40.8	97.9	-128.7	4.0	261.9	-157.3	85.5	130.0	-96.8	-3.7	-29.8
35	-657.7	-263.5	154.8	-8.9	111.9	-200.0	-111.4	-8.5	-58.3	42.8	79.6	-41.2	4.4	-130.8	-99.6	148.5	0.4	41.7	-95.2	-5.7
36	205.7	-321.9	691.4	176.9	-237.0	-9.0	-135.2	54.6	-101.2	-13.8	-51.8	56.4	27.3	-52.3	-15.7	12.7	28.6	33.0	19.8	22.5
37	-1510.1	-156.1	-464.1	7.2	54.5	-45.9	13.0	27.1	-25.9	-60.1	23.0	-110.2	-62.6	57.8	-14.3	-20.9	-52.8	-2.5	21.7	-18.4
38	-1357.3	-308.6	-249.2	1.7	80.1	-56.2	-112.5	-29.5	38.9	-26.3	95.8	141.4	87.5	-60.2	-137.3	85.8	-22.9	-21.6	-17.3	-22.3
39	-1457.7	-202.6	-346.8	40.2	83.1	-117.9	-96.8	80.9	-86.7	-72.2	-132.7	-55.0	-154.6	-75.3	9.3	151.4	82.4	29.3	118.0	30.9
40	-1299.5	-289.2	52.3	-54.4	24.2	-103.9	382.7	-458.1	283.9	65.7	-218.3	75.7	-7.6	-87.5	-28.6	-32.8	-95.5	-15.6	74.7	-102.6
41	447.1	-210.3	801.3	202.1	-178.4	-122.8	-55.8	53.6	-3.3	84.3	168.1	-120.8	271.9	-41.0	57.7	-96.2	18.9	1.6	113.3	-1.0

21	22	23	24	25	26	27	28	29	30	31	32	33	34	35	36	37	38	39	40	41
35.4	37.1	-22.8	-59.5	32.1	-51.1	18.3	23.3	12.6	-38.3	-8.3	23.2	-3.0	9.1	35.0	21.9	5.6	-22.5	-34.7	46.1	-91.2
2.5	-2.6	-2.9	-3.6	2.9	-1.9	-0.5	-2.9	-5.6	2.0	-0.7	0.8	-1.8	-0.2	-0.4	-1.1	0.0	0.0	-0.8	0.9	-12.9
11.8	2.2	10.7	4.9	1.3	2.3	-0.4	2.2	-4.1	4.1	-0.9	-2.0	-0.8	-1.2	-2.1	1.0	1.7	-0.5	2.3	0.3	-6.7
53.0	-59.0	11.9	14.0	-45.2	-12.2	46.8	27.3	-6.7	45.0	17.4	0.6	23.0	-13.8	-18.3	1.7	14.0	-11.5	10.8	1.9	7.3
-50.1	-7.0	14.4	-19.3	84.2	55.6	0.7	-35.4	-32.8	-15.3	9.4	2.1	-28.5	9.9	-36.7	-20.6	5.6	22.6	-21.2	-6.5	17.3
22.4	6.8	-38.0	0.7	-52.7	51.7	64.2	-11.2	-1.2	-63.9	22.6	-39.7	35.6	10.1	-12.9	6.1	17.3	-7.1	0.4	-4.5	4.2
-67.1	9.5	-45.4	45.0	18.3	34.3	-23.7	2.9	18.7	26.7	5.7	-8.5	-26.6	3.2	-46.2	69.0	11.4	-24.6	31.0	29.6	-33.1
3.2	30.3	18.7	16.9	-13.0	5.9	3.6	4.4	-7.4	-5.6	-0.7	0.3	-2.6	-2.6	2.8	1.3	3.5	-0.9	-0.2	0.8	-8.8
52.8	20.9	-85.0	-50.5	-21.9	-21.8	4.6	-31.9	28.0	77.3	-16.2	32.7	10.6	8.7	-28.2	-21.4	-8.0	13.1	8.1	6.8	-26.5
-19.2	-11.9	-5.3	1.1	-1.0	-7.0	-10.3	2.3	9.6	-4.9	5.6	-6.4	3.1	0.0	-1.3	-3.1	-0.1	-3.0	-3.8	1.1	15.3
-20.9	-33.6	-9.8	-27.6	-2.9	11.3	6.8	7.9	-9.6	-12.2	8.6	5.6	3.8	0.2	-1.5	0.2	-1.4	-0.1	-2.1	-0.7	10.0
9.6	-13.8	24.5	52.5	-3.1	-46.0	-39.4	1.7	10.1	11.7	-2.5	19.7	4.8	-7.2	3.4	9.4	-1.1	2.1	-5.0	-5.1	8.3
15.7	-3.7	11.6	9.0	-0.7	1.6	-1.5	5.1	-4.3	3.8	-2.5	-3.8	1.0	-0.6	-2.8	1.9	2.0	-1.3	1.3	0.2	-26.7
-50.5	13.2	37.0	36.9	2.3	11.9	-5.7	-26.8	37.6	16.6	1.8	-2.5	-9.4	-47.5	23.9	-45.7	67.2	-20.1	-10.4	19.3	-8.1
-40.1	-75.4	25.2	-35.4	-2.9	49.4	-11.0	16.9	1.5	29.5	44.0	25.2	44.3	-51.0	19.7	18.0	-29.3	10.9	-22.0	13.9	-8.4
15.9	-72.4	-37.8	-31.9	7.3	-47.1	-18.8	-9.9	-36.8	0.2	-36.2	9.9	9.7	-12.4	-10.8	29.0	55.2	-5.8	-14.4	-43.1	24.8
0.2	2.2	-1.9	0.1	-1.4	1.2	3.1	-1.1	0.6	1.4	0.3	1.6	-0.9	-0.4	-0.2	-0.6	0.4	0.8	0.5	-0.1	-23.5
11.4	75.6	17.2	19.8	44.9	-0.9	3.9	21.0	19.0	-28.6	10.2	55.8	45.3	1.9	-19.2	-33.9	-3.4	-20.8	43.2	-13.7	15.0
9.0	0.3	30.0	-10.7	-40.5	-11.5	-22.2	51.0	-13.7	-30.8	3.4	8.8	-24.4	-34.7	-9.4	-6.8	3.8	60.4	27.7	16.7	12.7
-23.1	-58.6	-21.4	-18.2	-10.4	73.6	-13.2	13.5	-11.7	-9.0	-28.9	61.5	-2.3	26.4	40.0	2.8	-0.4	-13.1	20.1	-12.5	9.7
12.4	33.2	-3.4	19.7	2.9	-15.1	-5.5	-9.1	13.1	7.1	-7.7	-2.1	-2.2	1.3	3.9	-1.0	-1.8	1.9	-0.9	-0.1	-4.2
-15.4	-52.2	28.1	-0.3	-25.1	-17.2	-59.3	-29.5	49.4	-43.3	-22.2	-18.8	55.9	54.9	-21.1	-7.0	8.4	22.3	-5.9	21.0	4.8
-22.7	47.9	-35.6	-39.0	48.1	-42.0	-16.9	-38.3	-6.5	-20.0	43.6	14.9	4.2	-9.1	5.8	7.5	-14.8	-9.5	-0.3	-7.4	-4.3
24.9	-32.6	74.6	18.5	78.6	-23.0	89.8	0.2	64.3	22.8	-0.5	-10.8	4.7	3.8	-8.8	23.0	-12.0	18.9	-6.4	-16.7	9.6
-47.0	83.8	86.6	-9.0	-44.5	-19.2	7.6	-0.7	-6.0	-6.3	14.3	31.1	-18.3	29.6	21.2	37.9	17.3	16.8	4.2	-18.7	4.3
131.4	-19.0	25.7	16.8	-27.7	43.5	-4.9	7.4	8.1	9.6	3.9	17.1	-45.2	28.3	2.9	-9.3	-0.5	-14.9	-20.5	3.5	-5.2
-100.9	36.0	16.3	45.5	-28.2	13.1	6.4	24.7	-28.8	42.8	-36.1	3.9	20.1	37.2	-10.3	-14.2	-23.7	-10.0	-40.6	-2.2	-0.3
-19.4	7.2	-22.6	16.3	22.8	-5.2	16.5	27.1	-18.4	1.3	-24.6	-7.5	-15.9	-8.3	-6.1	-28.3	-5.4	-11.2	-0.3	1.5	7.1
-48.9	-52.8	-22.9	-4.3	-15.3	5.8	-2.5	-31.1	70.4	-28.0	-50.5	-19.0	-24.8	-29.5	32.8	-0.9	-33.2	-7.8	14.8	-20.2	7.1
14.8	-65.6	63.1	-26.0	23.4	-37.5	-1.6	-26.8	-53.9	0.5	-47.2	-9.6	-22.0	6.6	-14.1	-11.9	-16.2	-3.4	24.4	24.9	5.1
28.0	-17.8	-16.7	-1.3	35.4	-7.2	-72.4	96.4	18.1	-17.7	26.4	-32.7	-8.6	-1.5	-22.7	-10.4	-7.3	-14.8	-15.1	-20.1	10.3
11.3	8.2	2.5	2.3	-2.5	2.6	-2.2	3.6	6.6	1.1	-1.4	-0.5	-2.6	0.4	-1.1	0.3	-0.4	2.3	0.1	0.2	-4.8
91.6	60.2	67.0	-2.0	-0.7	35.2	-52.2	-52.2	-33.7	7.1	-9.8	-37.6	23.5	-25.1	10.7	16.6	-23.0	-30.7	5.6	-5.5	15.6
7.2	6.2	19.9	-27.3	11.3	32.2	32.2	-3.8	-30.1	-7.1	2.3	-6.5	2.1	-6.5	-8.1	0.8	9.3	8.6	0.6	2.4	16.8
-18.2	19.0	13.4	-70.9	-44.3	0.5	-7.4	-1.9	41.2	26.0	42.8	-27.5	-46.1	27.8	3.5	-14.3	-2.8	-7.2	3.5	-14.5	16.5
16.4	73.4	-49.4	-3.2	44.4	24.2	-9.1	34.6	-10.0	44.3	-37.7	-51.2	24.2	9.9	55.4	6.5	14.4	39.6	12.7	-0.8	5.4
-11.7	-80.9	-33.8	67.6	19.0	-44.8	7.2	-20.1	-41.2	8.8	72.4	-18.1	-2.3	39.7	50.1	-14.4	-4.1	-1.9	21.2	4.8	9.8
59.5	20.7	-72.5	92.7	-7.4	16.3	-3.1	-38.8	3.1	-31.0	3.2	28.5	-20.5	-16.8	-3.6	7.6	-13.8	35.3	-24.9	-2.2	5.7
-30.6	17.3	-16.5	22.2	-40.6	-45.4	53.0	29.8	-23.0	-31.6	-32.7	-11.4	-8.0	-20.2	-3.1	-0.8	-23.0	-18.5	-1.6	-0.3	-1.4
-9.4	8.9	-38.3	-47.0	1.8	24.8	33.1	-1.9	-4.8	-10.1	3.4	-15.4	-3.9	2.9	-6.2	-9.8	0.3	-0.2	6.8	7.2	9.8
-45.2	38.4	-16.2	-15.2	-48.8	-40.7	-13.7	-30.1	-21.7	14.0	26.1	-11.7	5.1	-23.2	-16.1	-6.8	-11.9	6.3	-8.2	-8.1	13.4

Table A.4 The coefficients for the predictors obtained from the PCAR in order to model the surfaces of the hand bones. These coefficients can be used to determine the shape/size of the hand bones using the regression model developed in Chapter 5.

Hand Length	Hand Breadth	Hand Thickness	Sex	1
176.8559621	67.43729507	61.26724238	156.5222596	-23332.52622
367.940061	10.81322	-30.72125101	56.85549759	-1459.636787
61.37759442	39.05423516	-8.909281338	12.41050064	-6998.196352
-295.8335261	-9.168046431	41.63053758	-17.09620877	-1174.523788
-22.35636963	5.633617075	-31.57459096	4.786447051	1508.205368

REFERENCES

Albrecht, I., Haber, J., & Seidel, H. (2003). Construction and Animation of Anatomically Based Human Hand Models, 98–110.

Alexander, B., & Viktor, K. (2010). Proportions of Hand Segments, 28(3), 755–758.

Armstrong T.J., Choi, J. and Ahuja, V. (2008). Development of kinematic and biomechanical hand models for ergonomic applications. Handbook of Digital Human Modeling. V.G. Duffy, CRC Press.

Armstrong, T., C. Best, S. Bae, J. Choi, D. Grieshaber, D. Park, C. Woolley, and W. Zhou. (2009). Development of a kinematic hand model for study and design of hose installation, in Digital Human Modeling. Springer Berlin/Heidelberg. p. 85

Armstrong, T. J., Fine, L. J., Goldstein, S. A., Lifshitz, Y. R., & Silverstein, B. A. (1987). Ergonomics considerations in hand and wrist tendinitis. The Journal of hand surgery, 12(5), 830-837.

Bae, S., Choi, J. & Armstrong, T.J. (2008). Influence of object properties on reaching and grasping tasks. Proceedings of the SAE Digital Human Modeling for Design and Engineering Conference, Pittsburgh, PA

Barr, A., & Barbe, M. (2004). Work-related musculoskeletal disorders of the hand and wrist: epidemiology, pathophysiology, and sensorimotor changes. The Journal of Orthopaedic and, 34(10), 610–627.

Bell, A. L., Brand, R. A., & Pedersen, D. R. (1989). Prediction of hip joint centre location from external landmarks. Human Movement Science, 8(1), 3–16.

Bennink, H.E., Korbeeck, J.M., Janssen, B.J. and ter Haar Romeny, B.M., 2006. Warping a neuro-anatomy atlas on 3D MRI data with radial basis functions. Proc. International Conference on Biomedical Engineering 3, 214-218.

Besl P., McKay N. (1992) A method for registration of 3-D shapes, IEEE Transactions on Pattern Analysis and Machine Intelligence 14. 239–256.

Bey, M. J., Zauel, R., Brock, S. K., & Tashman, S. (2006). Validation of a new model-based tracking technique for measuring three-dimensional, in vivo glenohumeral joint kinematics. Journal of Biomechanical Engineering, 128(4), 604–609.

Blackwell, J.R., K.W. Kornatz, and E.M. Heath (1999), Effect of grip span on maximal

grip force and fatigue of flexor digitorum superficialis. Applied Ergonomics. 30(5): p. 401-5.

Bredbenner, T. L., Eliason, T. D., Potter, R. S., Mason, R. L., Havill, L. M., & Nicolella, D. P. (2010). Statistical shape modeling describes variation in tibia and femur surface geometry between Control and Incidence groups from the osteoarthritis initiative database. Journal of Biomechanics, 43(9), 1780–6.

Brett, A. D., & Taylor, C. J. (2000). A method of automated landmark generation for automated 3D PDM construction. Image and Vision Computing, 18(9), 739-748.

Buchholz, B. & Armstrong, T.J. (1992). A kinematic model of the human hand to evaluate its prehensile capabilities. J Biomech 25(2), 149-62

Buchholz, B., Armstrong, T. J., & Goldstein, S. a. (1992). Anthropometric data for describing the kinematics of the human hand. Ergonomics, 35(3), 261–73.

Budgeon, M.K.; Latash, M.L.; Zatsiorsky, V.M. (2008). Digit force adjustments during finger addition/removal in multi-digit prehension. Exp. Brain. Res. 189, 345–359.

Bullock, I. M., Borras, J., & Dollar, A. M. (2012). Assessing assumptions in kinematic hand models: A review. Proceedings of the IEEE RAS and EMBS International Conference on Biomedical Robotics and Biomechatronics, 139–146.

Bureau Of Labor Statistics. (2016). Nonfatal occupational injuries and illnesses with days away from work 2015, (202), 1–28.

Centers for Disease Control and Prevention. (2008) National Hospital Ambulatory Medical Care Survey: 2008 Emergency Department Summary Tables, 2011(October 24).

Cerveri, P., Lopomo, N., Pedotti, A., & Ferrigno, G. (2005). Derivation of centers and axes of rotation for wrist and fingers in a hand kinematic model: Methods and reliability results. Annals of Biomedical Engineering, 33(3), 402–412.

Chaffin, D. B. (2008). Digital Human Modeling for Workspace Design. Reviews of Human Factors and Ergonomics, 4(1), 41–74.

Chaffin, D., Andres, R., & Garg, A. (1983). Volitional postures during maximal push/pull exertions in the sagittal plane. Human Factors: The Journal of the Human Factors and Ergonomics Society.

Chalovich, J. M., & Eisenberg, E. (2005). NIH Public Access. Biophysical Chemistry, 257(5), 2432–2437.

Chang, L. Y., & Pollard, N. S. (2007). Constrained least-squares optimization for robust estimation of center of rotation. Journal of Biomechanics, 40(6), 1392–1400.

Choi, J. (2008). Developing a 3-dimensional kinematic model of the hand for ergonomic analyses of hand posture, hand space envelope, and tendon excursion. Ph.D. Thesis. The University of Michigan. Ann Aarbor

Das, B., & Wang, Y. (2004). Isometric pull-push strengths in workspace: 1. Strength profiles. International Journal of Occupational Safety and Ergonomics, 10(1), 43–58.

Delp, S. L., Anderson, F. C., Arnold, A. S., Loan, P., Habib, A., John, C. T., … Thelen, D. G. (2007). OpenSim: open-source software to create and analyze dynamic simulations of movement. IEEE Transactions on Bio-Medical Engineering, 54(11), 1940–50.

De Looze, M. P., Van Greuningen, K., Rebel, J., Kingma, I., & Kuijer, P. P. F. M. (2000). Force direction and physical load in dynamic pushing and pulling. Ergonomics, 43(3), 377-390. Chicago

Dennerlein, J. T., Diao, E., Mote, C. D., & Rempel, D. M. (1998). Tensions of the flexor digitorum superficialis are higher than a current model predicts. *Journal of Biomechanics*, *31*(4), 295–301.

Dewaele, G., Devernay, F., & Horaud, R. (2004). Hand motion from 3d point trajectories and a smooth surface model. In European Conference on Computer Vision (pp. 495-507). Springer Berlin Heidelberg.

Di Domizio, J., & Keir, P. J. (2010). Forearm posture and grip effects during push and pull tasks. Ergonomics, 53(3), 336–43.

Dickerson, C.R., Martin, B.J. & Chaffin, D.B., 2007. Predictors of perceived effort in the shoulder during load transfer tasks. Ergonomics, 50 (7), 1004 - 1016.

Dijkerman, H., Mcintosh, R., Schindler, I., Nijboer, T. & Milner, A., 2009. Choosing between alternative wrist postures: Action planning needs perception. Neuropsychologia, 47 (6), 1476-1482

Drillis, R., Contini, R., & Maurice Bluestein, M. M. E. (1966). Body Segment Parameters.

Hargittai, I., & Hargittai, M. (1994). Symmetry: A unifying concept. Shelter Publications, Inc.

Eaton, C. (2007). Hand Facts and Trivia. The Electronic textbook of Hand Surgery. Retrieved 2012-02-18.

Eberharter, J. K., & Ravani, B. (2006). Kinematic Registration in 3D Using the 2D Reuleaux Method. Journal of Mechanical Design, 128(2), 349.

Eberly, D. (1999). Least squares fitting of data. Www. Magic-Software. Com Lsfit.

Pdf, 1–10.

Eberly, D. (2011). Distance from a Point to an Ellipse, an Ellipsoid, or a Hyperellipsoid. Matrix, 1–28.

Ehrig, R. M., Taylor, W. R., Duda, G. N., & Heller, M. O. (2006). A survey of formal methods for determining the centre of rotation of ball joints. Journal of Biomechanics, 39(15), 2798–2809.

El-shennawy et al. 2001- Three-Dimensional Kinematic Analysis of the Second Through Fifth Carpometacarpal Joints

Elkus, R., & Basmajian, J. V. (1973). Endurance in hanging by the hands. Why do people hanging by their hands let go?. American journal of physical medicine, 52(3), 124-127.

Endo, Y., Tada, M., & Mochimaru, M. (2014). Reconstructing individual hand models from motion capture data. Journal of Computational Design and Engineering, 1(1), 1–12.

Feehan LM, Sheps SB. (2006) Incidence and demographics of hand fractures in British Columbia, Canada: a population-based study. Journal Hand Surgery. 31.

Figueroa, R., D, T. J. A. P., Woolley, C., Sun, L., & Zhou, W. (2016). Determining instantaneous centers of rotation for finger joints through different postures using the iterative closest point algorithm (ICP). In Proceedings of the Human Factors and Ergonomics Society 2016 Annual Meeting (pp. 1470–1474).

Figueroa, R., Das, S., Armstrong, T., Woolley, C., & Chung, K. (2014). Enhanced Hand Function Assessment Using Pressure Mapping and Low Cost Motion Capture. In Proceedings of the Human Factors and Ergonomics Society Annual Meeting (Vol. 58, No. 1, pp. 1290-1294). SAGE Publications.

Fischer, S. L., Picco, B. R., Wells, R. P., & Dickerson, C. R. (2013). The roles of whole body balance, shoe-floor friction, and joint strength during maximum exertions: Searching for the "weakest link." Journal of Applied Biomechanics, 29(1), 1–11.

Fodor, I.K. (2002) A Survey of Dimension Reduction Techniques. Lawrence Livermore National Laboratory Technical Report no. UCRL-ID-148494

Fowler, N. K., Nicol, a C., Condon, B., & Hadley, D. (2001). Method of determination of three dimensional index finger moment arms and tendon lines of action using high resolution MRI scans. Journal of Biomechanics, 34(6), 791–7.

Fransson, C., Winkel, J. (1991). Hand strength: the influence of grip span and grip type. Ergonomics, 34(7), 881-892.

Frontera, W. R., Hughes, V. a, Lutz, K. J., & Evans, W. J. (1991). A cross-sectional study of muscle strength and mass in 45- to 78-yr-old men and women. Journal of Applied Physiology (Bethesda, Md. : 1985), 71(2), 644–650.

Gamage, S. S. H. U., & Lasenby, J. (2002). New least squares solutions for estimating the average centre of rotation and the axis of rotation. Journal of Biomechanics, 35(1), 87–93.

Garg, a., & Kapellusch, J. M. (2011). Job Analysis Techniques for Distal Upper Extremity Disorders. Reviews of Human Factors and Ergonomics, 7(1), 149–196.

Garrett, J. W. (1971). The adult human hand: some anthropometric and biomechanical considerations. Human Factors, 13(2), 117–131. http://doi.org/10.1016/S0003-6870(72)80027-9

Gilles, B., Reveret, L., & Pai, D. K. (2010). Creating and animating subject-specific anatomical models. Computer Graphics Forum, 29(8), 2340–2351. http://doi.org/10.1111/j.1467-8659.2010.01718.x

Goodall, C. (1991). Procrustes methods in the statistical analysis of shape. Journal of the Royal Statistical Society. http://doi.org/10.2307/2345744

Gordon, C.C., Churchill, T., Clauser, C.E., Bradtmiller, B., McConville, J.T., Tebbetts, I., and Walker, R.A. (1989). 1988 Anthropometric Survey of U.S. Army Personnel: Methods and Summary Statistics. (Final Report. (NATICK/TR-89/027).

Gower, J. C. (1975). Generalized procrustes analysis. Psychometrika, 40(1), 33-51.

Granata, K. P., & Bennett, B. C. (2005). Low-back biomechanics and static stability during isometric pushing. *Human factors*, *47*(3), 536-549.

Grieshaber, C.D. (2007) Factors affecting hand posture and one-handed push force during flexible rubber hose insertions tasks. Ph.D. Dissertation. The University of Michigan, Ann Arbor.

Haas, J. C., & Meyers, M. C. (1995). Rock climbing injuries. Sports Medicine, 20(3), 199-205.

Halvorsen, K., Lesser, M., & Lundberg, A. (1999). A new method for estimating the axis of rotation and the center of rotation. Journal of Biomechanics, 32(11), 1221–1227.

Hamelund C. (2012) Summary of Oregon OSHA Accidents Reports (Form 170). Retrieved November 13, 2013, from http://www.orosha.org/pdf/pubs/reports/ladder-narratives2010topresent.pdf

Hamilton, G. F., McDonald, C., & Chenier, T. C. (1992). Measurement of grip strength: validity and reliability of the sphygmomanometer and jamar grip

dynamometer. Journal of Orthopaedic & Sports Physical Therapy, 16(5), 215-219.

Hazelton, F. T., G. L. Smidt, A. E. Flatt and R. I. Stephens (1975). "The influence of wrist position on the force produced by the finger flexors." J Biomech 8(5): 301-6.

Hoffman, S. G., Reed, M. P., & Chaffin, D. B. (2007). The Relationship between Hand Force Direction and Posture during Two-Handed Pushing Tasks. Proceedings of the Human Factors and Ergonomics Society Annual Meeting, 51(15), 928–932.

Hsiao, H., Whitestone, J., Taylor, S., Godby, M., & Guan, J. (2009). Harness Sizing and Strap Length Configurations. Human Factors: The Journal of the Human Factors and Ergonomics Society, 51(4), 497–518

Innovision Systems (2012). MaxTRAQ 3-D, Innovision Systems, Inc.

Jan, S. V. S., Giurintano, D. J., Thompson, D. E., & Rooze, M. (1997). Joint Kinematics Simulation from Medical Imaging Data. IEEE Trans Biomed Eng., 44(12), 1175–1184.

Joliffe, I.T. (2002). Principal component analysis. Springer, ed.

Kargov, A., Pylatiuk, C., Martin, J., Schulz, S., Kargov, A., Pylatiuk, C., … Do, L. (2009). A comparison of the grip force distribution in natural hands and in prosthetic hands A comparison of the grip force distribution in natural hands and in prosthetic hands, 8288(May).

Klein, K. F. (2015). Use of Parametric Finite Element Models to Investigate Effects of Occupant Characteristics on Lower-Extremity Injuries in Frontal Crashes.

Klein, K. F., Hu, J., Reed, M. P., Hoff, C. N., & Rupp, J. D. (2015). Development and Validation of Statistical Models of Femur Geometry for Use with Parametric Finite Element Models. Annals of Biomedical Engineering, 43(10).

Knudson, D. (2007). Fundamentals of biomechanics. Springer Science & Business Media.

Kong, Y. K., Kim, D. M., Lee, K. S., & Jung, M. C. (2012). Comparison of comfort, discomfort, and continuum ratings of force levels and hand regions during gripping exertions. Applied Ergonomics, 43(2), 283–289.

Kuch, J. J., & Huang, T. S. (1995, June). Vision based hand modeling and tracking for virtual teleconferencing and telecollaboration. In Computer Vision, 1995. Proceedings., Fifth International Conference on (pp. 666-671). IEEE.

Kurihara, T., & Miyata, N. (2004). Modeling deformable human hands from medical images. In Proceedings of the 2004 ACM SIGGRAPH/Eurographics symposium on Computer animation (pp. 355-363). Eurographics Association.

Larsen, C. F., Mulder, S., Johansen, A. M. T., & Stam, C. (2004). The epidemiology of hand injuries in the Netherlands and Denmark. European Journal of Epidemiology, 19(4), 323–327.

Lee, J.W., Rim, K., 1991. Measurement of finger joint angles and maximum finger forces during cylinder grip activity. Journal of Biomedical Engineering 13, 152–162.

Lempereur, M., Leboeuf, F., Brochard, S., Rousset, J., Burdin, V., & Rémy-Néris, O. (2010). In vivo estimation of the glenohumeral joint centre by functional methods: Accuracy and repeatability assessment. Journal of Biomechanics, 43(2), 370–374.

Li, Q. L. Q., & Griffiths, J. G. (2004). Least squares ellipsoid specific fitting. Geometric Modeling and Processing, 2004. Proceedings, 2004, 4–9. http://doi.org/10.1109/GMAP.2004.1290055

Lian X, Lambrichts I, Sun Y, Denis K, Hassan B, Li L, Pauwels R, Jacobs R. (2010) A Comparative Evaluation of Cone Beam Computed Tomography (Cbct) and Multi-Slice Ct (Msct). Part Ii: On 3d Model Accuracy. Eur J Radiol. 75(2):270–274.

Lien, C. (2005). A scalable model-based hand posture analysis system. Machine Vision and Applications, 16(3), 157–169.

Lopomo, N., Sun, L., Zaffagnini, S., Giordano, G., & Safran, M. R. (2010). Evaluation of formal methods in hip joint center assessment: An in vitro analysis. Clinical Biomechanics, 25(3), 206–212.

Lu, Y. C., & Untaroiu, C. D. (2013). Statistical shape analysis of clavicular cortical bone with applications to the development of mean and boundary shape models. Computer Methods and Programs in Biomedicine, 111(3), 613–628.

MacKenzie, C. L. and T. Iberall (1994). The Grasping Hand. Amsterdam, North-Holland.

Marin, F., Mannel, H., Claes, L., & Dürselen, L. (2003). Accurate determination of a joint rotation center based on the minimal amplitude point method. Computer Aided Surgery : Official Journal of the International Society for Computer Aided Surgery, 8(1), 30–34.

Marras, W. S., & Radwin, R. G. (2005). Biomechanical Modeling. Reviews of Human Factors and Ergonomics, 1(1), 1–88.

McInerney, T., & Terzopoulos, D. (1996). Deformable models in medical image analysis: a survey. Medical Image Analysis, 1(2), 91–108.

McKinnis, L. N. (2013). Fundamentals of musculoskeletal imaging. FA Davis.

Miyata, N., Kouchi, M., & Mochimaru, M. (2006). Posture Estimation for Screening

Design Alternatives by DhaibaHand - Cell Phone Operation -, (Cm).

Miyata, N., Kouchi, M., & Mochimaru, M. (2007). Generation and validation of 3d links for representative hand models. SAE 2007 Digital Human Modeling for Design

Miyata, N., Kouchi, M., Mochimaru, M., & Kawachi, K. (2005). Hand Link Modeling and Motion Generation from Motion Capture Data Based on 3D Joint Kinematics.

Miyata, N., Nakamura, D., Endo, Y., & Maeda, Y. (2013). Statistical surface shape adjustment for a posable human hand model. In Proc. of the 3rd Int. Symp. on Digital Human Modelling, ID (Vol. 81).

Miyata, N., Shimizu, Y., Motoki, Y., Maeda, Y., & Mochimaru, M. (2006). Hand MoCap by Building Individual Skeleton and Surface Model, 1–7.

Miyata, N., Shimizu, Y., Motoki, Y., Maeda, Y., & Mochimaru, M. (2012). Hand MoCap using an individual model with a skeleton and a surface skin. International Journal of Human Factors Modelling and Simulation 1, 3(2), 147-168.

Chaouch, M., Verroust-Blondet A. (2009). Alignment of 3D models. Graphical Models, Elsevier. IEEE International Conference on Shape Modeling and Applications 2008. 71 (2), pp.63-76.

Mohr, A., & Gleicher, M. (2003). Building efficient, accurate character skins from examples. ACM Transactions on Graphics, 22(3), 562.

Monnet, T., Desailly, E., Begon, M., Vallée, C., & Lacouture, P. (2007). Comparison of the SCoRE and HA methods for locating in vivo the glenohumeral joint centre. Journal of Biomechanics, 40(15), 3487–3492.

Mustvangwa, T. (2015). An Automated Statistical Shape Model Developmental Pipeline: Application to the Human Scapula and Humerus, 62(4), 1098-1107.

Nag, P. (1998) Work accidents among shift workers in industry. International Journal of Industrial Ergonomics. 21(3-4): p. 275.

Napier, J. R. (1956). The prehensile movements of the human hand. J Bone Joint Surg Br 38-B(4): 902-13.

Nicholas, J.W., Corvese, R.J., Woolley, C., and Armstrong, T.J. (2012). Quantification of hand grasp force using a pressure mapping system. Work Journal of Prevention, Assessment and Rehabilitation, 41:605-612.

Nikooyan, A. A., van der Helm, F. C. T., Westerhoff, P., Graichen, F., Bergmann, G., & Veeger, H. E. J. (2011). Comparison of two methods for In Vivo estimation of the glenohumeral joint rotation center (GH-JRC) of the patients with shoulder hemiarthroplasty. PLoS ONE, 6(3), 1–7.

O'brien J., Bodenheimer R., Brostow G., Hodgins J. (2000) Automatic joint parameter estimation from magnetic motion capture data. In Graphics Interface, pp. 53–60.

Ootes, D., Lambers, K. T., & Ring, D. C. (2012). The epidemiology of upper extremity injuries presenting to the emergency department in the United States. Hand, 7(1), 18-22.

Panjabi, M. M. (1979). Centers and angles of rotation of body joints: A study of errors and optimization. Journal of Biomechanics, 12(12), 911–920.

Park, B.-K., Lumeng, J. C., Lumeng, C. N., Ebert, S. M., & Reed, M. P. (2015). Child body shape measurement using depth cameras and a statistical body shape model. Ergonomics, 58(2), 301–9.

Pataky, T.C., Slota, G.P., Latash, M.L. & Zatsiorsky, V.M., 2011. Radial force distribution changes associated with tangential force production in cylindrical grasping, and the importance of anatomical registration. Journal of Biomechanics.

Pomidor, B. J., Makedonska, J., & Slice, D. E. (2016). A landmark-free method for three-dimensional shape analysis. PLoS ONE, 11(3), 1–18. http://doi.org/10.1371/journal.pone.0150368

Powell, M. J. D. (1964). "An efficient method for finding the minimum of a function of several variables without calculating derivatives". Computer Journal. 7 (2): 155–162.

Pratt, V. (1987). Direct least-squares fitting of algebraic surfaces. ACM SIGGRAPH Computer Graphics, 21(4), 145–152.

Rancourt, D., & Hogan, N. (2001). Dynamics of pushing. Journal of Motor Behavior, 33(4), 351–62.

Reed, M. P., Sochor, M. M., Rupp, J. D., Klinich, K. D., & Manary, M. a. (2009). Anthropometric specification of child crash dummy pelves through statistical analysis of skeletal geometry. Journal of Biomechanics, 42(8),

Rehg, J. M., & Kanade, T. (1994). Visual tracking of high dof articulated structures: an application to human hand tracking. In Computer Vision—ECCV'94 (pp.35-46). Springer Berlin Heidelberg.

Reuleaux, F. (1875). Theoretische Kinematik: Grundzuge einer Theorie das Maschinenwesens (F. Vieweg und Sohn, Braunschweig, Germany.

Rogers, M. S., Barr, A. B., Kasemsontitum, B., & Rempel, D. M. (2008). A three-dimensional anthropometric solid model of the hand based on landmark measurements. Ergonomics, 51(4), 511–526.

Rosenbaum, D., Cohen, R., Dawson, A., Jax, S., Meulenbroek, R., Wel, R. & Vaughan,

J., 2009. The posture-based motion planning framework: New findings related to object manipulation, moving around obstacles, moving in three spatial dimensions, and haptic tracking. Progress in Motor Control, 485- 497.

Rosenbaum, D.A., Cohen, R.G., Meulenbroek, R.G. & Vaughan, J., 2006. Plans for grasping objects. In Latash, M. & Lestienne, F. eds. Motor control and learning over the lifespan. New York: Springer, 9-25.

Salimi, I., Frazier, W., Reilmann, R. & Gordon, A.M. (2003). Selective use of visual information signaling objects' center of mass for anticipatory control of manipulative fingertip forces. Exp Brain Res, 150 (1), 9-18.

Sancho-bru, J. L. (2000). Towards a Realistic and Self-Contained Biomechanical Model of the Hand.

Schweizer, A., Frank, O., Ochsner, P. E., & Jacob, H. A. C. (2003). Friction between human finger flexor tendons and pulleys at high loads. Journal of Biomechanics, 36(1), 63–71.

Seo, N. J., Armstrong, T. J., Ashton-Miller, J. a, & Chaffin, D. B. (2007). The effect of torque direction and cylindrical handle diameter on the coupling between the hand and a cylindrical handle. Journal of Biomechanics, 40(14), 3236–43.

Shi, X., Cao, L., Reed, M. P., Rupp, J. D., Hoff, C. N., & Hu, J. (2014). A statistical human rib cage geometry model accounting for variations by age, sex, stature and body mass index. Journal of Biomechanics, 47(10), 2277–2285.

Shim, J.K., Latash, M.L. & Zatsiorsky, V.M., 2005. Prehension synergies: Trial-to-trial variability and principle of superposition during static prehension in three dimensions. Journal of Neurophysiology, 93 (6), 3649-3658.

Shimizu, Y., Kawaguchi, K., & Kanai, S. (2010). Constructing MRI-based 3D Precise Human Hand Models for Product Ergonomic Assessments. Proceedings of Asian Conference on Design and Digital Engineering, (November), 837–844.

Silverstein B, Adams D. (2006) Work-related Musculoskeletal Disorders of the Neck, Back and Upper Extremity in Washington State, 1996-2004. Technical Report No 40-10a-2006. Washington State Department of Labor and Industries, Olympia Washington.

Slice, D.E., (2007). Geometric morphometrics. Annual Review of Anthropology 36, 261- 281

Sorock, G.S., D.A. Lombardi, R.B. Hauser, E.A. Eisen, R.F. Herrick, and M.A. Mittleman (2002). Acute traumatic occupational hand injuries: type, location, and severity. Journal of Occupational and Environmental Medicine. 44(4): p. 345.

Stegmann, M. B., & Gomez, D. D. (2002). A brief introduction to statistical shape analysis. Informatics and Mathematical Modelling, (March), 1–15.

Sturman, D. J., & Zeltzer, D. (1994). A survey of glove based input. Computer Graphics and Applications, IEEE, 14(1), 30-39.

Swanson AB, Matev IB, de Groot G (1970). The Strength of the Hand. Bulletin of Prosthetics Research pp. 145-153.

Szychlinska, M., Dullaert, K., Beumer, A., Nsir, H., Guglielmino, C., Mazzone, V., & Giunta, S. (2017). Ergonomics of Prehensility in Pushing and Pulling Motions: An Anatomical and Biomechanical Overview. Journal of Functional Morphology and Kinesiology, 2(1), 6. http://doi.org/10.3390/jfmk2010006

Tsai, T.-Y., Li, J.-S., Wang, S., Li, P., Kwon, Y.-M., & Li, G. (2015). Principal Component Analysis in Construction of 3D Human Knee Joint Models Using a Statistical Shape Model Method. Comput Methods Biomech Biomed Engin., 18(7), 721–729.

Turner, D. a, Anderson, I. J., Mason, J. C., & Cox, M. G. (1999). An algorithm for fitting an ellipsoid to data. Methods, 1–12.

Vignais, N., & Marin, F. (2010). A Musculoskeletal Model of the Hand for Biomechanical and Ergonomic Analyses of Manual Tasks. Hand The, (2005),1–5.

Watanabe, T., K. Owashi, Y. Kanauchi, N. Mura, M. Takahara, and T. Ogino (2005) The short-term reliability of grip strength measurement and the effects of posture and grip span. Journal of Hand Surgery. American Volume. 30(3): p. 603-9.

Waters, T.R., Dick, R.B., Davis-Barkley, J., Krieg, E.F., 2007. A cross- sectional study of risk factors for musculoskeletal symptoms in the workplace using data from the General Social Survey (GSS). Journal of Occupational and Environmental Medicine.

Westwood, James. (2002). Medicine Meets Virtual Reality 02/10. IOS Pres. P 64-70

Wiker, S.F., Chaffin, D.B. & Langolf, G.D., 1990. Shoulder postural fatigue and discomfort: A preliminary finding of no relationship with isometric strength capability in a lightweight manual assembly task. International Journal of Industrial Ergonomics, 5 (2), 133-146.

Woltring, H. J., Huiskes, R., de Lange, A., & Veldpaus, F. E. (1985). Finite centroid and helical axis estimation from noisy landmark measurements in the study of human joint kinematics. Journal of Biomechanics, 18(5), 379–389.

Wu, G., Van Der Helm, F. C. T., Veeger, H. E. J., Makhsous, M., Van Roy, P., Anglin, C., … Buchholz, B. (2005). ISB recommendation on definitions of joint coordinate systems of various joints for the reporting of human joint motion - Part II: Shoulder,

elbow, wrist and hand. Journal of Biomechanics, 38(5), 981–992.

Wu, J., Dong, R., & Warren, C. (2012). A Hybrid Model Simulating Hand Gripping on a Cylindrical Handle. W.asbweb.org, 1–2.

Young, J. G., Woolley, C., Armstrong, T. J., & Ashton-Miller, J. a. (2010). Hand-Handhold Coupling: Effect of Handle Shape, Orientation, and Friction on Breakaway Strength. Human Factors: The Journal of the Human Factors and Ergonomics Society, 51(5), 705–717.

Zatsiorsky, V.M., Gao, F. & Latash, M.L., 2003. Finger force vectors in multi-finger prehension. Journal of Biomechanics, 36 (11), 1745-1749.

Zhang, C., & Chen, T. (2001). Efficient feature extraction for 2D/3D objects in mesh representation. Proceedings 2001 International Conference on Image Processing (Cat. No.01CH37205), 3, 935–938.

Zhou, W. (2013). Development of Biomechanical Models for Describing Hand and Finger Placements in Handling Work Objects.

Zhou, W., Armstrong, T., Wegner, D.M. & Reed, M.P., 2011a. Influence of object weight and terminal orientation on upper limb postures during grasping, holding, and placing cylindrical object. Proceedings of Human Factors and Ergonomics Society Annual Meeting

Zhu, Z., & Li, G. (2011). Construction of 3D human distal femoral surface models using a 3D statistical deformable model. Journal of Biomechanics, 44(13), 2362–2368.